AN ALTIMETER WAVEFORM MODEL FOR COMBINED SURFACE AND VOLUME SCATTERING

by

Michael Hayes Newkirk

Thesis submitted to the Faculty of the
Virginia Polytechnic Institute and State University
in partial fulfillment of the requirements for the degree of

DOCTOR OF PHILOSOPHY

in

Electrical Engineering

APPROVED:

Gary S. Brown, Chairman

David A. deWolf

Timothy Pratt

Werner E. Kohler

Warren L. Stutzman

November, 1994
Blacksburg, Virginia

AN ALTIMETER WAVEFORM MODEL FOR COMBINED SURFACE AND VOLUME SCATTERING

by

Michael Hayes Newkirk

Committee Chairman: Dr. Gary S. Brown
Electrical Engineering

(ABSTRACT)

Radar altimeters were originally designed to study ocean geodynamics, where the scattering processes are governed entirely by the surface features. These same altimeters have recorded data from over the polar ice sheets, where the scattering processes cannot in general be limited to surface properties. Radar pulse penetration, which gives rise to volume scattering, must also be accounted for in these return waveforms. This pulse penetration affects the altimeter range measurements as well as other information that is derived from the altimeter waveform data.

To aid in the study of pulse penetration effects, a waveform model for combining surface and volume scattering effects in the estimation of the radar altimeter returns recorded over continental ice and snow is developed and discussed. The surface scattered waveform model is based on the well-known impulse response method which is capable of accounting for arbitrary altitude, beamwidth, pulsewidth and pointing angle. The newly formulated volume scattered waveform model is also an impulse response based method which differs from previous versions in that it can also be applied to a general altimeter configuration. The two models are time registered and then added together in an arbitrary ratio representing the relative contributions of surface and volume scattering to the overall return power waveform. The combined model can be used to study actual altimeter waveforms by varying the important parameters, including surface roughness and effective extinction coefficient. The capabilities and limitations of this new combined model are also discussed and guidelines for its use are detailed.

The combined model is tested by comparing it to the Multimode Aircraft Radar Altimeter (MARA) data which were recorded over and around the Greenland ice sheet in

September 1991. Evaluation of this averaged waveform data identified problems that were encountered with the MARA design. A number of techniques are developed in an effort to account for and correct these problems, but none of these attempts were completely successful. The 1991 MARA data are considered usable for waveform analysis, but with the understanding that some error may be present in the final results.

The MARA data obtained from the Greenland ice sheet are analyzed for estimates of surface roughness, effective extinction coefficient and ratio of surface to volume scattering strengths. A simple optimization method is employed which achieves a least-squares fit of the combined model to the altimeter data. The result is an estimate of these parameters as a function of location on the ice shelf. To the author's knowledge, this is the first time both surface- and volume-related parameters have been estimated simultaneously from Ka-band radar data.

Acknowledgments

A number of individuals are to be thanked for their contributions, both direct and indirect, to this work. First I want to thank those who went before me, especially Bill Smith, Karl Reichard and Paul Werntz, for their continuing encouragement and advice from the very beginning of my graduate career. Their experience has helped me immensely.

I also thank my comrades in the ElectroMagnetic Interactions Laboratory (EMIL) for the endless help and discussions on "why things are" the way they are. Specifically, they are Rob Adams, Dave Kapp, Sean Kelley, Roger Marchand, Keith Tyerar and A. J. Zwiesler. Thankfully, the topics were not always directly related to our research, which I believe helped all of us get by.

Special thanks go to Rob Adams of EMIL for his help with the programming and analysis for the parameter estimation portion of this research. His efforts in this area were crucial to the success of this work. I wish him the best for his graduate program.

To Doug Vandemark of NASA Goddard Space Flight Center - Wallops Flight Facility I owe an enormous amount of gratitude. His help in understanding and navigating the Greenland data set was very important. Certainly without his help the application of this work to `real data' could not have been accomplished.

Thanks also go to Ellen Ferraro (formerly of the University of Massachusetts at Amherst) for her helpful discussions about the AAFE system and the samples of the actual altimeter data. Also, the copy of her dissertation that she provided was especially helpful in understanding how AAFE works.

I want to also point out the departmental support over the many years. Thanks to Loretta Estes for the guidance through the maze that is more commonly known as the graduate program. To the ladies in EE accounting I leave many thanks for their assistance in dealing with purchasing equipment, software and supplies for the lab.

A special thank you to Professor Hugh VanLandingham; he was the Interim Department Head who offered me the Bradley Fellowship. Without that financial

support, there is little doubt in my mind that this work would not have been done. Also, thanks to former Department Head and now Dean of Engineering Bill Stephenson for his continuing support over the years.

I cannot continue without acknowledging the person who was originally responsible for the financial support of the Fellowship. To the late Marion Bradley Via, my deepest thanks for all your help to me and the many others that you have touched. She surely is an angel now. I consider myself fortunate to have met her before she passed away.

Over the years that spanned my graduate career, this work was also supported in part by NASA under grant NAG5-659 and by the Office of Naval Research Electromagnetics and Sea Ice initiative under grant N00014-93-1-0123. The support provided by these agencies is greatly appreciated.

My committee members listed on the first page deserve special thanks. Their guidance and participation in this work has been invaluable. To think that their help is essentially volunteered is a credit to the teaching profession.

To my advisor, Gary Brown, I can only say *thank you*, even though that doesn't say enough. He has supported me through the best and worst times and offered me encouragement, guidance, wisdom and criticism. He is the reason that this work was not only possible, but also understandable. I'll never be able to repay him for all he has done; I only hope that someday I can be as good an advisor to future engineers as he has been to me.

My parents, Kenneth and Janice, are due tremendous thanks. Parents are, after all, the greatest influence on any child, and they had a big part in this work. Thank you, Mom and Dad, for believing in me all along and for allowing the freedom to pursue my goals in my own way. I hope I have the same positive influence on my children.

Finally and most importantly, to my wife Deanna, my sincerest gratitude and deepest love. I know that without her support, encouragement and friendship I would not have been able to do this. When we started out, she had no idea what she was in for, but I think now (and probably all along) she knew it would be worth it in the long run. In many indirect ways this work, and the resulting Ph.D. degree, is hers too.

• • •

This work is dedicated to my daughter, Rebecca Dare, with the hope that in some small way it can be used to provide a better world in which she can grow up and enjoy having children of her own.

• • •

Table of Contents

List of Figures

List of Tables

Chapter 1
Introduction

Spaceborne radar altimeters have been used for many years to map a variety of the earth's features. A radar altimeter, as used in remote sensing applications, is capable of measuring the range to the surface, the peak power and the backscattered power waveform as a function of delay time. The first altimeter experiment that was performed from space was Skylab [23] in 1973, a 13.9 GHz system that served as proof that satellite-based altimeters could provide important oceanographic and geodetic information. In the late 1970's the 13.9 GHz Geos-3 altimeter [33] provided the global coverage needed for large-scale oceanographic and geodetic studies. The 13.5 GHz Seasat altimeter [2,36] operated for only a few months before it failed in 1978, but it demonstrated the most accurate satellite measurements to that time and served as a precursor for the 13.5 GHz Geosat altimeter [19]. Although originally designed to aid in the study of ocean geodynamics, these altimeters have been shown to be useful for studying a number of other global features, including the elevations of the continents and ice masses in the arctic regions. Since their orbits covered up to $\pm$ 72° in latitude, they were able to observe a significant portion the Greenland and Antarctic ice sheets.

The surface elevation measurements of the ice sheets are important because they aid in the understanding of how mankind's actions affect the global environment. A change in the earth's ice masses has obvious effects on the sea level. Recently [31] it was shown that what were thought to be good measurements of the ice sheet topography were significantly affected by the penetration of radar pulses into the snow medium below. This phenomenon causes the elevation measurements to be slightly erroneous and this may lead to false conclusions about the rate of growth or decay of these ice masses and their overall influence on the global temperature balance. Since the altimeters also measured elevation as they passed over the continents, those measurements may be similarly affected by snow cover, vegetative cover or forest canopy. Errors in these measurements may lead to false conclusions about erosion or may infer incorrect assessment of the amount and type of these media.

Elevation measurements are but one of the pieces of information available directly from altimeters. If the pulse penetration can be reasonably quantified, it may be possible to derive certain characteristics about the media being penetrated. In the case of ice sheets, these characteristics might include the density, age, or possible layering in the medium. In the forest case, penetration behavior may be an indication of canopy type or foliage density. The common feature among these measurement examples is *pulse penetration into a medium.* Recent work [31,13,22] has demonstrated the importance of this phenomenon, indicating that a more thorough understanding of penetration is needed, particularly in the polar regions [35]. To accomplish this, a general-purpose waveform scattering model that could be used to analyze a wide variety of satellite and aircraft-based altimeter configurations would be a most useful tool. Previous researchers [31,13,22] have developed waveform models that account for volume scattering, but they were limited to certain ranges in pointing angle or altimeter height because certain simplifying assumptions were used in their derivations. While these simplifications enable somewhat easier and faster waveform modeling and data analysis, they preclude these models from being applicable to a general altimeter system.

The research reported herein attempts to formulate a model that can be used to predict and analyze altimeter data from *any* altimeter system. In this development, the concentration is on the ice and snow medium that is typical to the polar regions and in particular that found on Greenland. With somewhat minor modifications, it may be extended to modeling those waveforms expected from other areas such as vegetative terrain or forest canopies.

There are several scattering sources present over Greenland that can be placed into the categories of surface and volume scatterers; some of these are more dominant than others depending on the region, physical conditions, time of year and/or day and radar parameters. Benson [4] provided a summary of several years' effort in studying the topography of Greenland, by classifying the ice sheet into four facies or regions that have certain distinguishing properties. These regions, shown in Figure 1.1, are known as the *ablation, soaked, percolation* and *dry snow* regions, and are delineated by the *firn, saturation* and *dry snow lines*, respectively.

In the lowest elevations, in regions where the air temperature is often above freezing (0°C) during the summer, the surface of the ice sheet is wet and electromagnetic

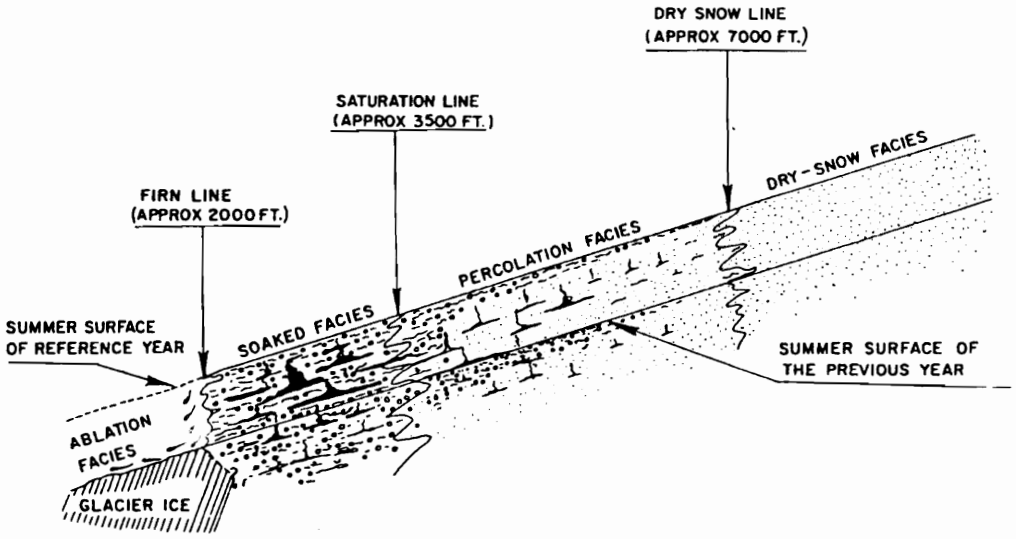

Figure 1.1. Diagram of the four general regions of the Greenland ice sheet. From [4].

penetration into the medium is extremely limited. This situation is common to the ablation and soaked regions of Greenland. The ablation region is separated from the soaked region by the firn line and is identified as the area where the snow cover is stripped away to reveal the bare glacier ice. The soaked region is the area from the firn line to the saturation line, where complete soaking of the ice sheet is noticed. The saturation line separates the soaked and percolation regions. Since the surface is typically wet in these lower two regions the scattering is dominated by the surface features, usually the surface roughness; however, *melt ponds* can exist in these regions. They act like wind-roughened specular scatterers, which contribute their strongest scattered power to a nadir oriented altimeter. In these two regions very little electromagnetic penetration is seen, so surface scattering dominates the total scattering process.

In the region above the dry snow line, where the air temperature never rises above freezing even in the summer, the scattering is dominated by the *ice particles* that make up the ice sheet. This dry snow region covers the upper altitudes of Greenland (from about 2 km at 81°N to about 3 km at 69°N), where there is no moisture either in the medium or on the surface, so the dominant scattering is due to the particles. Many authors consider an ice sphere to be an acceptable approximation to the particle shape [37,20], in part because the scattering problem is significantly easier for a sphere than for other more complicated geometries [17,5]. When the snow is packed or very dense such that the volume fraction of ice particles is greater than 50%, the medium may just as easily be modeled as voids or *air particles* distributed throughout an ice background. In either case, a random distribution of small particles in a background medium provides a good description of most areas of the ice sheet. Another possible scattering source in this and all regions is the ground beneath the ice sheet. This may be of little concern for millimeter-wave frequencies over the polar ice sheets, since the electromagnetic depth of penetration is not enough to reach the ground. Low frequency radars have been used to observe the underlying bedrock [38], so attention must be given to the frequency of the probing instrument. Thus, volume scattering dominates in this region, except for very high frequency (above Ka-band) altimeters, which have smaller penetration depths. In the optical limit there is essentially no penetration, so in this case the scattering would be due to the surface.

In the area between the saturation line and the dry snow line, the percolation region contains a mixture of the surface sources mentioned above along with a particular class of

volume features. In this region, localized melting creates melt ponds, as well as *ice glands*, *lenses* and *layers,* which Benson defines as [4]:

> "a) Ice layers extend over large areas parallel to the strata with only minor interruptions.
> b) Ice lenses are lens-shaped layers which pinch out laterally. They are parallel to the firn strata.
> c) Ice glands are pipe-like vertically extending masses which occasionally spread laterally to form lenses and layers. They are the frozen percolation channels which feed lenses and layers."

These structures are present beneath the surface of the ice sheet and are formed when rising air temperatures result in surface melting and seepage of water into percolation channels. These channels transport the water down to some colder depth where the water distributes laterally and refreezes to form the randomly distributed glands, lenses and layers. Some researchers, e.g., Swift, *et al.* [34], have modeled these features (to first order) by spheres and cylinders in the scattering problem. They are obviously larger and more complex than the ice or air particles discussed above, so this approach may be somewhat over-simplified. There can also be *moisture* within the medium which acts like discrete volume scatterers in the same manner as ice particles. Depending on the temperature within the ice sheet this moisture can take the form of inclusions between the particles, ice glands and lenses. In this region, there can be contributions from each of the above sources, including moistened surface roughness. Thus, both surface and volume scattering contribute to the overall scattered waveform, with the relative strengths of each varying spatially and/or temporally.

Benson [4] notes that the extent and presence of these four regions have a temporal dependence which is both long and short term. At a given location during the winter, for example, the environment and near-surface features of the entire Greenland ice sheet varies little from edge to center, while during the summer months the different regions discussed above are present. Also, the temperatures in some of these regions can vary from above to below freezing on a daily basis, so the surface may appear wet during the day while it may be refrozen during the night. Thus, the time of year and even time of day will affect the amount of scattering from any of these sources. Benson provides the locations of these regions [4] which are approximated in Figure 1.2.

In order to study the effects of the scattering in each of these different regions, a waveform model must be developed that can account for the variable features discussed

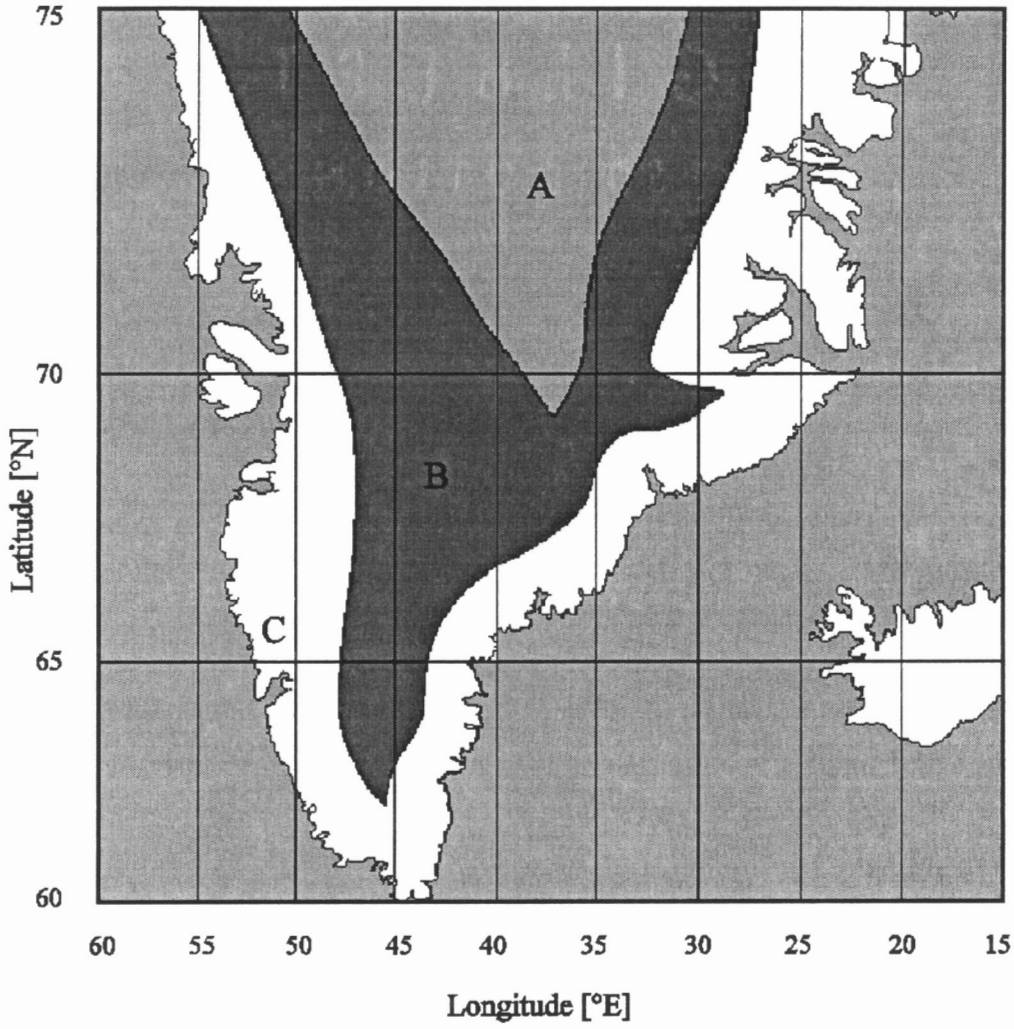

Figure 1.2. A rough estimate of the four regions of Southern Greenland, as given by Benson [4]: (A) dry snow, (B) percolation and (C) soaked and ablation regions.

above. To accomplish such a development, the following course of action has been followed. First, previous research in waveform scattering is investigated, pointing out the reasons that they cannot be used for this problem. Other scattering theories, including radiative transfer and other field-based methods are not included in this discussion because they are typically used to model the scattering intensities or cross-sections for surfaces and random media for a particular frequency [17]. For the problem at hand, the σ^o behavior is assumed in order to obtain the desired scattered waveform shape. As such, these other methods are not applicable. Following the background study is an introduction of the approach used to provide the model necessary to quantify the penetration effects. The derived model must be tested, so an outline of this procedure is given. Finally, a method for using this model to extract a measurement of these effects is then briefly discussed, with the following chapters used to provide the details of this research.

1.1 Survey of Past Work in Scattered Waveform Modeling

The discipline of radar altimetry has been an active research area for more than three decades. In 1957, Moore and Williams [25] put forth the concept that a pulse backscattered from a rough surface could be represented by a convolutional expression, which was supported by their observations of radar data scattered from terrain. Many other researchers have furthered this model, providing simplifications and/or generalizations of this concept. In 1977, Brown [8] provided a set of expressions that simplified the Moore and Williams model for application to spaceborne systems. Further simplifications were developed for off-nadir pointing angles [9]. A number of researchers [16,32,34,31,13] relied on these expressions (which they all refer to as the Brown model) for their studies of scattering from oceans, as well as ice and snow. Newkirk and Brown [26] provided further generalizations of this work to accommodate special antenna configurations as well as arbitrary altitude, making this the most versatile model available for waveform scattering from rough surfaces.

In all of this previous work, the particular versions of the convolutional model assumed that the return waveforms were scattered from an impenetrable rough surface. Since these applications were developed primarily for ocean surface scattering, this assumption was valid. As discussed previously, certain other surfaces cannot be

described as impenetrable. Examples of such penetrable media include the ice shelves that are present in the arctic regions and vegetation over land. For these media types, modifications to the waveform scattering model are clearly necessary.

A number of individuals have been active in volume scattering waveform modeling, including Ridley and Partington [31], LeVine, *et al.* [22], and Davis and Moore [13]. Each of these researchers provided a specialized model for waveform scattering from penetrable media, but with certain restrictions on their use. For example, the models developed by Ridley and Partington [31] and Davis and Moore [13] are only capable of modeling high altitude, normal incidence scattered waveforms. The application of these models was to satellite-recorded data, so such restrictions were acceptable. In addition, the Ridley and Partington model could not account for the more realistic non-rectangular transmitted pulse shapes. The vegetation model provided by LeVine, *et al.* [22] uses the distorted Born approximation to derive an impulse response for both "thick" and "thin" layers over a ground plane, but it is restricted to far off-normal incidence. The limitations placed on these models are acceptable for their intended applications, but too restrictive for analyzing general near normal-incidence radar returns from penetrable media.

Davis and Zwally [14] demonstrated the importance of accounting for the volume penetration of radar altimeter pulses into the polar ice sheets. Through the application of a combined surface and volume scattering model [13], they were able to identify areas of Greenland that exhibit significant volume penetration of 5-7 meters at a microwave frequency of 13.5 GHz. They also reported that the penetration depth was highly correlated with latitude, elevation and (for Greenland) the number of days per year that an area experiences melting temperatures. Recently, Ferraro [15] used the 13.9 GHz AAFE altimeter waveforms to identify ice layers in the percolation zone that were roughly one meter below the surface and extended over large lateral distances. Thus, altimeter measurements of the polar ice sheets are affected non-uniformly over the full extent of the ice sheet.

Up until now, the models used by these authors provided the necessary means for analysis of their particular needs; however, for the cases of radar altimetry where the pointing angle and/or radar altitude do not fit their criteria, a more general waveform scattering model is necessary.

1.2 Outline of Research

One of the major goals of this research is to provide a *general* scattered waveform model for penetrable media such as ice and snow. This means providing a model that can be applied to both nadir (normal incidence) and off-nadir antenna orientations, unrestricted platform altitude, general antenna power pattern beamwidth, and arbitrary transmitted pulse shape. The model must also account for the contributions of the surface and volume components of the total scattering process. In addition, the desired model is to be capable of accounting for an antenna pattern that is not necessarily azimuthally symmetric, i.e. one having different E- and H-plane beamwidths.

A suitably general waveform model for the surface scattering portion of the total scattered waveform was mentioned in the previous section. This model [26] is comprised of a convolution of three functions - the flat surface impulse response, the radar system point target response and a probability density function for the height of the rough surface. The impulse response is general enough to account for the various system parameters such as pointing angle, radar altitude and antenna beamwidth. Certain simplifications that depend on pointing angle are shown for the impulse response which serve to speed up calculations [26]. The point target response represents the transmitted pulsewidth and receiver effects while the height pdf accounts for the degree of surface roughness.

The first step in deriving a combined surface and volume scattering waveform model is then to formulate an appropriate waveform model for volume scattering. This is also an impulse response based method, similar in form to the surface scattering model. As was done for the surface model, simplifications can be made to the volume model's impulse response which allow more rapid calculations for specific pointing angle ranges. The two scattering models are then combined to provide a waveform model that accounts for the surface and volume scattering, with the relative strengths of each determined by a single parameter.

As a means for testing the combined waveform model derived in this work, it is compared to actual altimeter data from over water. The comparison to water data is logical as scattering from bodies of water such as oceans are better understood than scattering from ice sheets. As a consequence of this comparison, a number of problems specific to the chosen altimeter system are identified and the methods used to deal with

these problems are discussed. The altimeter data was obtained by the Multimode Aircraft Radar Altimeter (MARA), which was designed and flown by NASA / Goddard Space Flight Center - Wallops Flight Facility [28]. The MARA system is unique in that it is capable of simultaneously recording high-resolution data from five antenna beams, nominally pointed toward nadir and off-nadir in four azimuthal directions: forward, right, left and aft. The other distinguishing feature of the Ka-band MARA system is that with its extremely narrow antenna beamwidth of 0.6° and short pulsewidth of 6.5 ns, it produces beamwidth-limited data. This instrument was used during a 1991 joint experiment to observe the Greenland ice sheet as well as some of the surrounding waters. It is these data that are used to test the MARA system, as well as analyze the ice sheet for its medium parameters.

An appendix provides the necessary formulas to determine whether an altimeter operates in a beamwidth- or pulsewidth-limited state. Conventional satellite-based altimeters such as the Ku-band Seasat and Geosat are pulsewidth-limited systems by virtue of their altitudes, even though they have relatively narrow beamwidths of 1.6° and 2.0°, respectively, and short pulsewidths of 3.2 ns each. The MARA system that is used to qualify the model derived in this work is a vastly different altimeter than the satellite-based systems. This is primarily due to the relatively low altitude (< 1 km), but also because of its extremely narrow beamwidth (0.6°). MARA's unique operating characteristics will be shown to be particularly useful in determining the penetrable medium effects on altimeter data.

This leads into the other major goal of this work - to provide a method by which a set of parameters that describes a penetrable medium can be obtained. These parameters include the roughness of the interface between the medium and free space, a parameter that describes the content of the medium and another that indicates the relative contributions of the scattering from an interface and its underlying medium to the overall scattered waveform. A test case for this method, in which a waveform model is fit to itself, is used to verify its capabilities. Examples of how this parameter estimation technique is used to extract information from altimeter data will be given. The data that will be used is taken from an archive of the 1991 MARA Greenland mission.

Finally, a summary of the work is presented. The achievements of this research will be presented along with suggestions for future research ideas. This work only begins to

examine the problem of media penetration, but it serves as a stepping stone to the end goal of understanding the total waveform scattering phenomenon.

Chapter 2
Scattered Waveform Model Development

To parameterize the effects of the volume penetration of altimeter pulses, a suitable scattering model must be developed. This model should be able to account for a number of effects including the incidence angle of the radar pulses, the antenna power pattern beamwidth and gain characteristics, the radar system's altitude above the medium and the composition of the medium itself. Simplifications are sought to minimize the amount of computer resources (CPU time) needed to calculate these waveforms. These simplifications are necessary to make the study of extended areas feasible.

The approach taken in the derivation of this model consists of two steps. The overall scattering model is the summation of the individual surface scattering and volume scattering models. The first step is to either derive new versions or employ existing versions of individual surface scattering and volume scattering models. For this step, a suitable surface scattering waveform model already exists; however, the necessary volume scattering waveform model does not. The second step is to then combine these two models in some fashion to obtain the combined surface and volume scattering waveform model. The purpose of this chapter is then to derive a suitable volume scattering waveform model that can be combined with the appropriate surface model and then provide a means by which the two can be combined. Section 2.1 briefly outlines the surface scattering model that will be used; section 2.2 details the volume scattering model. Finally, the combination of the two models is discussed in section 2.3 and examples of such model waveforms are shown, along with an example of a fit of the combined model to real altimeter data. Finally, section 2.4 provides an overview of the capabilities and limitations of this model.

2.1 The Surface Scattered Waveform Model

The first step in the process of constructing the combined model is to find an appropriate waveform model for surface scattering. The impulse response based surface

scattering model introduced by Moore and Williams [25], improved by Brown [8] and used by many [31,13,16] is employed, but with the specific features that were developed for this method by Newkirk and Brown [26]. These features include general pointing angle, antenna beamwidth and radar altitude, as well as simplifications for nadir and off-nadir pointing angles. This model is expressed as a convolution of quantities known as the *flat surface impulse response*, *radar system point target response* and *surface height probability density* functions.

The flat surface impulse response (FSIR) results in [26] contain a simplification that results from assuming the model would be used only for high altitude altimetry. This restricted $c_o\tau/h \ll 1$, so that $(1 + c_o\tau/h) \approx 1$, a condition that is easily violated for low altitude altimetry common to the aircraft experiments. In the above expressions, c_o is the speed of light in free space, τ is the two-way ranging time referenced to $2h/c^*$ and h is the radar altitude. To remedy this situation, the equations for the FSIR in [26], namely (9), (12) and (15) must be modified to allow for low altitude operation. In each expression, the only changes necessary are to replace the amplitude factor $1/2h^3$ with the factor $4/(c_o\tau + 2h)^3$. These equations are presented here without derivation, since the details are published [26]. The only difference between what is given in [26] and here is that the low altitude condition described above is also included. For *arbitrary* off-nadir pointing angle ξ, the FSIR as a function of delay time is

$$P_{FS}(\tau) = \frac{4G_o^2\lambda^2 c_o\,\sigma^o(\theta)}{(4\pi)^3(c_o\tau + 2h)^3}\int_0^{2\pi} \exp\left\{ -\frac{4}{\gamma}\left[1 + \frac{\beta\rho^2\sin^2\phi}{\rho^2 - 2\rho\rho_o\cos\phi + \rho_o^2}\right]\right.$$
$$\left. \cdot \left[1 - \frac{\left(\cos\xi + \epsilon\sin\xi\,\cos\phi\right)^2}{1+\epsilon^2}\right]\right\} d\phi, \qquad \tau \geq 0, \tag{2-1}$$

where

G_o	boresight antenna gain
λ	radar carrier wavelength
c_o	free-space speed of light
$\sigma^o(\theta)$	radar cross-section per unit area of the illuminated surface (angle dependent)

* $\tau = 0$ corresponds to the time delay between when the leading edge of the transmitted pulse has traveled to the surface, been scattered by the surface, traveled back to the radar and is just entering the radar receiver.

h radar system altitude

$\epsilon = \sqrt{c\tau/h}, \quad \rho = \sqrt{c\tau h}, \quad \rho_o = h\tan\xi.$

(The geometry associated with this model is the same as used for the volume model in §2.2; see Figure 2.6) The parameters γ and β are related to the antenna beamwidth [26] through

$$\gamma = \frac{2\sin^2(\theta_s/2)}{\ln 2}, \tag{2-2}$$

$$\beta = \frac{\gamma \ln 2}{2\sin^2(\theta_{xs}/2)} - 1. \tag{2-3}$$

The parameters θ_s and θ_{xs} are the *scan* and *cross-scan* beamwidths, which can be thought of as the E- and H-plane beamwidths of the antenna. If the two beamwidths are identical, β reduces to zero.

It should be pointed out that the expression for the radar cross-section per unit scattering area, σ^o depends in general on angle θ *and* time τ, as shown in Figure 2.1. Notice that as time progresses, the projection of the impulse $\delta(\tau + 2(r-h)/c)$ on the surface moves through the beamwidth away from the origin. The only contribution from the surface in the impulse response comes from within the antenna pattern 3 dB width, shown as the angular extent given by BW in the figure. For this work, it is assumed that the antenna beamwidth is sufficiently small to allow this time dependence to be ignored. This means that the angular resolution determined by the antenna beamwidth is small enough that σ^o does not vary appreciably over the extent of the illuminated area. For wider antenna beamwidths, it may be necessary to reconsider this assumption.

When the altimeter is pointed at nadir the integrand becomes symmetric about the origin and independent of ϕ so a simplification of (2-1) results;

$$P_{FS}(\tau) = \frac{2G_o^2\lambda^2 c\,\sigma^o(\theta)}{(4\pi)^2(c_o\tau + 2h)^3}\exp\left\{-\frac{4\epsilon^2}{\gamma}\left[1+\frac{\beta}{2}\right]\right\} I_0\left[\frac{2\beta\epsilon^2}{\gamma}\right], \tag{2-4}$$

with $\tau \geq 0$. When the altimeter is pointed *far enough* away from nadir, an asymptotic approximation for the FSIR is derived using Laplace's method [3]. Its form is [26]

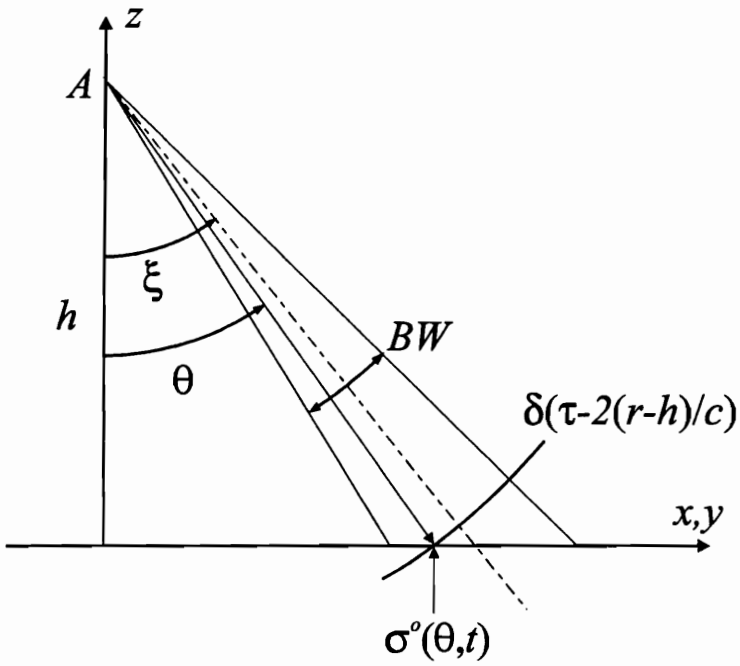

Figure 2.1. Demonstration of the angle and time dependence of σ^o in the flat surface impulse response.

$$P_{FS}(\tau) = \frac{2G_o^2\lambda^2 c\,\sigma^o(\theta)}{(4\pi)^2(c_o\tau + 2h)^3}\exp\left\{ -\frac{4}{\gamma}\frac{(\sin\xi - \epsilon\cos\xi)^2}{1+\epsilon^2}\right\}\sqrt{\frac{2\pi}{\alpha_s}}, \tag{2-5}$$

where

$$\alpha_s = \frac{4\epsilon}{\gamma(1+\epsilon^2)}\left[\sin 2\xi + 2\epsilon\left(\sin^2\xi + \beta\cos^2\xi\right)\right]$$

and $\tau \geq 0$. The condition for using the asymptotic form in (2-5) in place of the general form in (2-1) is [26]

$$\tau \geq \frac{h}{c}\left[\frac{0.849\gamma(1+\tan^2\xi)}{\tan\xi}\right]^2. \tag{2-6}$$

This condition is used to find the minimum time for which the asymptotic form for the FSIR can be used for a given pointing angle and antenna beamwidth. For the case of asymmetric beamwidths ($\beta \neq 0$), the most conservative value for (2-6) is found by using the value of γ that corresponds to the largest of the principle plane antenna beamwidths [26].

To obtain the average return power waveform for surface scattering, the appropriate expression for the FSIR is convolved with the height probability density function of the rough surface and the system point target response (PTR) [26];

$$S(\tau) = P_{FS}(\tau) \otimes P_H(\tau) \otimes P_{PT}(\tau), \tag{2-7}$$

where $\otimes$ is the convolution operator. Any form can be used for $P_H(\tau)$ so long as it satisfies the requirements of a pdf. In most cases it can be adequately represented by a Gaussian function of the form [8]

$$P_H(\tau) = \frac{1}{\sqrt{2\pi}\sigma_s}\exp\left\{ -\frac{\tau^2}{2\sigma_s^2}\right\}, \tag{2-8}$$

where $\sigma_s = 2\sigma_h/c$ and σ_h is the rms surface roughness or standard deviation from the mean of the surface. The PTR represents the receiver's effects on the transmitted pulse shape. It can be a measured function, but for convenience it is often approximated by another Gaussian function.

Appendix A discusses the difference between pulsewidth-limited and beamwidth-limited altimeter configurations. This difference is important because the altimeter's return waveform shapes for each type are markedly different, as will be seen in the examples below. A beamwidth-limited system has its return waveform governed by its antenna beam's illuminated area or footprint on the surface, while a pulsewidth-limited system's return waveform is determined by the projection of the pulsewidth on the surface.

Examples of surface scattered waveforms are shown in Figures 2.2 and 2.3 for an altitude of 500 meters. Figure 2.2 shows sample waveforms for the Multimode Aircraft Radar Altimeter (MARA) system parameters: 0.6° beamwidth, 6.5 ns pulsewidth and 36 GHz frequency. Using these parameters and an altitude of 500 meters in the expressions given in Appendix A shows that the system is considered beamwidth-limited both at nadir and 12°. The waveforms in Figure 2.3 are examples of those that would be obtained from the MARA system if its parameters were altered to a 6° beamwidth and 2 ns pulsewidth. According to Appendix A, this configuration is pulsewidth-limited for an altitude of 500 meters.

Figure 2.2 shows the beamwidth-limited average waveforms for both nadir and off-nadir (12°) pointing angles and two values of rms surface height, σ_h. Note how the waveforms are very insensitive to pointing angle, retaining the same basic shape as ξ changes. The waveforms widen as σ_h increases, which means that a larger deviation in the surface height causes a broadening of the scattered waveforms. This principle permits measurement of the surface heights of the ocean from altimeter data. Figure 2.3 shows some examples of pulsewidth-limited waveforms for the same pointing angles and σ_h values. Notice that the pointing angle dependence is now rather drastic. Also, the surface roughness sensitivity is "lost" in the 12° waveform. These features will enable a beamwidth-limited system to distinguish surface roughness changes from pointing angle errors more readily than the pulsewidth-limited system.

The example waveforms shown in Figures 2.2 and 2.3 are computed for the low altitude of 500 m. This height was chosen because it is roughly the altitude at which the altimeter data that will be examined later were recorded. To illustrate the affect that altitude has on waveform behavior, Figures 2.4 and 2.5 compare the beamwidth- and pulsewidth-limited waveforms expected from an altitude of 50 km for an rms surface

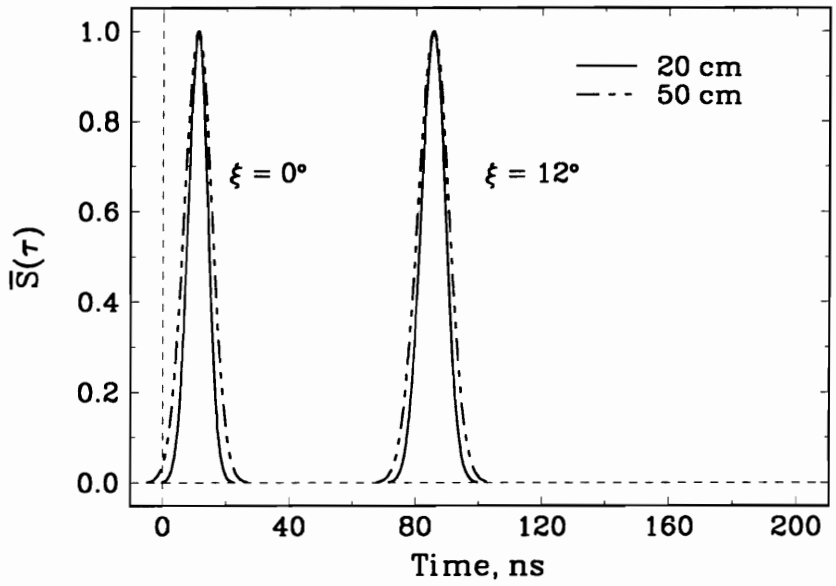

Figure 2.2. Modeled surface scattered waveforms for a beamwidth-limited altimeter. The altitude is 500 m, beamwidth is 0.6° and pulsewidth is 6.5 ns. Shown are two values of rms surface height, 20 cm (solid) and 50 cm (dashed), and antenna pointing angles of 0° and 12°. Note the similar shapes of the waveforms for each pointing angle.

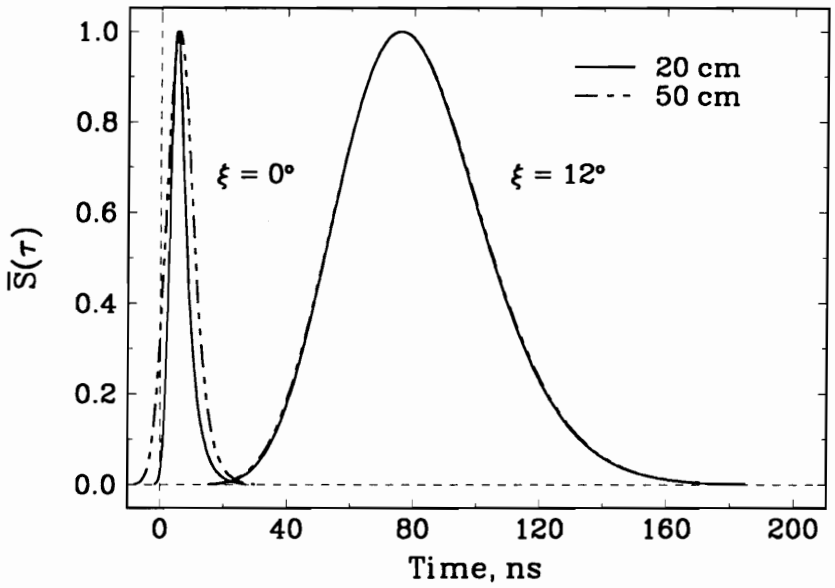

Figure 2.3. Modeled surface scattered waveforms for a pulsewidth-limited altimeter. The altitude is 500 m, beamwidth is 6° and pulsewidth is 2 ns. Shown are two values of rms surface height, 20 cm (solid) and 50 cm (dashed), and antenna pointing angles of 0° and 12°. In this case, the waveforms are markedly different for changing pointing angle.

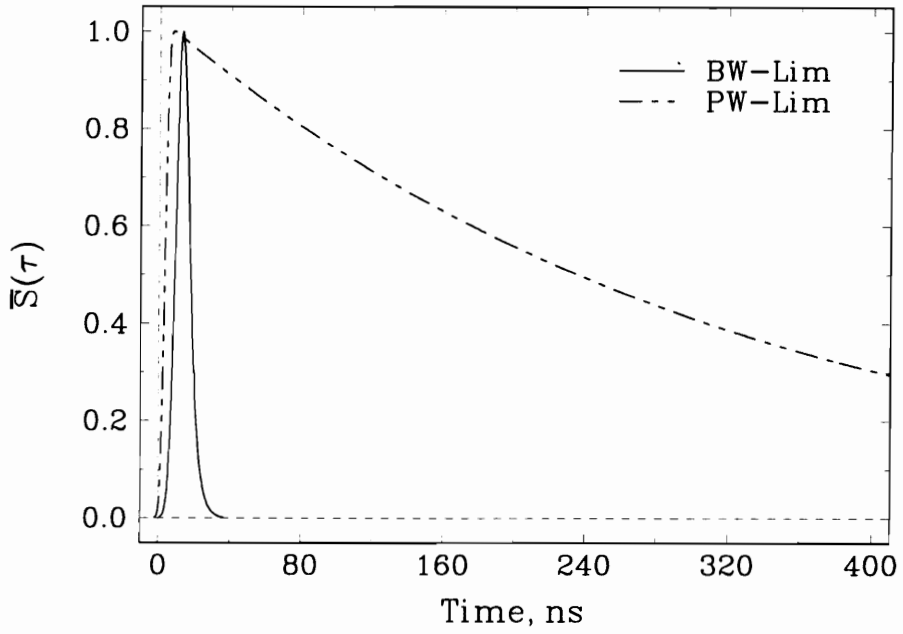

Figure 2.4. Example surface scattered waveforms for nadir oriented beamwidth- and pulsewidth-limited altimeters at 50 km and $\sigma_h = 20$ cm. For the beamwidth-limited case, the beamwidth is 0.6° and pulsewidth is 6.5 ns. For the pulsewidth-limited case, the beamwidth is 6° and pulsewidth is 2 ns.

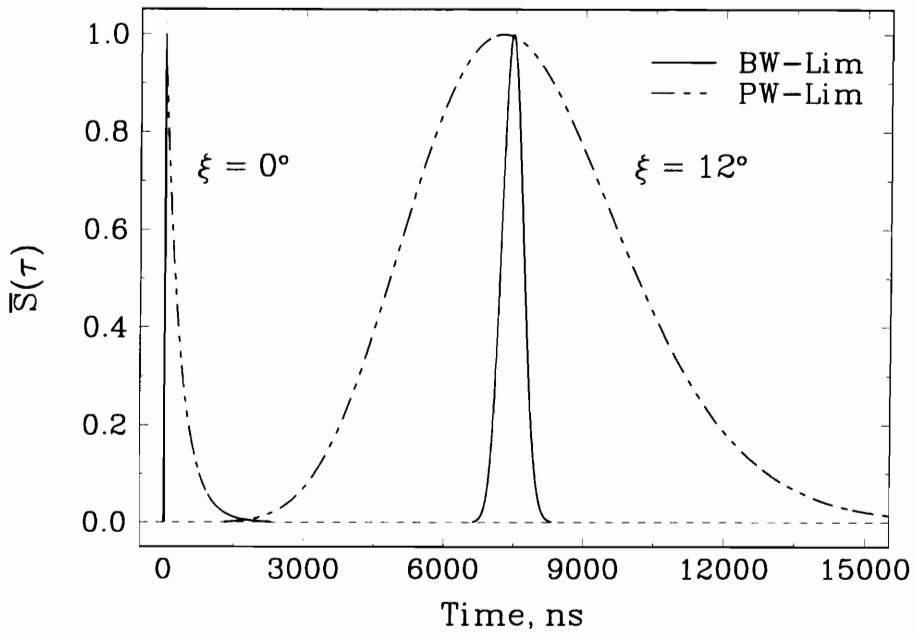

Figure 2.5. Example surface scattered waveforms for 12° off-nadir oriented beamwidth- and pulsewidth-limited altimeters at 50 km and $\sigma_h = 20$ cm. For the beamwidth-limited case, the beamwidth is 0.6° and pulsewidth is 6.5 ns. For the pulsewidth-limited case, the beamwidth is 6° and pulsewidth is 2 ns.

roughness of $\sigma_h = 20$ cm. The beamwidth-limited waveforms are obtained for a beamwidth of 0.6° and pulsewidth of 6.5 ns and the pulsewidth-limited waveforms are for a beamwidth of 6° and pulsewidth of 2 ns. These values correspond to the values used to obtain the waveforms in Figures 2.2 and 2.3. Figure 2.4 shows these waveforms for nadir, while Figure 2.5 shows these for both nadir and 12° off-nadir.

At this high altitude, the difference between the beamwidth- and pulsewidth-limited waveforms becomes even more noticeable than at lower altitudes. Comparing the pulsewidth-limited returns for nadir at these two altitudes (compare Figures 2.3 and 2.4) shows the greatest change. The nadir waveforms are included in Figure 2.5 to demonstrate the tremendous difference between the two altimeter types. Notice the time scale in Figure 2.5; these waveform widths are more representative of those encountered in satellite-based altimeters

2.2 The Volume Scattered Waveform Model

The average return power waveform due to volume scattering from a half space of discrete random media is composed of two parts - the *volume scattered impulse response*, or VSIR, and the radar system *point target response*, or PTR. The convolution of the VSIR and PTR results in the average return power waveform or *volume scattering pulse response*. This is the same basic approach taken by Newkirk and Brown [26] and outlined in §2.1 to obtain the average return power waveform due to surface scattering. This approach is deliberately taken to make the combination of the surface and volume scattering models easier.

There is a fundamental difference in how the surface and volume scattering are modeled. This difference lies in what is actually being measured when a radar is pointed at a discrete random medium. In surface scattering, the quantity usually being measured is the backscattered power as a function of time. Knowledge of the pointing angle permits the determination of $\sigma^o(\xi)$ by inverting the radar equation, provided that the antenna beamwidth is not too large. If the beamwidth is too large, the result is loss of angular resolution for σ^o.

For the volume scattering model, the principle is the same in that the desired quantity from the measurement is the backscattering cross section $N_V \sigma_a$ of the discrete scatterers

contained within the thin volumetric shell as it propagates through the medium. The problem is that as the pulse passes through the medium, a portion of its energy is both scattered in all directions and absorbed by the particles that make up the medium. This combined scattering and absorption is called extinction [17]. The portion that is scattered back toward the radar must undergo this extinction again as it propagates back out of the medium. The net effect is that the return pulse undergoes twice the extinction per unit distance traveled through the medium to the scatterers. Thus, a direct measure of $N_V \sigma_a$ is not possible; instead some attenuated estimate of the parameter is obtained.

To remedy this problem, the volume scattering model incorporates this two-way attenuation through the use of an exponential decay term in the impulse response, as described in the following section. The rate of decay is controlled by an attenuation or *effective extinction coefficient*, k_e, of the medium. Mathematically, it is given by $\exp\{-2k_e\chi\}$, where χ is the one-way distance from the interface through the medium to the shell of discrete scatterers. This concept is similar to that used in previous volume scattering models [31,13]. It is important to point out that k_e may be frequency-dependent [37]. Altimeters operating at different frequencies will experience different extinction rates. Ulaby, *et al.* [37] provides estimates of extinction vs. frequency behavior, so translation of extinction measurements between frequencies may be estimated, but not known for sure.

The impulse response takes into account the operating characteristics of the altimeter, in particular the radar height, antenna beamwidth and pointing angle, as well as the description of the random medium by the effective extinction coefficient, and density of particles that make up the medium. The medium is assumed to be composed of small particles suspended in a background medium of air. The point target response is essentially the radar altimeter's transmitted pulse as modified by the receiver effects. An advantage to this method is that the point target response is a fixed, known waveform - it can be measured; it is also the same waveform used for both the surface and volume scattered waveform models.

2.2.1 The Impulse Response

The VSIR function serves the same purpose as the flat surface impulse response in §2.1. By definition, it is the response of a half-space containing independent, randomly distributed discrete volume scatterers that can be characterized by an effective extinction

coefficient, k_e, to an impulse of energy from a radar having altitude h, 3-dB antenna beamwidth θ_b and pointing angle ξ. It is important to note that any scattering from the interface is completely accounted for by the surface scattering model, discussed in Section 2.1.

Figure 2.6 shows the geometry used to construct the VSIR. The radar antenna is located at point A and altitude h above the surface (xy-plane). The antenna is pointed away from nadir by the angle ξ and its boresight axis is r_o. The differential volume dV is located at angles θ and ϕ, a distance r from the altimeter. Note that dV is *always* located below the surface. The general VSIR equation for this geometry is [26]

$$P_{IR}(t) = \frac{\lambda^2}{(4\pi)^3} \int_V \frac{G^2(\psi,\omega) T_b^2(\theta)}{r^4} \, \delta\left[t - 2\left(\frac{r_i}{c_o} + \frac{(r - r_i)}{c_s}\right)\right] \sigma_V^o \, dV \qquad (2\text{-}9)$$

where

λ	radar carrier wavelength
$T_b(\theta)$	Fresnel power transmission coefficient of background medium
$G(\psi,\omega)$	radar antenna gain pattern
$\delta(\bullet)$	impulse function, appropriately delayed in absolute time
r	range to differential volume
r_o	antenna boresight range to free space / medium interface
r_i	range to free space / medium interface
c	speed of light $= c_o$ in free space, $= c_s$ in snow medium
σ_V^o	scattering factor
dV	$= r^2 \sin\theta \, dr \, d\theta \, d\phi$; differential volume within medium.

The argument of the impulse function allows for the impulse traveling through free space for a portion of the time and within the medium the rest of the time. If the penetrable medium were replaced by free space, c_s would be replaced by c_o and the impulse function would reduce to the more familiar form of $\delta(t - 2r/c)$.

The scattering factor σ_V^o in (2-9) is given by

$$\sigma_V^o = N_V \sigma_a \, u(r - r_i) \, e^{-2k_e(r - r_i)}, \qquad (2\text{-}10)$$

where N_V is the effective number density of scatterers, σ_a is the scattering cross section of an average scatterer and k_e is the *effective extinction coefficient* of the medium with units Np/m. From Figure 2.7, $r_i = h \sec\theta$ is the distance along the r-coordinate from the antenna (A) to the medium interface (C). Thus $u(r - r_i)$ is the unit step function that

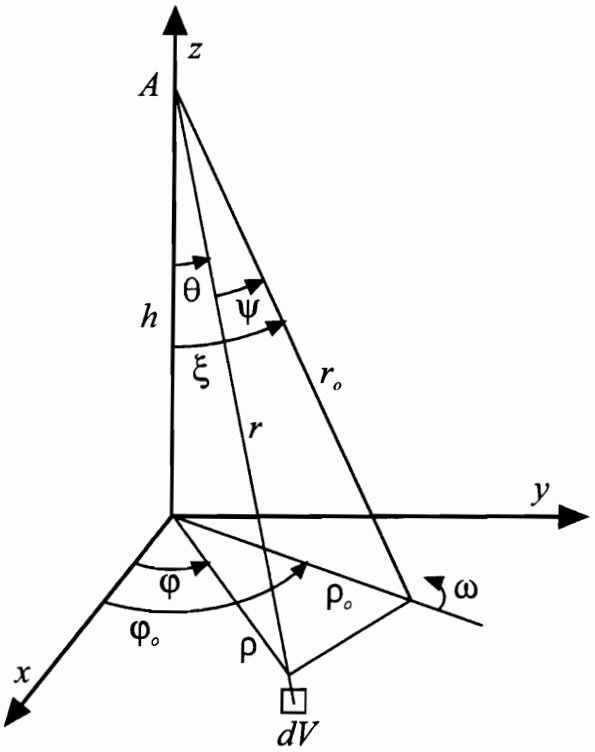

Figure 2.6. Geometry used to derive the volume scattered impulse response. "A" is the altimeter location and r_o is the antenna boresight axis. dV is the differential volume, which is *always* located below the surface (xy-plane).

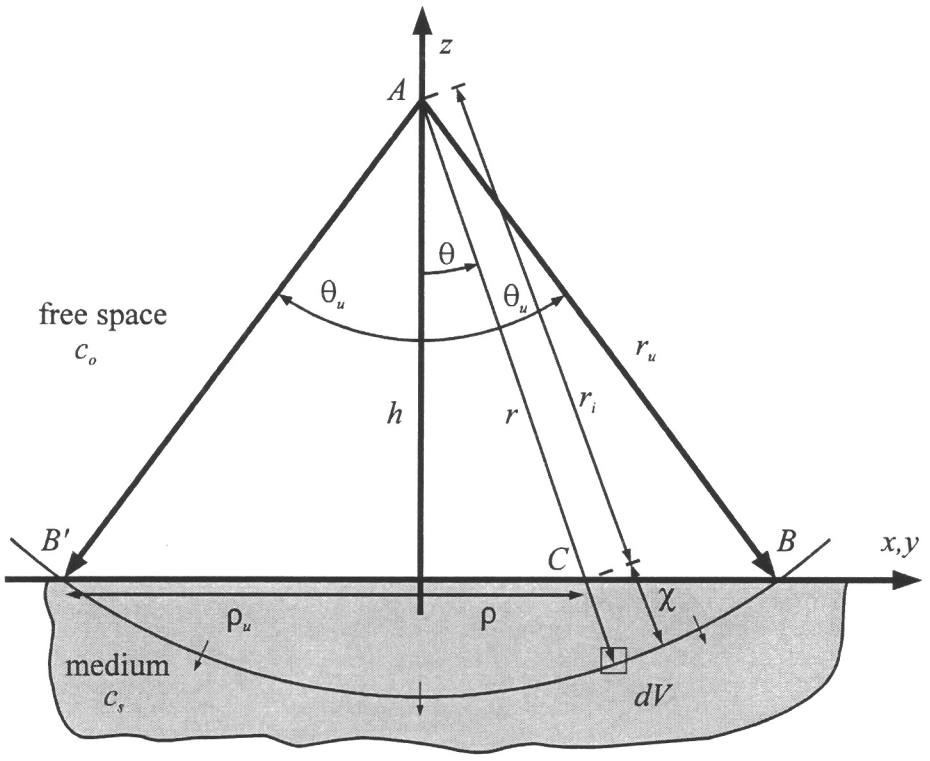

Figure 2.7. Two-dimensional illustration of the limits of the θ-integration for the VSIR. The altimeter is at point A. A spherically expanding impulse of energy is propagating into and through the random medium and intersects the surface (xy-plane) as a circle of radius ρ_u at points B and B'. The distance in the medium from the interface to the impulse is $\chi = r - r_i = r - h\sec\theta$.

"turns on" when $r > h\sec\theta$ and "turns off" when $r < h\sec\theta$; this limits the volume integration in (2-9) to the random medium half-space, as illustrated in Figure 2.7. At an instant in time, the spherically expanding impulse has traveled a distance r_u from the nadir-oriented altimeter located at point A, and intersects the mean surface (the xy-plane) at points B and B'. Thus, the upper limit of the theta integration for this time instant and is given by $\theta_u = \cos^{-1}(h/r)$. This intersection at B and B' is actually a circle of radius $\rho_u = h\tan\theta_u$ in the xy-plane, but in this two-dimensional view it is represented as two points on the mean surface, the "xy-line". When the integration variable r is greater than $h\sec\theta$ and $\theta \leq \theta_u$, as shown in the figure, the unit step is "on" and the integration is performed. If r is less than $h\sec\theta$ or $\theta > \theta_u$, it is not performed. As the impulse progresses in time, the upper limit θ_u changes and the integration space expands. The exponential factor in (2-10) thus accounts for the exponential attenuation of the impulse as it travels a distance $\chi = r - r_i$ from the interface through the medium to the differential volume dV and back, a total "round-trip" distance of $2(r - h\sec\theta)$.

For the main beam of the antenna pattern, the radar antenna gain is adequately represented, by an elliptical Gaussian beam [26] given by

$$G(\psi,\omega) = G_o \exp\left\{ -\frac{2}{\gamma}\left(1 + \beta\sin^2\omega\right)\sin^2\psi \right\}, \qquad (2\text{-}11)$$

where β is a dimensionless parameter that describes the degree of pattern asymmetry. If $\beta = 0$, (2-11) becomes the expression for a symmetric Gaussian beam. Many authors [16,31,26,13] have used the symmetric Gaussian in their versions of the Brown surface model, and it will be used here also. As seen is Figure 2.6, ψ is measured relative to the boresight axis and ω represents a rotation about boresight. γ and β are related to the antenna's E- and H-plane beamwidths as given in (2-2) and (2-3), respectively, and are used to map these beamwidths into a form that can be incorporated into the integration of (2-9) using (2-11).

Note that the angles ψ and ω in (2-11) are different from the integration variables expressed in (2-10). This is because the antenna may be pointed off-nadir by the angle ξ (see Figure 2.6), which is a major difference from previous volume scattering models [31,13]. In order to perform the integration, these antenna coordinate angles must be transformed to the integration angles; this is done by applying the laws of sines and cosines and a few trigonometric identities to obtain

$$\sin^2\omega = \frac{\tan^2\theta \sin^2(\phi - \phi_o)}{\tan^2\xi - 2\tan\xi \tan\theta \cos(\phi - \phi_o) + \tan^2\theta}$$
$$\sin^2\psi = 1 - \cos^2\xi \cos^2\theta \left[1 + \tan\xi \tan\theta \cos(\phi - \phi_o)\right]^2. \tag{2-12}$$

The antenna azimuth angle ϕ_o is assumed to be arbitrary, so it can be set to zero to simplify (2-12) without affecting the end result.

Substituting the scattering factor expression in (2-10) and the expression for the antenna pattern in (2-11) into the VSIR integral of (2-9) yields

$$P_{IR}(t) = \frac{G_o^2 \lambda^2 N_V \sigma_a}{(4\pi)^3} \int_0^{2\pi} \int_0^{\theta_u} \int_h^{\infty} \frac{\exp\left\{ -2k_e(r - r_i) - \frac{4}{\gamma}(1 + \beta \sin^2\omega)\sin^2\psi \right\}}{r^2}$$
$$\cdot \delta\left[t - 2\left(\frac{r_i}{c_o} + \frac{(r - r_i)}{c_s}\right)\right] T_b^2(\theta)\ \sin\theta\, dr\, d\theta\, d\phi. \tag{2-13}$$

Note that the unit step function has determined the upper limit of the θ-integral, as discussed above. The r-integration can be performed easily due to the presence of a delta function in the integrand. This sifting property simply converts all references to r into a time-dependent factor and Appendix B provides the details of this integration. Thus, after using the transformation equations in (2-12), (2-13) becomes, for $t \geq 2h/c_o$,

$$P_{IR}(t) = \frac{2G_o^2 \lambda^2 N_V \sigma_a c_s}{(4\pi)^3} \int_0^{\theta_u} T_b^2(\theta) \sin\theta \frac{\exp\left\{ -k_e\left[c_s t + 2h\, c_r \sec\theta\right] \right\}}{\left[c_s t + 2h \sec\theta(1 - c_r)\right]^2}$$
$$\cdot \int_0^{2\pi} \exp\left\{ -\frac{4}{\gamma}\left[1 + \beta\left(\frac{\tan^2\theta \sin^2\phi}{\tan^2\xi - 2\tan\xi \tan\theta \cos\phi + \tan^2\theta}\right)\right] \right.$$
$$\left. \cdot \left[1 - \cos^2\xi \cos^2\theta \left[1 + \tan\xi \tan\theta \cos\phi\right]^2\right] \right\} d\phi\, d\theta. \tag{2-14}$$

The relative speed of light within the medium, c_r, now appears in (2-14) which is defined as $c_r = c_s/c_o$. Equation (2-14) is expressed in terms of absolute time t, which includes the transit time of the impulse from the antenna through free space to the interface and back. This uneventful time can be eliminated by converting to *two-way ranging time*, τ, through $\tau = t - 2h/c_o$. This means that $\tau = 0$ corresponds to the instant in time where the propagating impulse just intersects the free space - random medium interface just below the altimeter and has propagated back to the receiver. Thus, (2-14) becomes

$$P_{IR}(\tau) = \frac{2G_o^2\lambda^2 N_V \sigma_a c_s}{(4\pi)^3} \int_0^{\theta_u} T_b^2(\theta)\sin\theta \frac{\exp\{-k_e[c_s\tau - 2hc_r(\sec\theta - 1)]\}}{[c_s\tau + 2h(c_r + \sec\theta(1-c_r))]^2}$$
$$\cdot \int_0^{2\pi} \exp\left\{-\frac{4}{\gamma}\left[1+\beta\left(\frac{\tan^2\theta\sin^2\phi}{\tan^2\xi - 2\tan\xi\tan\theta\cos\phi + \tan^2\theta}\right)\right]\right.$$
$$\left.\cdot\left[1-\cos^2\xi\cos^2\theta\left[1+\tan\xi\tan\theta\cos\phi\right]^2\right]\right\} d\phi\, d\theta, \qquad \tau \geq 0, \tag{2-15}$$

where $\theta_u = \cos^{-1}\left(\frac{1}{c_o\tau/2h+1}\right)$.

A simplification can be made to (2-15) if it is assumed that the radar is restricted to near-nadir pointing. If this is true, then θ is always relatively small and $\sec\theta \approx 1$ and the denominator in the θ-integral reduces to $[c_s\tau + 2h]^2$. In this case, the VSIR form is

$$P_{IR}(\tau) = \frac{2G_o^2\lambda^2 N_V \sigma_a c_s}{(4\pi)^3(c_s\tau + 2h)^2} \int_0^{\theta_u} T_b^2(\theta)\sin\theta\exp\{-k_e[c_s\tau - 2hc_r(\sec\theta - 1)]\}$$
$$\cdot \int_0^{2\pi} \exp\left\{-\frac{4}{\gamma}\left[1+\beta\left(\frac{\tan^2\theta\sin^2\phi}{\tan^2\xi - 2\tan\xi\tan\theta\cos\phi + \tan^2\theta}\right)\right]\right.$$
$$\left.\cdot\left[1-\cos^2\xi\cos^2\theta\left[1+\tan\xi\tan\theta\cos\phi\right]^2\right]\right\} d\phi\, d\theta, \qquad \tau \geq 0. \tag{2-16}$$

The θ-integration need only be performed up to the point where the antenna pattern gain drops off to some small value. This would be when θ_u is roughly equal to the pointing angle plus one beamwidth. This yields a practical limit for very small error in the denominator term, say 2%; θ can be as large as 11° ($\sec 11° = 1.019 \approx 1$). For a narrow beamwidth altimeter, on the order of 1°, this means that the antenna can be pointed up to about 10° off-nadir and (2-16) can be used with little error. For the remainder of this chapter, this approximation will be used; however, it is important to realize when this approximation may not be used.

The VSIR form in (2-16) is valid for arbitrary antenna pointing angle, antenna power pattern beamwidth and radar height. The effects of the antenna pattern, indicated by parameters γ and β, are completely contained within the ϕ-integral. The effect of the medium, described by k_e, is independent of ϕ but influenced by the polar angle θ. Note that (2-16) contains a double integral which cannot be simplified further without making

limiting assumptions. Furthermore, the upper limit of the θ integral is *time dependent*, meaning that for every discrete time value that a point on the model waveform is desired, a two-dimensional integration must be performed. This easily can be a costly computation if many evaluations are required. Clearly, finding possible simplifications for (2-16) which would reduce the amount of time required to compute a VSIR waveform is desirable. Fortunately, two helpful simplifications exist that can be used to supplement (but not completely replace) (2-16) and reduce the computation time.

2.2.2 Nadir Form of the Impulse Response

For the case when the radar altimeter antenna is pointed directly downward, substantial simplification of (2-16) is possible. When $\xi = 0^\circ$, the ϕ-integrand terms that were transformed by equations (2-12) reduce considerably;

$$P_{IR}(\tau) = \frac{2G_o^2\lambda^2 N_V \sigma_a c_s}{(4\pi)^3(c_s\tau + 2h)^2} \int_0^{\theta_u} T_b^2(\theta)\,\sin\theta \exp\{ -k_e[c_s\tau - 2hc_r(\sec\theta - 1)]\}$$

$$\cdot \int_0^{2\pi} \exp\left\{ -\frac{4}{\gamma}\left(1 + \beta\sin^2\phi\right)\sin^2\theta \right\} d\phi\, d\theta, \quad \tau \geq 0. \tag{2-17}$$

With the aid of a trigonometric identity, the ϕ-integrand in (2-17) can be manipulated into the form

$$P_{IR}(\tau) = \frac{2G_o^2\lambda^2 N_V \sigma_a c_s}{(4\pi)^3(c_s\tau + 2h)^2} \int_0^{\theta_u} T_b^2(\theta)\,\sin\theta \exp\{ -k_e[c_s\tau - 2hc_r(\sec\theta - 1)]\}$$

$$\cdot \exp\left\{ -\frac{4\sin^2\theta}{\gamma}\left(1 + \frac{\beta}{2}\right) \right\} \int_0^{2\pi} \exp\left\{ \frac{2\beta\sin^2\theta}{\gamma}\cos 2\phi \right\} d\phi\, d\theta, \tag{2-18}$$

for $\tau \geq 0$. Now the exponential factor in the ϕ-integrand of (2-18) can be rewritten in terms of a series of modified Bessel functions [1] to obtain

$$P_{IR}(\tau) = \frac{2G_o^2\lambda^2 N_V \sigma_a c_s}{(4\pi)^3(c_s\tau + 2h)^2} \int_0^{\theta_u} T_b^2(\theta)\sin\theta \exp\{ -k_e\left[c_s\tau - 2hc_r(\sec\theta - 1)\right]\}$$
$$\cdot \exp\left\{ -\frac{4\sin^2\theta}{\gamma}\left(1 + \frac{\beta}{2}\right)\right\}$$
$$\cdot \int_0^{2\pi} \left\{ I_0\left[\frac{2\beta\sin^2\theta}{\gamma}\right] + 2\sum_{k=1}^{\infty} I_k\left[\frac{2\beta\sin^2\theta}{\gamma}\right]\cos 2k\phi \right\} d\phi\, d\theta, \quad \tau \geq 0, \quad (2\text{-}19)$$

where I_k are the modified Bessel functions of the first kind. The first (zero order) term of the ϕ-integrand in (2-19) does not depend on ϕ so its value is 2π times the integrand; the second part can be integrated term-by-term, and each term is dependent on $\cos 2k\phi$, which when integrated over the specified limits reduces to zero. Thus, (2-19) becomes

$$P_{IR}(\tau) = \frac{G_o^2\lambda^2 N_V \sigma_a c_s}{(4\pi)^2(c_s\tau + 2h)^2} \int_0^{\theta_u} T_b^2(\theta)\sin\theta \exp\{ -k_e\left[c_s\tau - 2hc_r(\sec\theta - 1)\right]\}$$
$$\cdot \exp\left\{ -\frac{4\sin^2\theta}{\gamma}\left(1 + \frac{\beta}{2}\right)\right\} I_0\left[\frac{2\beta\sin^2\theta}{\gamma}\right] d\theta, \quad \tau \geq 0. \quad (2\text{-}20)$$

For nadir orientation of the antenna beam, a simplified result is obtained for the VSIR that has one less integration to be performed. (2-20) is simplified even further if the antenna pattern is circularly symmetric, i.e. $\beta = 0$. This makes $I_0[0] = 1$ and

$$P_{IR}(\tau) = \frac{G_o^2\lambda^2 N_V \sigma_a c_s}{(4\pi)^2(c_s\tau + 2h)^2} \int_0^{\theta_u} T_b^2(\theta)\sin\theta$$
$$\cdot \exp\left\{ -k_e\left[c_s\tau - 2hc_r(\sec\theta - 1)\right] - \frac{4\sin^2\theta}{\gamma}\right\} d\theta, \quad \tau \geq 0. \quad (2\text{-}21)$$

The elimination of the ϕ-integral in (2-20) and (2-21) serves to simplify the VSIR and thus speed up its computation considerably, but the conditions of $\xi = 0°$ and $\beta = 0$ severely restrict the use of this simplified version of the VSIR.

2.2.3 Asymptotic Approximation of the Impulse Response

When the pointing angle is not zero, the θ- and ϕ-integrals in (2-16) are not as readily accomplished by analytic techniques, as was possible for $\xi = 0°$. However, the parameter γ can be quite small when the antenna beamwidths are very narrow, as can be seen in (2-2). With γ very small ($\gamma \sim 10^{-4}$ for $\theta_b \approx 1°$), the argument of the exponential in the ϕ-integrand of (2-16) becomes very large. This makes the integrand very peaked in ϕ, which allows the ϕ-integral to be approximated by Laplace's method [3].

Laplace's method allows the integral of an exponential to be approximated by

$$\int_0^{2\pi} \exp\{W(\phi)\}d\phi \approx \exp\{W(\phi_o)\}\sqrt{\frac{-2\pi}{W''(\phi_o)}}, \tag{2-22}$$

where ϕ_o is a zero of the derivative of the exponential argument $W(\phi)$, i.e. $W'(\phi_o) = 0$. The first two derivatives of the argument of the exponential in the ϕ-integral in (2-16) are quite lengthy and messy and are excluded from this document. They were computed using Mathematica [39] and ϕ_o was found to have two repeating solutions: 0 and π. $\phi_o = 0$ corresponds to the maximum value of $W(\phi)$, which is the peaked region that Laplace's method requires for this approximation to be used. Thus, choosing $\phi_o = 0$, (2-22) can be applied to (2-16) to obtain

$$P_{IR}(\tau) \approx \frac{2G_o^2\lambda^2 N_V \sigma_a c_s}{(4\pi)^3(c_s\tau + 2h)^2} \int_0^{\theta_u} T_b^2(\theta)\sin\theta \exp\{-k_e[c_s\tau - 2hc_r(\sec\theta - 1)]\}$$
$$\cdot \exp\left\{-\frac{4}{\gamma}\left(1 - \cos^2\xi\cos^2\theta\left[1 + \tan\xi\tan\theta\right]^2\right)\right\}\sqrt{\frac{2\pi}{\alpha_v}}\,d\theta, \tag{2-23}$$

where

$$\alpha_v = \frac{8}{\gamma}\left[\beta\cos^2\xi\sin^2\theta + \cos(\theta - \xi)\sin\theta\sin\xi\right]$$

and $\tau \geq 0$. Once again the ϕ-integral is eliminated, but not without a cost. (2-23) is an approximation based on the value of γ, so the error introduced by its use must be examined.

2.2.4 Error Analysis for Asymptotic Approximation of the Impulse Response

The asymptotic approximation given by (2-23) should be used in place of the more computationally intensive (2-16) only when the error is sufficiently low, e.g. less than 2% of the true value say. To determine when this can be done, consider the general form for the VSIR given in (2-16) (with $\beta = 0$ for now);

$$P_{IR}(\tau) = \frac{2G_o^2\lambda^2 N_V \sigma_a c_s}{(4\pi)^3(c_s\tau + 2h)^2} \int_0^{\theta_u} T_b^2(\theta)\sin\theta \exp\{ -k_e\left[c_s\tau - 2hc_r(\sec\theta - 1)\right]\}$$

$$\cdot \int_0^{2\pi} \exp\left\{ -\frac{4}{\gamma}\left[1 - \cos^2\xi\cos^2\theta\left[1 + \tan\xi\tan\theta\cos\phi\right]^2\right]\right\} d\phi\, d\theta, \qquad (2\text{-}24)$$

with $\tau \geq 0$ and θ_u as in (2-16). The important part of this expression is the ϕ-integral because it is what is being approximated by Laplace's method. With the use of a trig identity, the ϕ-integral can be manipulated into a form that is similar to that used in the flat surface impulse response model used by Brown [9];

$$\int_0^{2\pi} \exp\left\{ -\frac{4}{\gamma}\left[1 - \cos^2\xi\cos^2\theta\left[1 + \tan\xi\tan\theta\cos\phi\right]^2\right]\right\} d\phi$$

$$= \exp[c]\int_0^{2\pi} \exp\{a\cos\phi - b\sin^2\phi\}\, d\phi, \qquad (2\text{-}25)$$

where

$$a = \frac{2}{\gamma}\sin 2\xi \sin 2\theta,$$

$$b = \frac{4}{\gamma}\sin^2\xi \sin^2\theta,$$

$$c = -\frac{4}{\gamma}\left[1 - \cos^2\xi\cos^2\theta - \sin^2\xi\sin^2\theta\right].$$

The expressions for a, b and c are different here, but the form is identical to that in [9] The integral on the right hand side of (2-25) can be expressed in terms of a series of

Bessel functions,

$$\exp[c]\int_0^{2\pi}\exp\{a\cos\phi - b\sin^2\phi\}d\phi$$
$$= 2\sqrt{\pi}\exp[c]\sum_{n=0}^{\infty}\frac{(-1)^n\Gamma(n+1/2)}{\Gamma(n+1)}\left(\frac{2b}{a}\right)^n I_n[a], \tag{2-26}$$

or alternatively approximated by Laplace's method,

$$\exp[c]\int_0^{2\pi}\exp\{a\cos\phi - b\sin^2\phi\}d\phi$$
$$\approx \exp[c-b+a]\sqrt{\frac{2\pi}{a(1+2b/a)}}. \tag{2-27}$$

The evaluation of the series in (2-26) is very difficult for large values of a, while the approximation given by the right-hand side of (2-27) is relatively easy to compute [9]. The error in using (2-27) in place of (2-26) will depend only on a and not on b, only if $a \gg b$ [9]. Examination of the equations for a and b shows this is indeed true. Numerical comparison in [9] of the two forms determined that to achieve less than 2% error in using (2-27) in place of (2-26), the necessary and sufficient condition is $a \geq 6.79$, or

$$\frac{2}{\gamma}\sin 2\xi \sin 2\theta \geq 6.79. \tag{2-28}$$

Note that this is a condition on θ and ξ, not on ξ and τ as was the case for the surface model [9,26] (cf. (2-6)). Thus, the asymptotic form in (2-27) can only be used with less than 2% error when

$$\theta \geq \theta_m = \frac{1}{2}\sin^{-1}\left[\frac{6.79\gamma}{2\sin 2\xi}\right]. \tag{2-29}$$

This condition is applied to the limits on the θ-integral of the VSIR, which are $[0, \theta_u]$. Figure 2.8 shows a plot of (2-29) for values of γ that correspond to beamwidths of 0.6° and 6.0° through (2-2). This figure indicates what values of ξ and θ allow the use of the asymptotic form of the ϕ integral portion of the VSIR in place of the numerical integral form. The full double-integration of (2-16) must be done over $[0, \theta_m]$, then the asymptotic

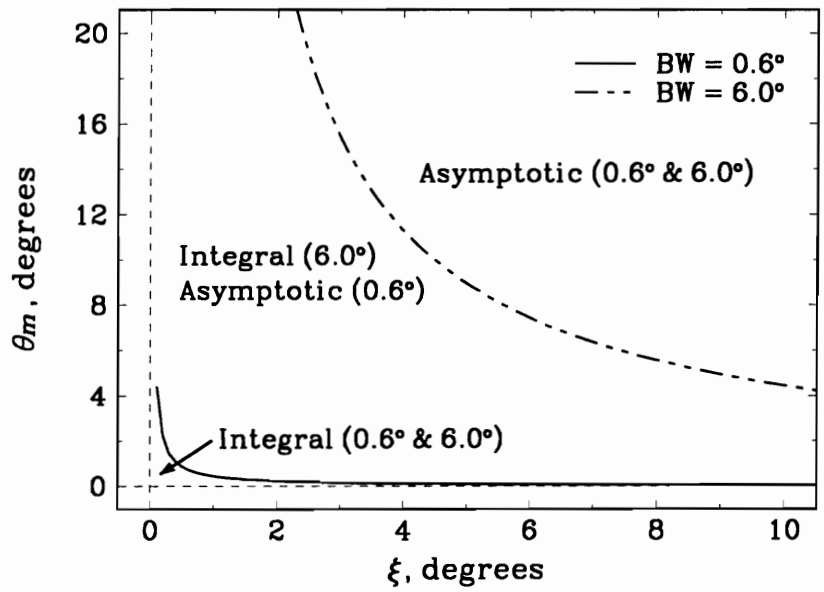

Figure 2.8. Plot of (2-29) for beamwidths of 0.6° and 6.0°. For a pointing angle ξ, regions are indicated where either the asymptotic form (2-23) or full integral form can be used for the VSIR.

form in (2-23) can be used to perform the remaining portion of the θ-integral over $[\theta_m, \theta_u]$. The VSIR algorithm must then be capable of splitting the θ-integral into two parts to correctly evaluate the impulse response using the asymptotic form.

The condition given in (2-29) depends only on the antenna pointing angle and beamwidth parameters. As the pointing angle increases, θ_m decreases, thus allowing the asymptotic form to be used for a larger portion of the total θ-integration. Likewise, a smaller antenna pattern beamwidth (which decreases γ, see (2-2)) also decreases θ_m. Note that this condition does not depend on the altitude h, as does the corresponding condition for the surface model in (2-6) [26].

When the antenna pattern must be described by an elliptical Gaussian, β is not zero. The condition in (2-29) must then be modified because it was derived for $\beta = 0$. It has already been established that the parameter γ is dependent on the beamwidth through (2-2), and θ_m is dependent on γ. If γ is then computed based on the larger of the two principle-plane beamwidths and that value is used in (2-29), the larger and more conservative of the two possible values for θ_m will be obtained. Using the more conservative value of θ_m assures that the θ-integration will be accurate to less than 2% error.

2.2.5 The Pulse Response

With the above expressions for the volume scattering impulse response, all that remains to be done to obtain the volume scattering pulse response is to convolve the appropriate form of the VSIR in either (2-16), (2-20) or (2-23) with the point target response, e.g.,

$$V(\tau) = P_{IR}(\tau) \otimes P_{PT}(\tau), \tag{2-30}$$

where $\otimes$ is the convolution operator. The PTR can be measured for a given altimeter, but for short pulse systems a Gaussian pulse is usually an adequate approximation [8] as noted previously. The convolution is easily performed by an FFT method [7], whether the PTR is measured or closed-form Gaussian.

Examples of the modeled pulse responses are given in Figures 2.9 and 2.10 for pointing angles of 0° and 12°. Figure 2.9 shows sample waveforms for the same MARA system parameters as for Figure 2.2. The waveforms in Figure 2.10 are examples that

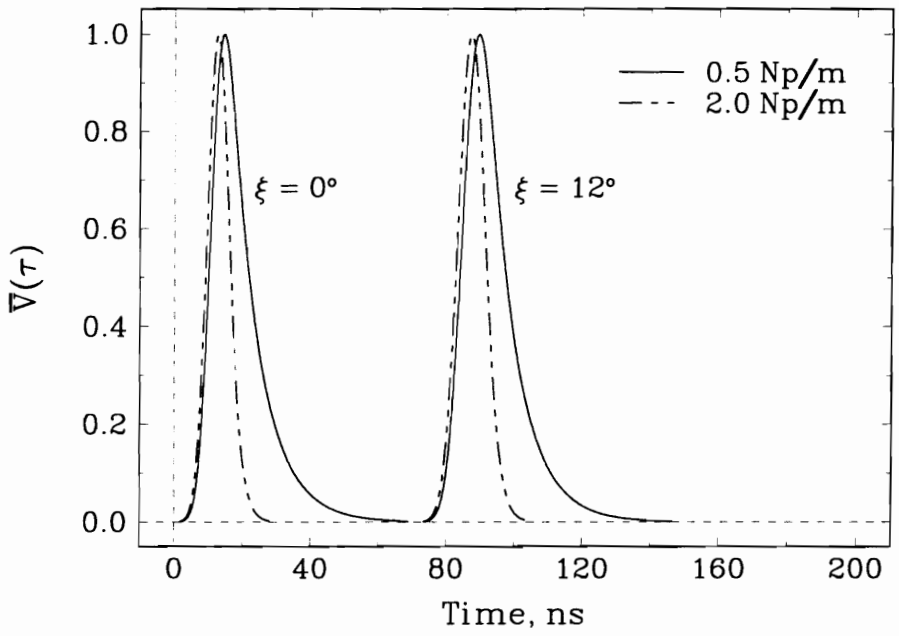

Figure 2.9. Modeled volume scattering waveforms for a beamwidth-limited altimeter. The altitude is 500 m, beamwidth is 0.6° and pulsewidth is 6.5 ns. Shown are two values of extinction coefficient, 0.5 Np/m (solid) and 2.0 Np/m (dashed), and antenna pointing angles of 0° and 12°. The waveform shapes are very similar for the different pointing angles.

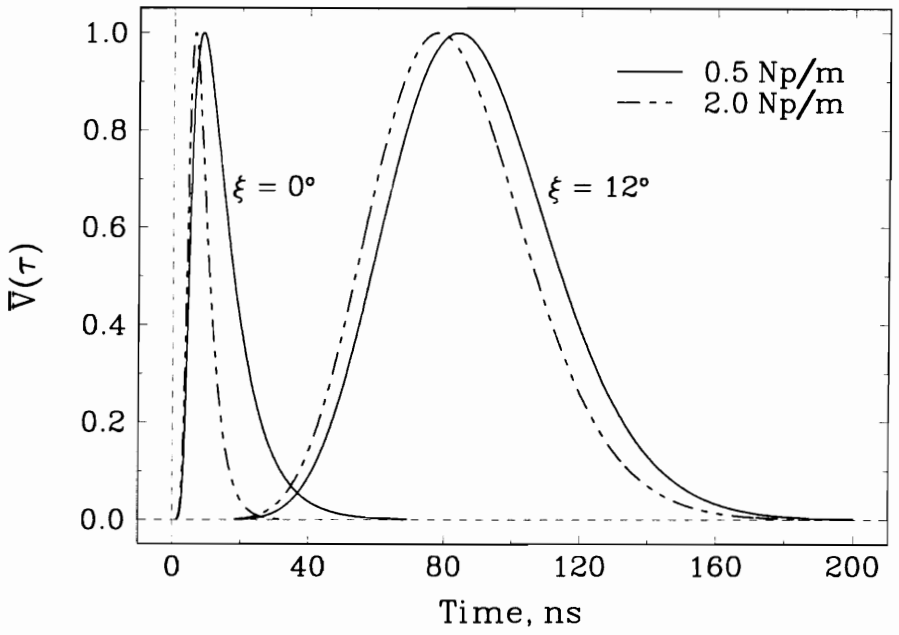

Figure 2.10. Modeled volume scattering waveforms for a pulsewidth-limited altimeter. The altitude is 500 m, beamwidth is 6° and pulsewidth is 2 ns. Shown are two values of extinction coefficient, 0.5 Np/m (solid) and 2.0 Np/m (dashed), and antenna pointing angles of 0° and 12°. The waveforms are very dissimilar for different pointing angles in this case.

correspond to the same modified MARA system configuration used in Figure 2.3. In both curves, the extinction coefficient dependence is demonstrated as k_e is either 0.5 or 2.0 Np/m. Since the extinction coefficient is the reciprocal of the penetration depth [11], these values correspond to depths of 2.0 and 0.5 meters, respectively. The extinction coefficient has the greatest effect on the trailing edge region of the volume scattering waveforms, particularly for the beamwidth-limited returns.

The example waveforms in these figures indicate the radical difference in the behavior of beamwidth- and pulsewidth-limited systems. As for the surface model example, the beamwidth-limited system is much less sensitive to pointing angle at this low altitude, as indicated by the very similar shapes of the waveforms in Figure 2.9. At the same time, the effects of the extinction coefficient are independent of ξ. In Figure 2.10, the shapes are markedly different as the pointing angle changes, and the extinction coefficient dependence does not appear to be similar. In fact, the two waveforms for $\xi = 12°$ look very similar except for a time shift which could easily be attributed to a different pointing angle. Also notice that the 12° volume returns are very similar to the 12° surface returns in Figure 2.3, a further complication to trying to isolate the penetration effects on the waveforms. To illustrate these differences, Table 2.1 summarizes the half-power widths of the volume waveforms in Figures 2.9 and 2.10. Note that the ratio of widths, given in the last column, shows that the beamwidth-limited returns are much more insensitive to pointing angle than the pulsewidth-limited counterparts. A larger ratio indicates a greater difference, while a ratio near unity indicates that the two waveforms are very similar. Also note that the difference in the half-power width ratios between 0° and 12° for the beamwidth-limited waveforms are very similar, as opposed to those for the pulsewidth-limited waveforms. This indicates that the extinction effects are independent of ξ for beamwidth-limited, but not pulsewidth-limited systems. These desirable features of the beamwidth-limited system can be exploited to help determine the parameters of the observed medium, since the waveform behavior is relatively insensitive to pointing angle errors.

As was done for the surface model in Figures 2.4 and 2.4, example average waveforms for an altitude of 50 km are shown in Figures 2.11 and 2.12. Figure 2.11 compares the beamwidth- and pulsewidth-limited nadir returns for an extinction coefficient of 0.5 Np/m. Compare these to the nadir returns in Figures 2.9 and 2.10 and the significant difference in the waveform shapes become apparent. As the altitude

Table 2.1. Waveform width comparison for Figures 2.9 and 2.10.

Figure	k_e (Np/m)	ξ (°)	HPW (ns)	HPW Ratio (12°/0°)
2.9	0.5	0	11.9	
		12	13.7	1.15
	2.0	0	7.5	
		12	9.3	1.24
2.10	0.5	0	13.3	
		12	56.3	4.23
	2.0	0	6.7	
		12	53.3	7.96

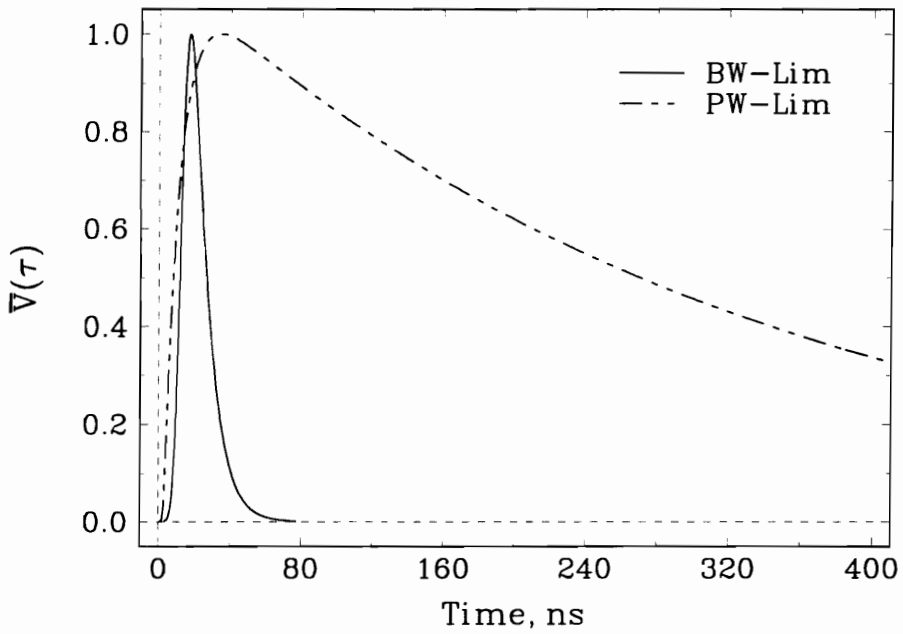

Figure 2.11. Example of the beamwidth- and pulsewidth-limited volume scattered waveforms for an altitude of 50 km. The pointing angle is nadir and the extinction coefficient, k_e, is 0.5 Np/m.

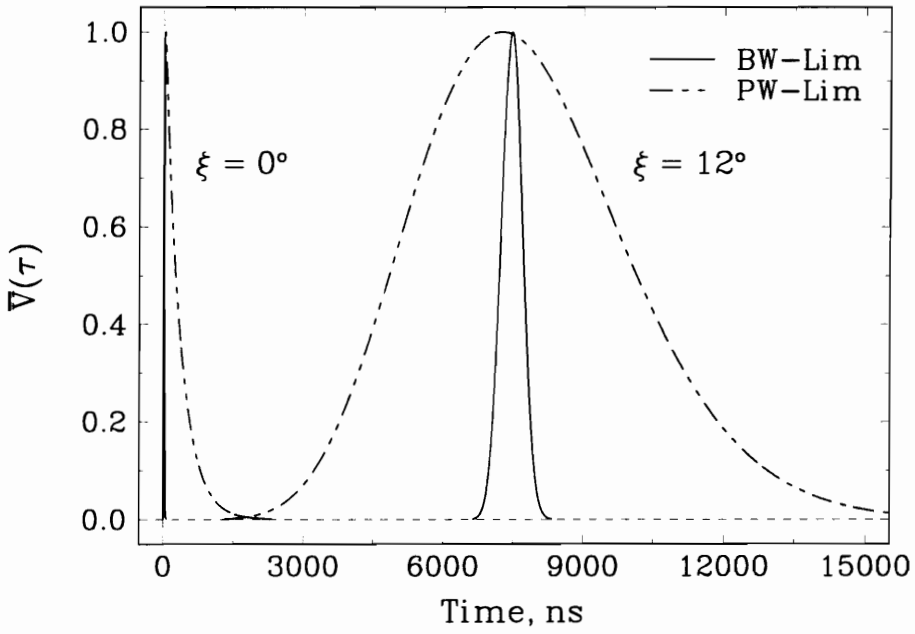

Figure 2.12. Example of the beamwidth- and pulsewidth-limited volume scattered waveforms at an altitude of 50 km for both nadir and 12° pointing angles. The extinction coefficient, k_e, is 0.5 Np/m.

increases, the waveform width for the pulsewidth-limited returns increases much more than the beamwidth-limited returns. This makes extinction coefficient determination more difficult for a pulsewidth-limited altimeter because a small change in k_e makes a less apparent change in waveform shape.

Figure 2.12 shows the same nadir returns in Figure 2.11 along with the corresponding returns for a 12° pointing angle. Notice that the time scale has changed dramatically when compared to previous figures. This makes the beamwidth-limited nadir return appear near $\tau = 0$ as something like a delta function by comparison. These wider waveforms are more difficult to use in determining the change in extinction coefficient. A beamwidth limited system, especially at lower altitudes, is more effective at discriminating extinction coefficient changes. This feature is similar to the way it can discriminate between surface roughness changes, as was demonstrated in the previous section.

2.3 The Combined Surface and Volume Scattered Waveform Model

The volume scattered pulse response can now be combined with the surface scattered pulse response to model the actual returns from a random medium such as ice or snow. The two models are combined by adding the waveforms together, paying particular attention to the timing of the waveforms. This is especially important when modeling waveforms for beamwidth limited, low altitude systems such as MARA [28]. The return waveforms for this system are very narrow, unlike conventional pulsewidth limited satellite altimeter waveforms (cf. Figures 2.2 and 2.9 to Figures 2.3 and 2.10).

When adding the surface and volume models together, they cannot simply be added with equal weighting because there are varying physical conditions where at times the surface scattering may dominate the volume scattering or vice versa. An example of this occurs in Greenland. The *dry snow* region of Greenland [4], characterized by higher elevations and latitudes, exhibits negligible surface scattering at microwave frequencies. Conversely, the *soaked* region [4], located in the coastal zones of Greenland, experiences significant surface melting in the summer, thus giving rise to surface scattering only. So when designing an algorithm for fitting altimeter waveforms with the model, a parameter that will vary is the *combination ratio*, η, which is used in

$$
\begin{aligned}
C(\tau) &= S(\tau) + V(\tau) \\
&= \widehat{S}\overline{S}(\tau) + \widehat{V}\overline{V}(\tau) \\
&= \widehat{S}\left[\overline{S}(\tau) + \frac{\widehat{V}}{\widehat{S}}\overline{V}(\tau)\right] = \widehat{S}\left[\overline{S}(\tau) + \eta\overline{V}(\tau)\right],
\end{aligned}
\tag{2-31}
$$

where $C(\tau)$ is the combined scattered waveform and $S(\tau)$ is the surface scattered model given by (2-7) and $V(\tau)$ is the volume scattered model in (2-30). The quantities $\widehat{S}$ and $\widehat{V}$ are the peak values of the surface and volume scattered waveforms, respectively; $\overline{S}(\tau)$ and $\overline{V}(\tau)$ are then the *normalized* scattered waveforms. η can vary from zero (all surface scattering) to infinity (all volume scattering). In the data fitting portion of this research, a practical limit is placed on η to confine the parameter search to a finite range. Examples of the combined surface and volume scattered waveforms are shown in Figures 2.13 and 2.14.

The surface scattered waveforms used in Figures 2.13 and 2.14 are the same as the surface examples in Figures 2.2 and 2.3 for $\sigma_h = 0.2$ meters. The volume scattered waveforms used in these figures are those from Figures 2.9 and 2.10 for $k_e = 0.5$ Np/m. Figure 2.13 shows these modeled waveforms for (a) beamwidth-limited and (b) pulsewidth-limited altimeters, varying combination ratio, η, and nadir orientation. Compared to previous figures, the time scale has been halved to permit a more detailed view. The value $\eta = 1$ represents the case where the surface and volume waveform peak values are equal. While this situation is possible, in practice it is quite unlikely that for a given span of altimeter data the relative contributions from surface and volume scattering are identical. In fact, it may be more likely that the measured average altimeter waveforms will look more like either the case of $\eta = 0.33$ or $\eta = 3$. These two values correspond to the situation of 75% surface to 25% volume contribution and vice-versa. For either case of beamwidth- or pulsewidth-limited nadir waveforms, the waveform shapes are quite different as η changes.

Figure 2.14 shows the combined waveforms for the same extinction coefficient, k_e, and rms surface height, σ_h, as in Figure 2.13, but for an off-nadir pointing angle of 12°. The difference between Figures 2.14(a) and (b) is significant. Notice that as η changes, the beamwidth-limited waveforms in Figure 2.14(a) change shape considerably in the tail region, while the pulsewidth-limited waveforms in Figure 2.14(b) retain the same basic shape but are shifted in time. In fact, the effect of varying η to obtain the pulsewidth-

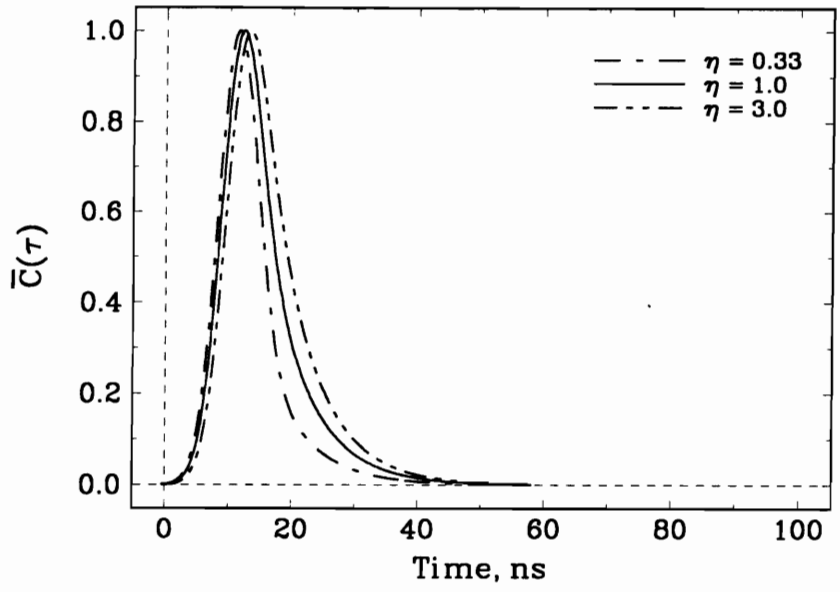

(a)

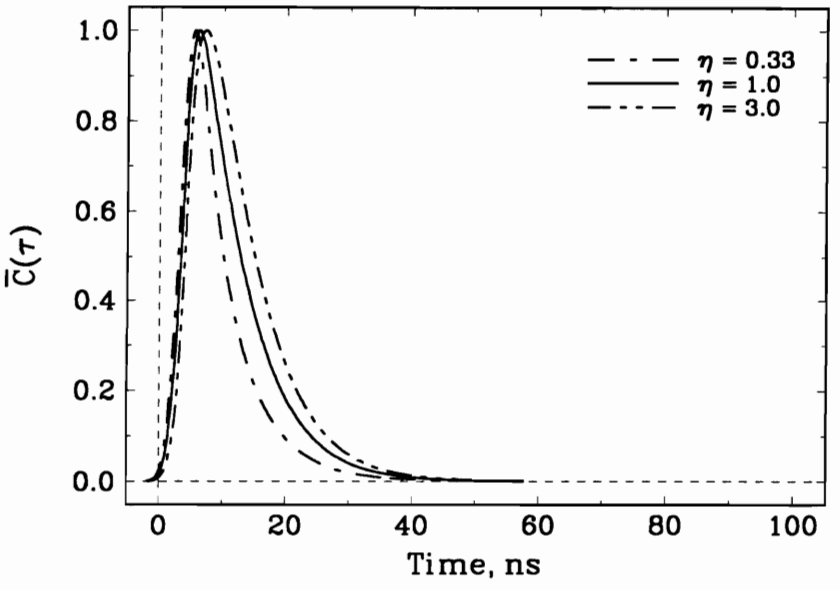

(b)

Figure 2.13. Examples of the combined scattered waveforms for (a) beamwidth- and (b) pulsewidth-limited altimeters at nadir orientation. The combination ratio, η, varies from 0.33 to 3.

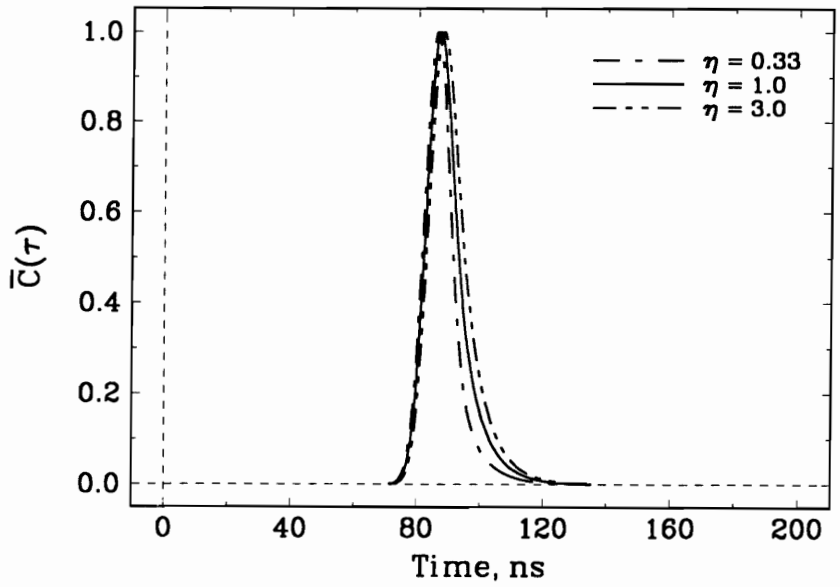

(a)

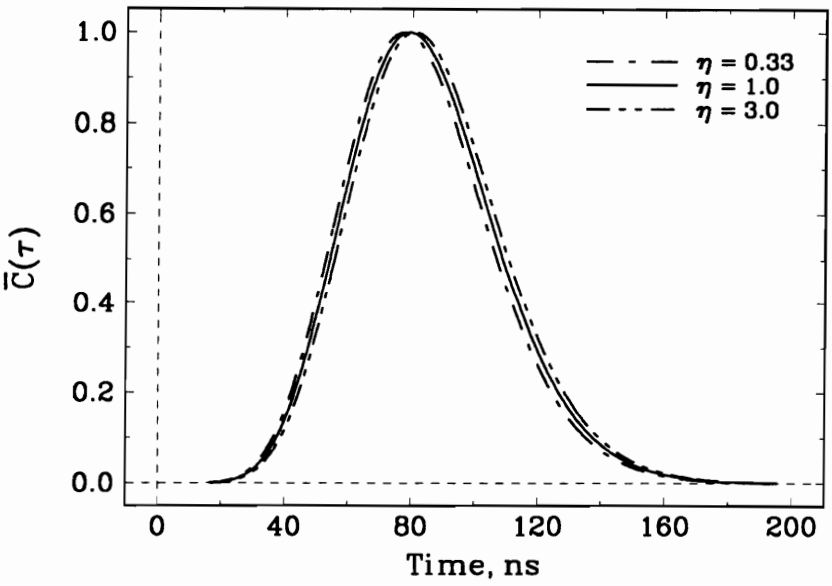

(b)

Figure 2.14. Examples of combined scattered waveforms for (a) beamwidth- and (b) pulsewidth-limited altimeters at 12° off-nadir pointing angle. The combination ratio, η, varies from 0.33 to 3. Notice the significant difference in the beamwidth-limited waveform behavior while the pulsewidth-limited waveform seems to only shift in time as η varies.

limited waveforms in Figure 2.14(b) is no different than changing the antenna pointing angle slightly. *For this reason, the pulsewidth-limited altimeter cannot distinguish the difference between pointing errors and surface/volume scattering contributions. The beamwidth-limited altimeter is relatively insensitive to pointing angle, even to many beamwidths off-nadir, so it is more suitable to detecting penetration effects.*

As an example of how well this approach models the returns from the ice sheet, the combined surface and volume scattering model will be compared to real data. MARA data from the September 1991 mission to Greenland is compared to the combined model in Figure 2.15. In this example, the pulse responses from near nadir are examined. The three unknown model parameters are crudely varied by hand to obtain the "best fit" seen in Figure 2.15

These data were obtained from the upper elevations of the ice sheet, well into the dry snow region where penetration is most likely to occur. For the surface model, the rms roughness σ_h is varied to provide the best fit to the leading edge region of the return waveform; for this example the best fit is for $\sigma_h = 0.25$ meters. The extinction coefficient is varied in the volume model to provide the best fit in the tail region of the waveforms. The models are then combined according to the mixing ratio η. Figures 2.15(b-d) show various combinations of k_e and combination ratio η. Any of these provides a good fit, but note that the mixing ratio varies from only 0.43 (70% surface, 30% volume contributions) all the way up to ∞ (100% volume contribution) and the corresponding penetration depth varies from 200 to 83 cm. While this example demonstrates how the combined model can be used to account for the volume penetration effects on the altimeter waveforms, it is clear that a more automated procedure is needed to find the best combination of parameters to achieve a best fit. This is the subject of the next chapter.

This example shows how important it is to account for the extinction caused by the medium as we attempt to measure the effects of scattering from the ice sheet. This example showed that there is some penetration into the ice sheet at 36 GHz, so there must also be some for lower frequencies [37]. Since there are operational altimeters at these lower frequencies, accounting for waveform penetration in the modeling of the altimeter returns is obviously important.

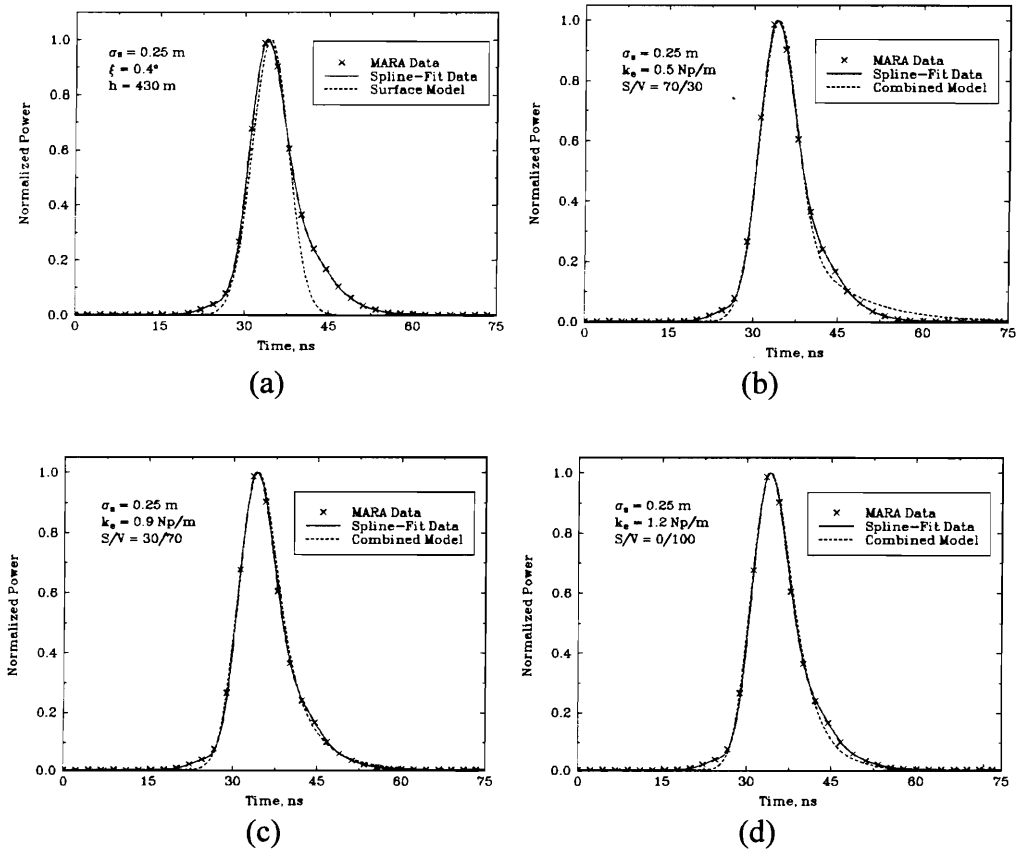

Figure 2.15. Comparison of measured altimeter data to the combined surface and volume scattering model. For the data, 950 waveforms are averaged (10 second averaging time), the pointing angle is 0.4° and the altitude is 430 meters. In (a), the data are fit to only the surface model with $\sigma_h = 0.25$ meters, revealing that medium penetration is occurring. The remaining figures show the combined model fit to the data for $\sigma_h = 0.25$ meters with respective k_e and η values of (b) 0.5 Np/m, 0.43; (c) 0.7 Np/m, 2.33; and (d) 1.2 Np/m, ∞.

2.4 Capabilities and Limitations of the Model

As in any case where a model is used to represent some physical process, it is important to realize that there are certain capabilities and limitations that must be considered before it can be used to analyze altimeter data. For the combined model, an important concept is that all the effects of the rough interface are included in the surface model only. Whether or not this is a positive feature, it serves to simplify the volume model considerably.

If the interface roughness were accounted for in the volume model, it would have to be included in the argument of the exponential factor for extinction as a random variable in the $r - h\sec\theta$ expression. The upper limit of the θ-integral would also have to include the random nature of where the impulse intersects the rough surface. Thus, including a randomly rough interface in the volume model is much more complicated than for the surface model, which was a simple convolution with the surface height pdf. As used in this work, the combined model can be applied with the most confidence to a randomly rough surface over a penetrable media in cases where the roughness is not too large in terms of electromagnetic wavelengths. Such is the situation in the higher elevations of the ice sheets.

Another limitation of the combined model is in the use of η to describe the relative contributions of surface and volume scattering. The limits on η are $[0, \infty)$, but in practice the upper limit is unreasonable. Using this limit in the combined model would cause a numerical overflow in the computation, so practical limits on η must be set. A brief study of the dependence of features like the half-power width, area, centroid and leading- and trailing-edge slopes of a combined model waveform concluded that η could be limited to a range of $[0.1, 10]$. Any values of η beyond these limits causes no significant change to the waveforms.

These limits correspond to cases where the volume-to-surface strength is 1/10 and 10. Increments over this range are best performed in logarithmic-space, i.e. over the range of $\log \frac{1}{10} = -1$ to $\log 10 = 1$. In log space, an increment of 0.1 or 0.05 will provide a uniform sampling of η over this range

The remaining capabilities and limitations of the combined model are discussed in terms of its components, the surface and volume scattering models.

2.4.1 The Surface Model

The surface model can be used up to many beamwidths off-nadir with excellent results [26]. While the Gaussian height pdf is commonly used, any pdf form that may provide a more accurate description of the surface statistics can easily be used in the model. The point target response is a function that can be easily measured once for an altimeter system and used in the model to account for the transmitter/receiver effects on the waveforms. Finally, since two of the three expressions given for the flat surface impulse response are closed form, the model can be computed very rapidly with the aid of FFTs [7] to make parameter variation for model fitting feasible.

The limitations of this model include those given by Brown [8]. The model assumes that the illuminated surface is comprised of a sufficiently large number of random independent scatterers, which may or may not be a concern for low altitude, narrow beamwidth altimeters. A quick check to see if this condition is met is to compute the size of the altimeter's footprint (illuminated area). If the diameter is very large in terms of the surface height decorrelation length, then this condition is most likely met. It is confined to use near-nadir because a small off-nadir angle assumption was made to allow the random surface height variation to be represented by a convolution with the height pdf rather than within the impulse response itself [10]. Thus, it cannot be used for near grazing incidence, but fortunately this is not a problem in conventional altimetry. The model only describes incoherent scattering in the mean, assumes no polarization effects and the surface height statistics are assumed to be constant over the total illuminated area. It also requires that the variation of the scattering process with incidence angle is manifested in σ^o and the antenna gain pattern. Further, σ^o is assumed to vary slowly over the angular extent of the mean return. Finally, the total Doppler frequency spread due to the radial velocity between the radar and the surface is assumed small when compared to the bandwidth of the transmitted pulse.

2.4.2 The Volume Model

The capabilities of this method include the ability to model the volume scattered return waveforms for a general configuration of antenna beamwidth, transmitted pulsewidth, radar altitude and pointing angle. The point target response is the same as that used for the surface model, so it is already available without further computation or measurement. This model also has an advantage in that, as in previous work [31,13], it is

a simple "first order" approach to modeling the scattering process. It does not attempt to identify the particular mechanisms such as multiple scattering [17]; rather, it only attempts to identify a simple *effective parameter (or set of parameters)* that can be used to identify when volume scattering is present.

One of the limitations of this model is that it assumes the medium is comprised of a large number of independently distributed scatterers, which ignores multiple scattering effects. This may be a crucial point for the ice sheet of Greenland if the volume fraction of scatterers in natural snow is assumed to be in the range of 20-55% [37]. For a high volume fraction, the particles may be packed too close together to ignore multiple scattering. The model is also restricted to near-nadir use, because of the simplifying assumption made to obtain (2-16). This can be somewhat relaxed if the VSIR form in (2-15) is used instead. Another limitation that may be important is that the model as described above does not account for possible layering in the medium. This may be circumvented by modifying the volume scattering impulse response formulation to account for layering, which will inevitably lead to more complicated functions and increased evaluation times. This model collectively treats the scattering mechanisms in the medium between the air/ice sheet interface and volumetric shell by the use of an *effective* extinction coefficient and number density of particles. As previously stated, however, this model does not attempt to account for the individual scattering mechanisms. Since the extinction coefficient is also frequency dependent, direct comparison of derived values for extinction cannot be directly compared between altimeters with different frequencies. Some of these limitations, such as ignoring multiple scattering or possible layering, may need to be examined further as the model is used to describe the volume scattering contribution to the return waveforms for various random media types.

Chapter 3
Altimeter System Analysis

This chapter deals with the discussion and analysis of the Multimode Aircraft Radar Altimeter (MARA) [28] which was used to obtain the 1991 waveform data over the Greenland ice sheet that is analyzed in this and the next chapter. The MARA system is based at NASA Goddard Space Flight Center - Wallops Flight Facility. Table 3.1 provides a summary of the system parameters for MARA.

The MARA system generates five very narrow-beamwidth, high gain, independent beams pointed at nadir and at four off-nadir angles (forward, port, aft, starboard). Figure 3.1 shows how this is achieved. The off-nadir beams can be configured to point up to 15° off-nadir, but were all set to 12.5° for the data used in this thesis. The beamwidths are different for the nadir and off-nadir beams because of an astigmatism that results from the use of multiple pyramidal horns and a single lens to create multiple off-nadir beams. This beamwidth variation only occurs in the E-plane of the antenna while the H-plane has a nearly constant 0.6° beamwidth for all pointing angles from nadir to about 13° off-nadir. Because of the very short time expanse of the return waveforms that result from such a narrow beamwidth, the MARA system only needs to record 48 samples per waveform with 2.226 ns spacing between samples, resulting in a 106 ns (or 32 meter) time (range) window. The pulsewidth is somewhat adjustable, but is usually no shorter than 6.5 ns. The signal-to-noise ratios shown in Table 3.1 are calculated for both the nadir and off-nadir beams for an expected worst-case (minimum) σ^o value of $-23\,\mathrm{dB}$ [28]. Since there is no detailed reference that discusses the necessary post-processing of the MARA data, the following sections are provided to summarize those topics.

3.1 MARA Data System

The MARA system simultaneously transmits a single pulse through five antennas which are nominally pointed at nadir and 12.5° off-nadir in the forward, port, aft and

Table 3.1. Summary of the MARA system parameters. Values are taken from [28]. The S/N ratios are calculated for a σ^o value of -23 dB.

Parameter	Value
frequency (GHz)	36.0
intermediate (IF) frequency (MHz)	600
wavelength (mm)	8.33
peak power per channel (W)	200
nominal pulsewidth (ns)	6.5
bandwidth (MHz)	220
prf (Hz)	100
E-plane beamwidth - nadir (°)	0.6
- off-nadir (°)	0.9
H-plane beamwidth (°)	0.6
number of beams	5
antenna gain (dB)	46.0
number of samples/waveform	48
sample increment (ns)	2.226
receiver noise figure (dB)	10
S/N (at 1 km altitude) - nadir (dB)	25
- off-nadir (dB)	17.5

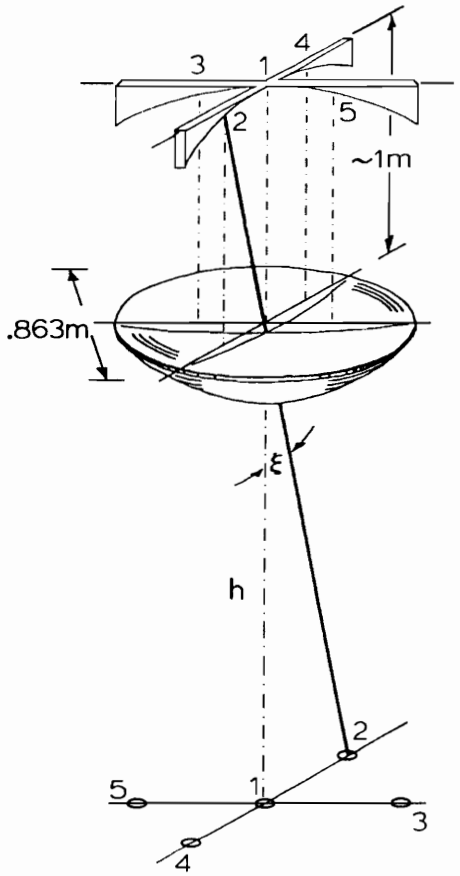

Figure 3.1. The MARA antenna system geometry [28]. The pyramidal horn antennas are located above the lens on the orthogonal arms at the numbered locations. The nadir horn is located at "1", the left horn at "2", the fore horn at "3", etc. Aircraft motion is from left to right.

starboard directions. While there is only one transmitter whose power is split among each of these beams, there are five individual receivers that digitize the five return pulses at a sample spacing of 742 picoseconds. These samples are then clustered in groups of three and averaged to obtain each sample point. This results in an effective sample spacing of 2.226 ns for 48 samples per waveform for each beam, which corresponds to the values quoted in Table 3.1. A computer-controlled AGC loop is incorporated in each receiver to ensure that the signal level of the return waveforms are kept within the dynamic range of each receiver. The AGC value, along with the threshold range, aircraft pitch and roll and time of day are recorded with the waveforms on the data tapes.

The data from this system must be processed before it can be compared with model waveforms. The processing includes AGC removal, detector correction, determination of true pointing angles, waveform retracking and waveform splining.

3.1.1 Nonlinear MARA Detector Correction

After the 1991 Greenland experiment, it was found that the MARA detectors in the receiver subsystem do not operate as linearly as designed. The waveform data must be corrected for this non-linear amplitude conversion. The waveform data are digitized into one of 256 amplitude levels after the AGC loop centers the waveform within the dynamic range of the receiver. To perform the amplitude correction, the waveform data is first multiplied by an AGC-dependent factor to return the waveform amplitude to its pre-AGC level.

The AGC value has units of 1/4 dB steps of *power attenuation*, so the AGC factor can be written as

$$F = 10^{\left\{\frac{1}{10}\left[\frac{AGC}{4}\right]\right\}}. \tag{3-1}$$

As an example, an AGC value of 140 means that $140/4 = 35$ dB attenuation was used to keep the return waveform within the dynamic range of the digitizer. The AGC factor, from (3-1), is then 3.16×10^3. Larger AGC values translate into a larger AGC factor F, which results in a larger waveform amplitude. Each sample $P_s(\tau_i)$ of a particular waveform is then multiplied by the factor F for that waveform's AGC value. This results in a pre-corrected waveform given by

$$P_{pre}(\tau_i) = F\, P_s(\tau_i) \tag{3-2}$$

where $i = 1, 2, \ldots, 48$.

The tunnel diode detectors used in the MARA receivers are designed to be square-law devices, so in terms of power they should be linear devices. A bench test performed at NASA - Wallops Flight Facility revealed that for power levels of 0.8 W and higher the detectors are not linear [38]. That test used a 600 MHz continuous-wave (CW) signal to provide an input-to-output power relationship. This frequency was used because it is the same as the IF frequency of each receiver. Figure 3.2 shows a plot of the data from this test and the nonlinear behavior of the MARA detector is clearly obvious. These data points are fit with a cubic function, which is shown as the solid line in the figure. Using this fit results in a post-corrected waveform amplitude that can be expressed as

$$P_{post}(\tau) = 10\big[c_1 + c_2\big(c_3 + c_4 x + c_5 x^2 + c_6 x^3\big)\big], \tag{3-3}$$

where $x = \frac{1}{10}\, P_{pre}(\tau_i)$, $x > 8$ and

$$\begin{aligned} c_1 &= -0.01484, & c_2 &= 242.944, \\ c_3 &= -0.0118, & c_4 &= 0.005721, \\ c_5 &= -3.853(10)^{-5}, & c_6 &= 1.042(10)^{-6}. \end{aligned}$$

This correction is used on all of the MARA data that is analyzed in this dissertation.

This correction method is rather crude since it was performed only for one frequency, i.e. the intermediate frequency of the MARA receivers. The best possible correction method would be based on the system transfer function of the detector over the entire 200 MHz receiver bandwidth. As of this writing, such a test has not been performed because the MARA recording system was shared with the Surface Contour Radar (SCR) [28]. The SCR rendered the system inaccessible until it was damaged when the transmitter overheated and failed during operation; it has not yet been repaired.

It is also thought (but not confirmed) [38] that an extremely high AGC value, e.g. anything greater than 160 AGC units (or 40 dB attenuation), causes unknown distortion of the recorded waveforms that cannot be corrected by (3-3). Thus, the AGC level must be closely monitored when data analysis is performed. For now, any waveform data that has an AGC value of more than 160 is subject to unknown error.

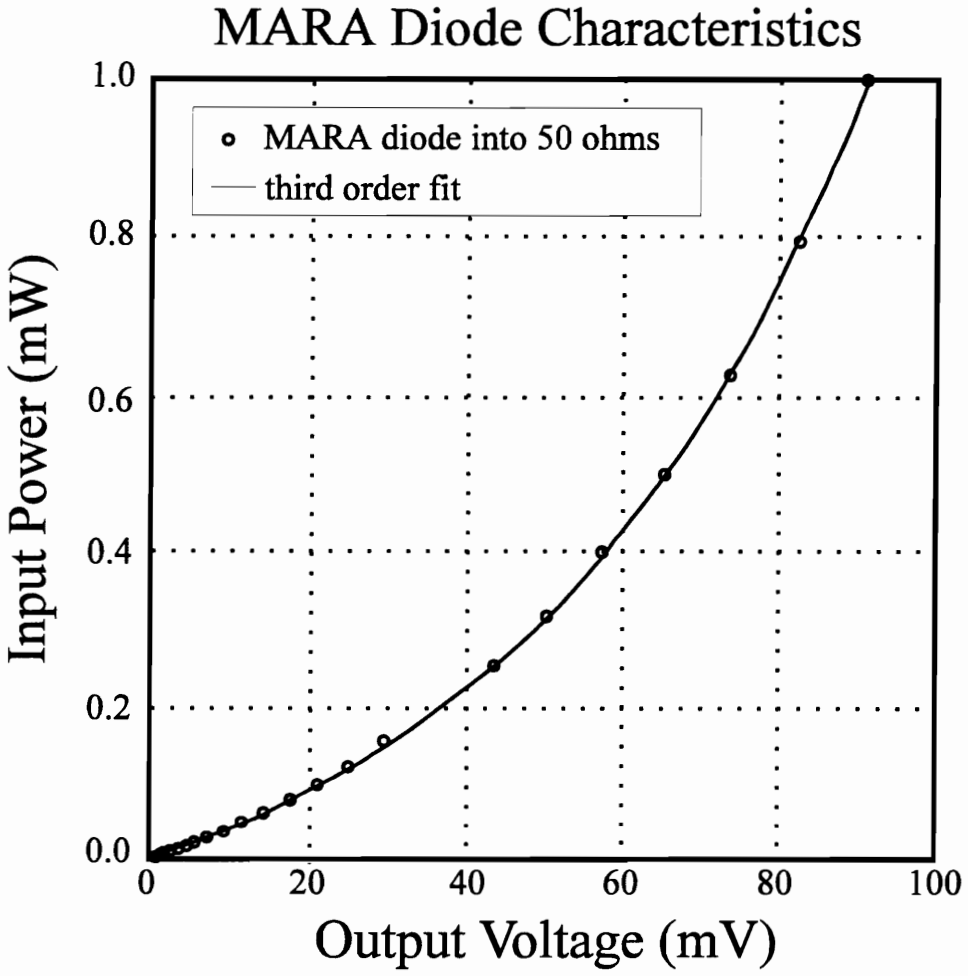

Figure 3.2. Plot of the MARA detector's nonlinear input power vs. output voltage relationship. From [38].

3.1.2 Pointing Angle Determination

The MARA system records the Internal Navigation System (INS) values of the aircraft's pitch and roll attitude as part of the data record for each received waveform. These values are known be accurate to at least one-tenth of a degree [38]. Each of the five beams has a known nominal pointing angle, so for a given waveform from one of the beams the actual pointing angle can be determined. The original pointing angles must be transformed into the actual pointing angles by making the use of an Eulerian angle transformation [30]. The actual angles are required as an input to the waveform model in Chapter 2.

Since the MARA beamwidth is less than one degree, pointing errors of more than one degree will adversely affect the resulting modeled waveform, especially for larger altitudes. This can be seen in the plot shown in Figure 3.3. The two curves show the behavior of the half-power width (in ns) vs. antenna pointing angle of the MARA surface scattered waveforms for altitudes of 500 and 5000 meters. Notice that the lower altitude curve is relatively flat when compared to that for the higher altitude. The need for accurate pointing knowledge is thus apparent since pointing angle errors can be misinterpreted as changes in surface roughness or medium extinction, as described in Chapter 2.

Figure 3.4 shows two Cartesian coordinate systems, denoted by the primed and unprimed axes. The angles α, β and γ are used to define the Eulerian angles, which represent the rotation angles between the two coordinate systems. The primed system is used to represent the aircraft orientation before the pitch and roll has occurred. The unprimed system represents the aircraft orientation after the pitch and roll angles have been accounted for. For the MARA system, the z-axis in Figure 3.4 is taken to be the forward direction of the aircraft, the x-axis corresponds to the starboard direction and the y-axis points directly toward nadir. Using this orientation, α, β and γ correspond to roll, pitch and yaw angles of the aircraft, respectively. The MARA system does not record the aircraft yaw angle, which is a measure of where the nose of the airplane is pointed. During normal flight it is usually very small, so it can be assumed to be zero in the following discussion. This does not cause a problem because a small change in the yaw angle creates a negligible change in actual pointing angle.

The transformation equation for conversion between the unprimed and primed

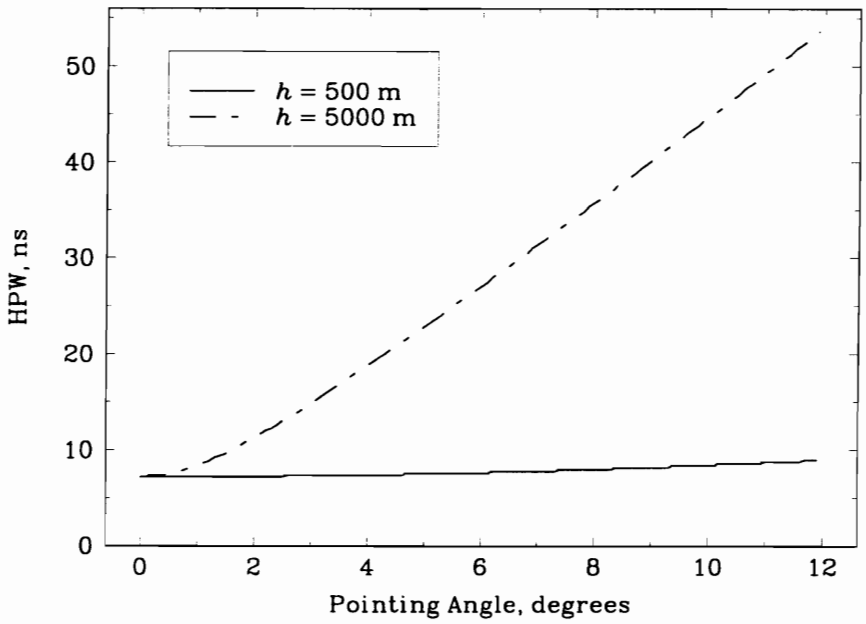

Figure 3.3. Comparison of the half-power width of the surface scattered waveforms at two altitudes for the MARA system.

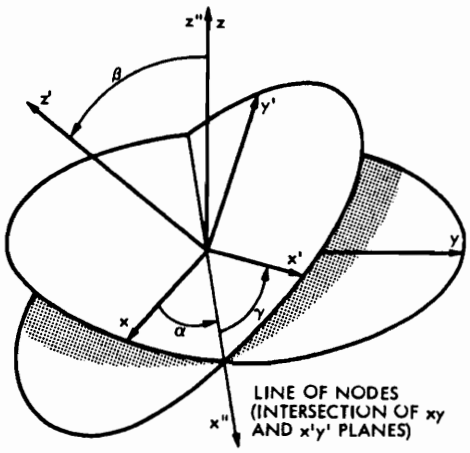

Figure 3.4. Definition of Eulerian angles. From [30].

coordinate systems is [30]

$$\vec{r}' = A\,\vec{r}, \tag{3-4}$$

where

$$A = \begin{bmatrix} \cos\alpha & -\sin\alpha\cos\beta & \sin\alpha\sin\beta \\ \sin\alpha & \cos\alpha\cos\beta & -\cos\alpha\sin\beta \\ 0 & -\sin\beta & \cos\beta \end{bmatrix},$$

and

$$\vec{r}' = \begin{bmatrix} x' \\ y' \\ z' \end{bmatrix} = \begin{bmatrix} \tan\xi_o \cos\phi_o \\ 1 \\ \tan\xi_o \sin\phi_o \end{bmatrix} \quad \text{and} \quad \vec{r} = \begin{bmatrix} x \\ y \\ z \end{bmatrix} = \begin{bmatrix} \tan\xi_a \cos\phi a \\ 1 \\ \tan\xi_a \sin\phi a \end{bmatrix},$$

and γ has been set to zero as discussed previously. The angles ξ and ϕ denote the elevation and azimuth angles, respectively, of the antenna. The o and a subscripts refer to original (before including pitch and roll) and actual (after including pitch and roll) angles, respectively. The elevation angle ξ is the same as the pointing angle used in the waveform models of the previous chapter. The azimuth angle ϕ indicates which direction the off-nadir antennas are pointing. For example, if the forward-directed antenna is used as a reference, its azimuth angle is zero and the remaining off-nadir beams (in counter-clockwise order) are: starboard, 90°; aft, 180°; portside, 270°. The nadir beam is not really pointing at a specific azimuth direction, so its original azimuth angle is set to zero.

To solve for the actual angles contained within $\vec{r}$, the matrix inverse A^{-1} must be found. From [30], $A^{-1} = A^T$ so the inversion is trivial. Thus, $\vec{r}$ can be found by computing $A^{-1}\,\vec{r}'$ and the actual pointing angles calculated from the elements of $\vec{r}$;

$$\phi_a = \tan^{-1}\left[\frac{z}{x}\right], \qquad \xi_a = \tan^{-1}\left[\frac{x}{y\cos\phi_a}\right]. \tag{3-5}$$

This procedure provides a more accurate value of antenna pointing angle to be used to compute the waveform models for analysis of the altimeter data. However, the azimuth angle is not as important as the pointing angle in these models; it's importance is its use in finding the actual elevation (pointing) angle in the latter of equations (3-5).

As an example, assume that the port antenna is directed toward $\xi_o = 12°$, $\phi_o = 270°$. If the aircraft experiences a 2° pitch and 4° roll, the resulting actual pointing angles are

$\xi_a = 16.1°$, $\phi_a = 277.1°$. Note that a positive roll is defined by a clockwise rotation of the aircraft (as viewed from behind), so that the left wing rises as the right wing drops. A positive pitch means that the nose of the aircraft has risen.

Another thing that must be accounted for in the angle computations is the use of mounting biases. A mounting bias is the angular difference between the nadir beam's boresight axis and the aircraft yaw- (y-) axis. These biases are used because during normal flight, the aircraft usually flies with a pitch of roughly 2° to stay airborne. If the altimeter system is not adjusted to account for this, the result is a nadir beam that doesn't nominally point toward nadir.

For the MARA system, the mounting biases are 1.85° in pitch and 0° in roll. To incorporate these biases into the above calculation of actual pointing angles, they are simply added to the pitch and roll values obtained from the aircraft INS system. The result is a more accurate value of pointing angles for model computations. This accurate pointing knowledge is especially important for the MARA system because of its extremely narrow beamwidth.

3.1.3 Waveform Retracking

The MARA system records 48 contiguous samples of each return waveform for each beam. These waveforms are centered in the 48-bin window by an on-board tracker, but from pulse to pulse, these waveforms can move left or right in the window because the *track point* depends on a threshold level on the waveform. Since the waveforms experience random fading, the track point does not necessarily occur at the same time for each waveform. Thus, the waveforms need to be *retracked*, so that when they are averaged to reduce the noise and the fading effects a more accurate representation of the waveform is obtained.

Several retracking algorithms exist, and three of these are discussed by Ferraro [15]. One of these methods, called the offset center of gravity (OCOG) tracker and developed by the Mullard Space Science Laboratory, basically computes a centroid location of each waveform, then lines up these centroid locations before averaging. It is said to be the most robust, as it can be successfully applied to a wide range of waveform shapes, such as those returned from sea ice, glacial ice, ocean returns and others that exhibit low signal-to-noise ratios [15].

While the OCOG retracking method is said to be best for a wide range of waveform shapes [15], its use to-date has been for pulsewidth limited returns such as those common to the Advanced Aircraft Flight Experiment (AAFE) altimeter and other satellite-based systems. For the low altitudes used in conjunction with the MARA system, the return waveforms have a very short duration because of the much smaller footprint on the surface. A brief study was performed which demonstrated that the OCOG tracker is less than effective for these MARA waveforms, when compared to others methods.

The *peak-alignment* (PA) method used to perform the retracking for the MARA waveforms in this work is much simpler than the OCOG method. The peak value of each waveform is identified and its corresponding time-location is noted. The retracking algorithm then simply shifts the individual waveforms to line up all the peak values at the same time location. However, for a given average of, say 100 waveforms, not necessarily all of the peak locations should be aligned to the same time location. The reason is that aligning all the individual waveforms to one location may remove the large-scale surface height variability from the averaged waveform.

An example surface in Figure 3.5 has both small- and large-scale height variability. Suppose that an average of 100 individual waveforms covers the surface between points a and d as the aircraft flies from left to right. Each return waveform will have a slightly different threshold-determined range value that will follow the overall contour of the surface. If the individual waveforms are aligned to a single time location for this entire length, the large-scale variation will be lost because each waveform will be shifted to some value set by the first waveform. Now suppose the waveforms obtained over a smaller region, say between a and b, are aligned to one time location, then the next segment between b and c are aligned to a new time location that may be different from the first group and so on for the whole extent of a to d. These segment-realigned individual waveforms are averaged together to obtain a (hopefully) truer representation for the area defined between a and d. For the MARA data examined in this work, individual waveforms are peak-aligned five at a time to obtain an averaged waveform.

3.1.4 Waveform Splining

Because of the short duration of the recorded waveforms, the sample spacing of 2.226 ns used for the MARA system is actually rather coarse. For example a specific nadir

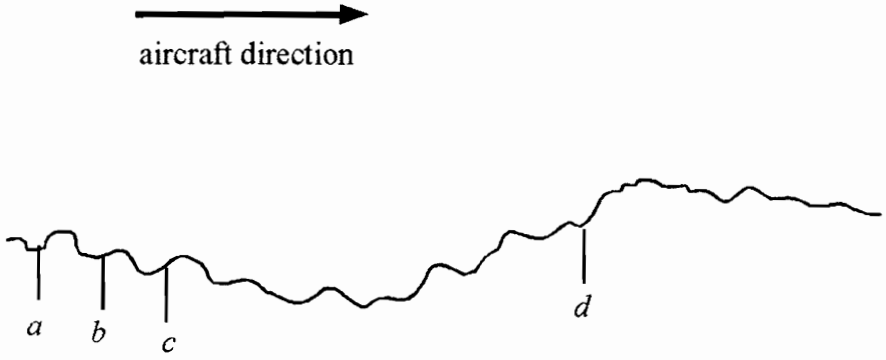

Figure 3.5. Example of large- and small scale surface height variability to illustrate the effect on retracking.

return usually has only 8-10 samples greater than 1/10 the peak value. When comparing the averaged waveforms to the modeled waveforms, the modeled waveforms are much smoother as their sample spacing can be set at-will in the modeling algorithm. To provide a better comparison of the averaged and modeled waveforms, the averaged waveforms are *splined.* A cubic spline routine is used to "fill-in" the waveforms between the averaged points.

To illustrate this, consider the average waveform shown in Figure 3.6. The data points denoted by small $\times$'s represent the actual averaged data. The solid line represents the splined waveform that has a sampling increment of 0.1 ns, resulting in a smoother waveform. An important feature of this method is realized be examining the peak region of this example data. Note that the closest averaged data point to the peak ($\sim$ 37 ns) is not located precisely at the peak of the splined waveform. In this example the sampling of the actual altimeter data (on average) did not sample the peak of the returns exactly. If the data point at $\sim$ 37 ns were taken to be the peak value of the waveform, a slightly different waveform shape would result. The different waveform shape would then adversely affect the value of σ_h that would be chosen for the model to provide the best fit to the data. It is very important to have an accurate as possible representation of the averaged data if robust estimates of fit parameters are to be obtained. This is particularly true in the case of combined surface and volume scattered waveforms, where more than one fit parameter will be affected by inaccurate waveform shapes.

3.2 Examination of Data from Over Water

The MARA system was originally designed to be used to study ocean surfaces, so examination of data from over-water experiments provides a logical method for testing the system's data recording capabilities. On several occasions during the 1991 Greenland mission, the aircraft flew out over the Western waters of Greenland, particularly over Jakobshaven Bay and Sondestrom Fjord. On September 20, 1991, shortly before landing at the NASA base at Sondestrom, the aircraft flew out over the fjord and the MARA system recorded data for a period of time before the pilot turned and headed back toward the mainland. These data provide a check to ensure that the system was operating correctly, since radar altimeter returns from water are better understood than those from the ice sheets.

3.2.1 Waveform Fit Example

Figure 3.6 shows a sample of the averaged MARA waveform data for the nadir beam. 1000 raw waveforms are averaged, resulting from approximately 10 seconds of data. Since the aircraft ground speed was about 100 m/s and the system prf is 100 Hz, the length of the illuminated area was about 1 km. The altitude during this span of data was nearly 500 meters, so a "single-pulse" illuminated area had a diameter of about 10 meters. The width of this 1 km swath is then 10 meters. It is assumed that this distance is significantly larger than the surface height correlation length.

Overlaid with the averaged waveform is a model surface waveform. This surface waveform uses a Gaussian point target response that is 6.5 ns wide to approximate the transmitted pulse of the MARA system. For this waveform, the best fit is realized when the rms surface roughness is set to 20 cm in the model. Since the water surface is very smooth on the fjords that surround Greenland, this value seems a bit high. Examination of video footage taken during these flights over the fjord revealed a near-glassy water surface, which should translate into a very small surface roughness. Since there was no ground-truth data (such as from buoys or in-situ measurements) to compare with, the actual surface roughness can only be speculated. For a surface this smooth, roughness values of about 5-10 cm could be expected.

3.2.2 Water Data Waveform Statistics

Since the roughness estimate from the smooth-water data seems a bit off, another useful check for the MARA system is to examine the statistics of the return waveforms. The MARA receivers' detectors are square-law devices*, so a random, narrow-band Gaussian input signal to these devices will result in an output signal power that is exponentially-distributed after low-pass filtering [12]. A notable property of the exponential pdf is that its mean is equal to its standard deviation [24]. The average waveform data points in Figure 3.6 are the mean values of the received power waveform. Thus, the standard deviation curve should closely follow the average waveform, since the mean and standard deviation values at each point in time should be equal.

Figure 3.7 shows an example of the waveform statistics that correspond to the average

*In fact, the MARA detector is known to not be exactly square law (see §3.1.1). This assumption thus contributes some error to the statistical analysis.

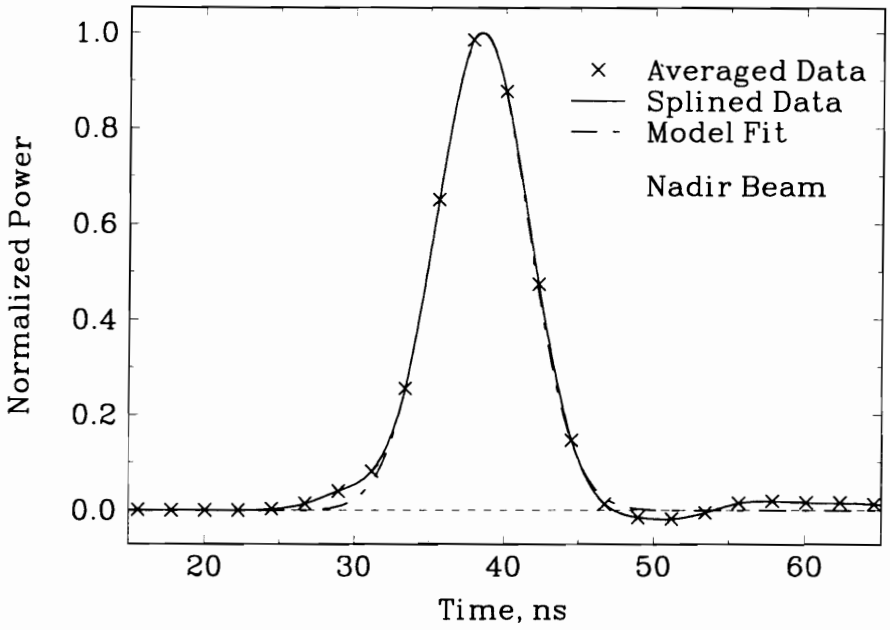

Figure 3.6. Example of averaged over-water data for the MARA altimeter.

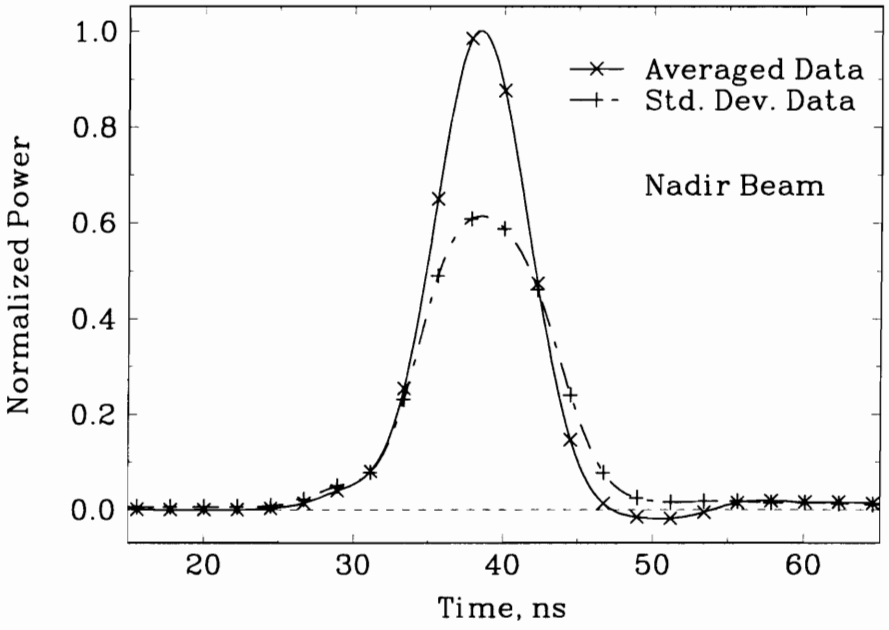

Figure 3.7. Mean and standard deviation waveform statistics for the averaged waveform in Figure 3.6.

waveform shown in Figure 3.6. Notice that the average (mean) and standard deviation curves do not coincide as expected. However, these curves are not completely dissimilar, as the standard deviation curve has roughly the same shape as the mean waveform. This type of behavior is common to all the water data that was examined from this experiment.

Examination of the histograms of the recorded power values for each value of time and for each individual return waveform should provide a basic idea of what the power pdf looks like. Figure 3.8(a-g) shows a few sample histograms of the waveform data in Figures 3.6 and 3.7. For each, the time location on the waveform is noted, as they correspond to the discrete times during the (a) leading edge through (g) trailing edge of the average return waveform shown in Figure 3.7. The histograms should resemble the pdf of the random process [24] that is the return power waveform at the particular time in the waveform. Only those histograms for the time points with low mean values, that is Figure 3.8(a), (b), (f) and (g), resemble exponential distributions. Those with higher mean values, Figure 3.8(c) through (e), actually resemble something more like Rayleigh distributions.

Two known problems may possibly be affecting the waveform statistics. First, the MARA detectors are known to be not exactly square-law type, as noted in § 3.1.1. Since the nonlinearity is stronger for higher power levels, it might explain why the histograms are non-exponential only for the higher amplitude (peak) regions of the average return waveforms. This deviation from the square-law assumption would make the output signal pdf somewhat different from an exponential, but there is no way to know exactly what it is without a closer examination of the receiver subsystem. Second, the average AGC level for the example data in Figures 3.6 and 3.7 was about 157, which is very near the caution limit of 160 discussed in § 3.1.1. This value is so high because during the flights over the fjord, the nadir signal was very strong while the off-nadir signals were consequently quite weak because of the almost specular surface. The corresponding off-nadir AGC values ranged from 86 to 143. In order to keep the off-nadir signal strength high enough to allow the receivers to maintain a lock, the output power had to be kept high, which unfortunately drove the nadir signal too strong. This unanticipated problem was common to much of the water data, as well as some areas of ice sheet data.

To see if the high AGC problem is a major contributor to the ill-behaved waveform statistics, off-nadir over-water data was also examined. These data also were not exponentially distributed, so the AGC level may not be as influential in this problem as

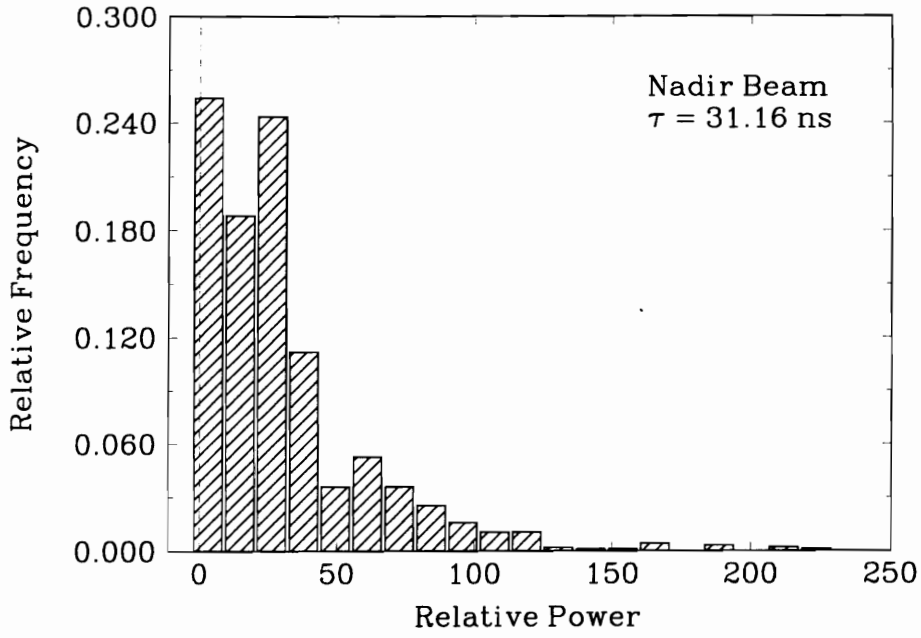

(a)

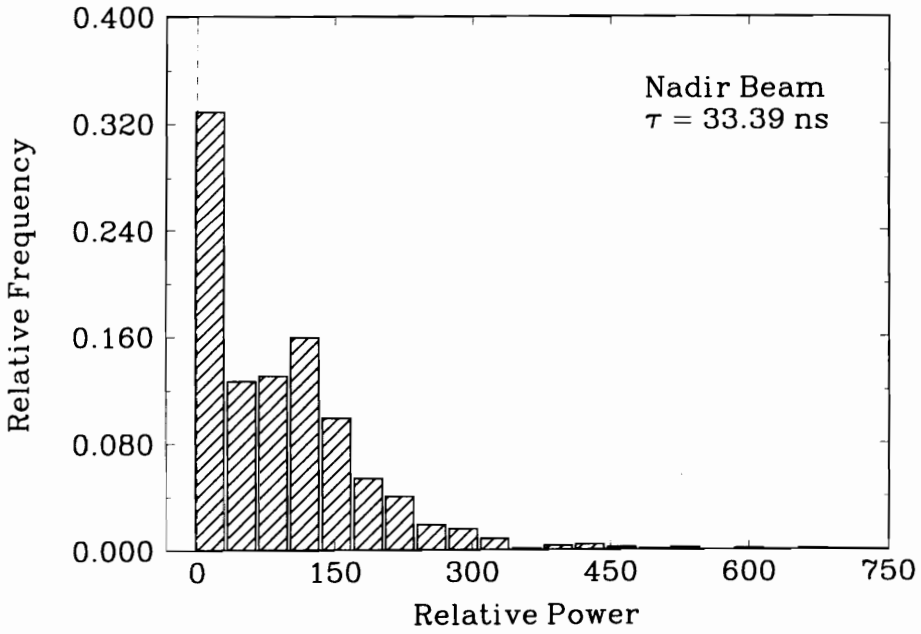

(b)

Figure 3.8. Sample histograms of the waveform data shown in Figure 3.7.

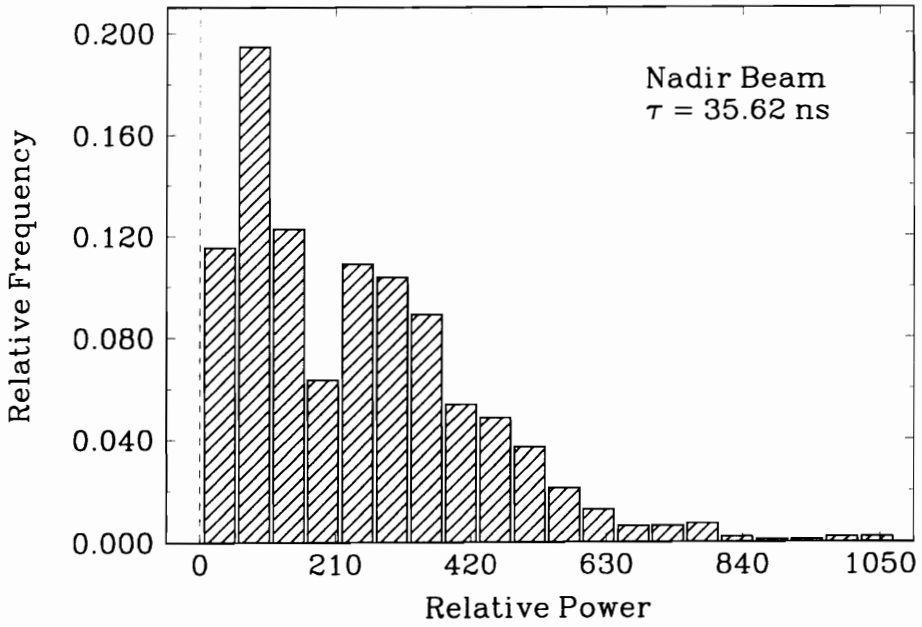

(c)

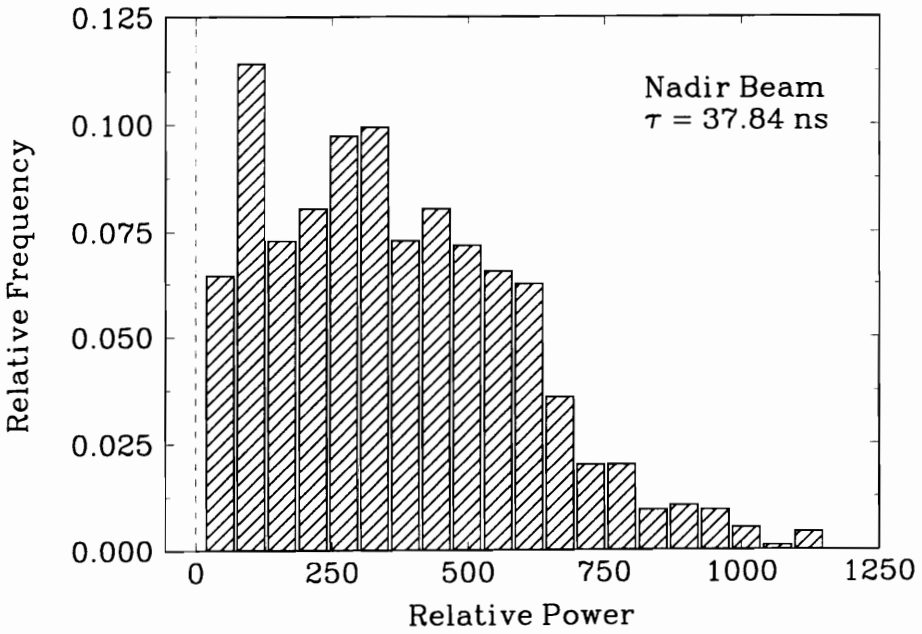

(d)

Figure 3.8. (Cont.) Sample histograms of the waveform data shown in Figure 3.7.

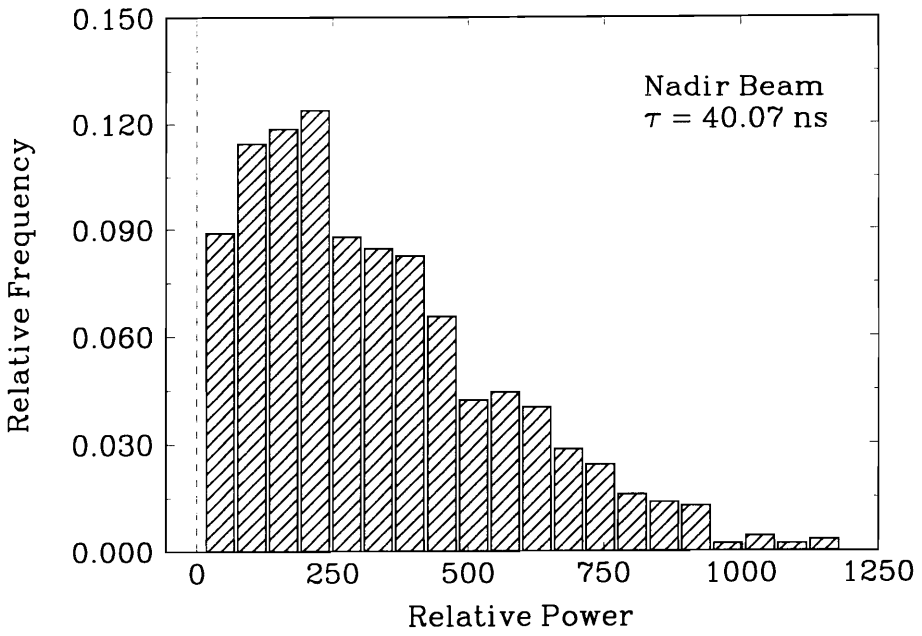

(e)

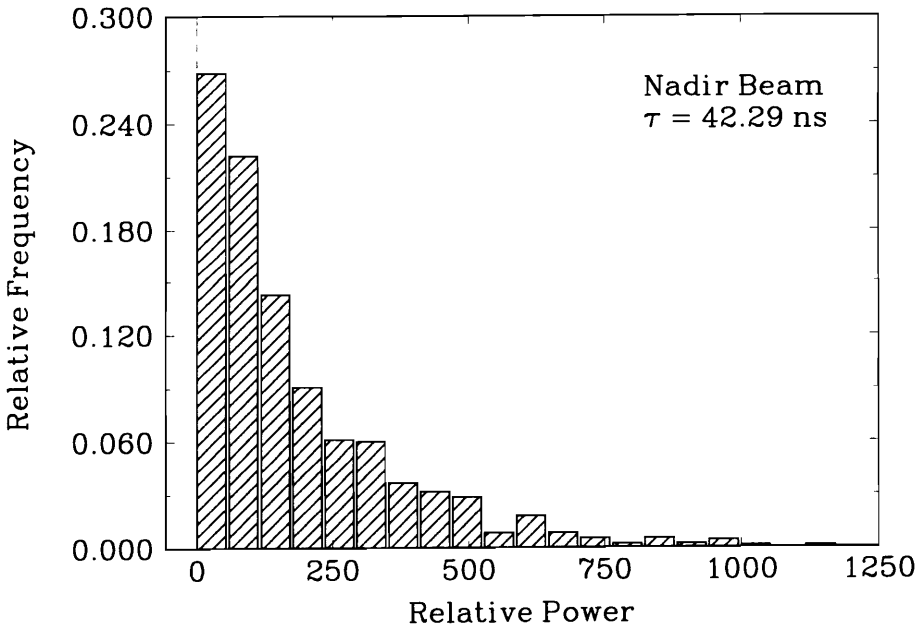

(f)

Figure 3.8. (Cont.) Sample histograms of the waveform data shown in Figure 3.7.

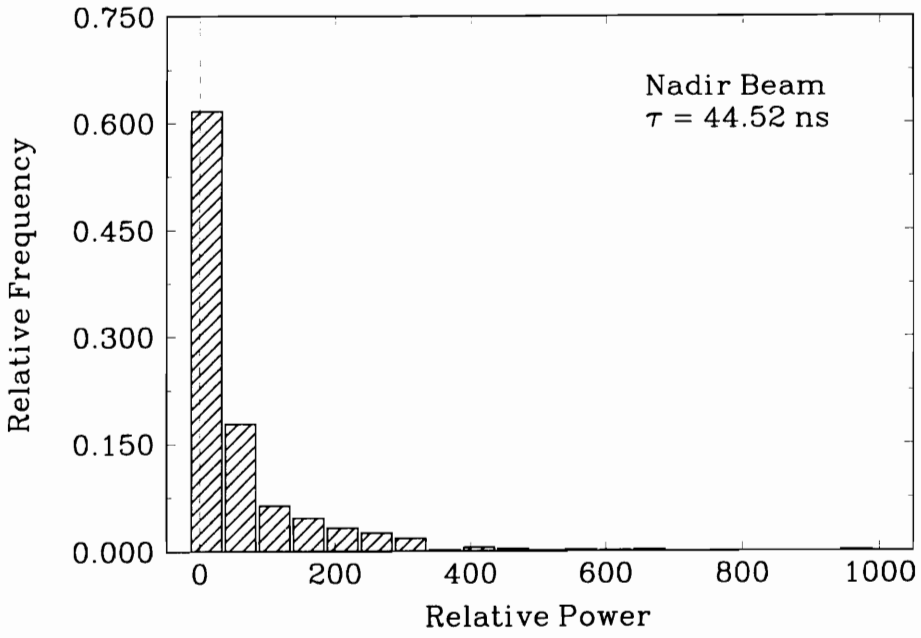

(g)

Figure 3.8. (Cont.) Sample histograms of the waveform data shown in Figure 3.7.

the nonlinear detectors. Again, this cannot be confirmed, as only a more thorough system-level test can determine the complete effects of the nonlinear detectors.

3.3 Data Correction Attempts

A number of approaches were investigated to see if the data could be corrected beyond the simple cubic equation used in §3.1.1. This involved relating the measurements of the recorded MARA data and its moments to the true post-detection waveform and its moments for rather simple effects. The most reasonable of these is a weak nonlinear effect, because the detectors are known to be nonlinear.

3.3.1 Weak Non-Linearity Correction

If $X_n(\tau)$ denotes the n^{th} true post-detection waveform (which is exponentially distributed) and $Y_n(\tau)$ denotes the n^{th} recorded MARA (corrupted) waveform, then the weak nonlinear effect can be described by

$$Y_n(\tau) = X_n(\tau) + \beta X_n^2(\tau) \tag{3-6}$$

if $|\beta| \ll 1$. To find a correction formula based on the weak nonlinear effect, equation (3-6) must be solved for $X_n(\tau)$ in terms of the moments of $Y_n(\tau)$. The first and second (central) moments are what have been shown in Figure 3.7. If the time dependence (τ) is suppressed from here on, the first moment (denoted $\langle \cdot \rangle$) of Y_n, is

$$\begin{aligned} \langle Y_n \rangle &= \langle X_n \rangle + \beta \langle X_n^2 \rangle \\ &= \langle X_n \rangle + \beta \left[[\![X_n]\!]^2 + \langle X_n \rangle^2 \right] \\ &= \langle X_n \rangle + 2\beta \langle X_n \rangle^2. \end{aligned} \tag{3-7}$$

The result in (3-7) makes use of the fact that the mean and standard deviation (denoted $[\![\cdot]\!]$) of the exponentially distributed X_n are equal, i.e. $\langle X_n \rangle = [\![X_n]\!]$. Using (3-7), the standard deviation of Y_n is

$$
\begin{aligned}
[\![Y_n]\!]^2 &= \langle Y_n^2 \rangle - \langle Y_n \rangle^2 \\
&= \left\langle \left[X_n + \beta X_n^2 \right]^2 \right\rangle - \left\langle \left[X_n + \beta X_n^2 \right] \right\rangle^2 \\
&= \langle X_n \rangle^2 + 2\beta \langle X_n^3 \rangle + \beta^2 \langle X_n^4 \rangle - \langle X_n^2 \rangle - 2\beta \langle X_n \rangle^3 - \beta^2 \langle X_n \rangle^4 \\
&= [\![X_n]\!]^2 + 2\beta \left[\langle X_n^3 \rangle - \langle X_n \rangle^3 \right] + \beta^2 \left[\langle X_n^4 \rangle - \langle X_n \rangle^4 \right] \\
&= \langle X_n \rangle^2 \left[1 + 2\beta \left(\frac{\langle X_n^3 \rangle - \langle X_n \rangle^3}{\langle X_n \rangle^2} \right) + \beta^2 \left(\frac{\langle X_n^4 \rangle - \langle X_n \rangle^4}{\langle X_n \rangle^2} \right) \right],
\end{aligned}
\tag{3-8}
$$

where once again $\langle X_n \rangle = [\![X_n]\!]$ has been used. At this point, if $|\beta| \ll 1$ (which implies the *weak* nonlinearity) the β^2 term in equation (3-8) can be neglected. To simplify (3-8) further, $\langle X_n^3 \rangle$ must be determined. Use of basic principles of probability theory provides $\langle X_n^3 \rangle = 6 \langle X_n \rangle^3$. By using this and taking the square root of (3-8), $[\![Y_n]\!]$ reduces to

$$
[\![Y_n]\!] \approx \langle X_n \rangle [1 + 10\beta \langle X_n \rangle]^{1/2}. \tag{3-9}
$$

Now if $|10\beta \langle X_n \rangle| \ll 1$, the binomial approximation can be applied to (3-9) to obtain

$$
[\![Y_n]\!] \approx \langle X_n \rangle [1 + 5\beta \langle X_n \rangle]. \tag{3-10}
$$

Equations (3-6) and (3-10) can now be solved simultaneously for $\langle X_n \rangle$ and β, which yields

$$
\langle X_n \rangle = \frac{5}{3} \langle Y_n \rangle - \frac{2}{3} [\![Y_n]\!] \tag{3-11}
$$

and

$$
\beta = \frac{1}{3} \frac{[\![Y_n]\!] - \langle Y_n \rangle}{\left[\frac{2}{3} [\![Y_n]\!] - \frac{5}{3} \langle Y_n \rangle \right]^2}. \tag{3-12}
$$

Equation (3-11) can be used to obtain the corrected mean waveform from the existing mean and standard deviation waveforms. However, this does not prove that the corrected mean and standard deviation waveforms are equal. To do this, the raw waveform data must be corrected *before* the waveform averaging takes place. The raw data is corrected by solving (3-6) for X_n

$$
X_n = \frac{-1 \pm \sqrt{1 + 4\beta Y_n}}{2\beta}. \tag{3-13}
$$

Equation (3-13) is used with the β value calculated from the mean and standard deviation

values for the corrupted data using (3-12) to provide the corrected data. These data are then averaged and hopefully the waveform statistics will be corrected, i.e. exponential. An important note is that the assumptions of $|\beta| \ll 1$ and $|10\beta\langle X_n\rangle| \ll 1$ must be satisfied for this method to work, so the value of β must be monitored as the data averaging is performed. Also, since the waveform data must be positive, the proper sign must be chosen in (3-13), which will depend on the sign of β.

This "correction method" was applied to the data shown in Figure 3.7, resulting in no significant difference in the shapes or amplitudes of the mean and standard deviation waveforms. In fact, comparison of this correction technique with that discussed in §3.1.1 revealed that this technique actually made the difference between the mean and standard deviation curves slightly worse. In Figure 3.7, the ratio of the mean to standard deviation values near the peak region (at $\sim$ 37 ns, where the difference is greatest) is 1.6. For the technique described above, the similarly defined ratio is 1.8, an adverse relative difference of 12%. A possible explanation for this is that the second condition on β (which allowed the binomial approximation to be used) was in fact often violated when the correction method was applied to this example.

3.3.2 Modified Weak Non-Linearity Correction

The weak non-linearity correction discussed in the previous section requires that two conditions be met, namely $|\beta| \ll 1$ and $|10\beta\langle X_n\rangle| \ll 1$. Unfortunately the latter of the two conditions is frequently violated, as demonstrated in the previous section. This usually occurs for the averaged data in the peak region of the waveforms, exactly where the correction is needed most because the nonlinear effects are strongest there.

This latter condition on β enabled the binomial approximation to be used to simplify equation (3-9); this in turn allowed the correction equations in (3-12) and (3-13) to be easily found. Since this condition is often violated, a modified version of the weak non-linearity correction method must be developed. First, equations (3-7) and (3-9) are solved simultaneously for β in terms of $\langle Y_n\rangle$ and $[\![Y_n]\!]$. Equation (3-7) is multiplied by $\langle X_n\rangle$ and equation (3-9) is squared to yield

$$\begin{aligned} [\![Y_n]\!]^2 &= \langle X_n\rangle^2[1 + 10\beta\langle X_n\rangle] \\ \langle X_n\rangle\langle Y_n\rangle &= \langle X_n\rangle^2[1 + 2\beta\langle X_n\rangle]^2. \end{aligned} \tag{3-14}$$

The difference of the equations in (3-14) is taken and solved for β to obtain

$$\beta = \frac{[\![Y_n]\!]^2 - \langle X_n \rangle \langle Y_n \rangle}{8\langle X_n \rangle^3}. \tag{3-15}$$

The form for β in (3-15) still depends on the unknown $\langle X_n \rangle$. This is found by taking the difference of the first of equations (3-14) and five (5) times the second to obtain

$$4\langle X_n \rangle^2 - 5\langle X_n \rangle \langle Y_n \rangle + [\![Y_n]\!]^2 = 0. \tag{3-16}$$

Equation (3-16) is quadratic in $\langle X_n \rangle$ and its solution is

$$\langle X_n \rangle = \frac{5}{8}\langle Y_n \rangle \pm \frac{1}{2}\sqrt{\frac{25}{16}\langle Y_n \rangle^2 - [\![Y_n]\!]^2}. \tag{3-17}$$

Now β is found by (3-15), making use of (3-17). The data are then corrected by applying (3-6).

This modified technique was again applied to the waveform data shown in Figure 3.7. Once again the data was not corrected, but was made worse. The ratio of the mean and standard deviation values at $\sim$ 37 ns for this method was 1.9, while the original ratio for the technique for §3.1.1 was 1.6. The relative change was 19%, which is even worse than the previous correction attempt.

3.3.3 Other Correction Attempts

The previous correction attempts were based on knowing how the MARA data should behave. These methods took the corrupted data and used knowledge of its moments to transform it into data with supposedly true (uncorrupted) moments. The problem was that some of the necessary basic assumptions were violated along the way.

Other correction methods were tried as well. These were not based on knowing how the data should behave, but on realizing how the data was behaving. Since the power pdf shape was non-exponential in the peak region of the averaged waveforms, other pdf types beside the exponential were tried. In particular, the Gamma, Rayleigh and the "convolved exponential" pdfs were investigated to see if they could describe the data, not worrying about what it would mean if one of these did work. The convolved exponential pdf arose from convolving two exponential functions and adjusting the amplitude to make the resulting function fit the defining rules for pdfs. It can result from the addition of two uncorrelated, exponentially distributed random processes. Only very preliminary

work was necessary to see that these approaches were also not effective in explaining the deviation from exponential statistics.

After all of these attempts, all that can be said is that the MARA data is usually affected by factors that cannot be accounted for by these simple attempts. The data can still be used for analysis of the ice sheets as in the next chapter, but it should be kept in mind that the results obtained in any analysis may be in error to some unknown degree.

Chapter 4
Parameter Estimation

The other major goal of this research is to devise a method by which the combined waveform scattering model can be used to determine the parameters that describe the scattering medium and its interface with free space. These parameters are the surface roughness σ_h, effective volume extinction coefficient k_e and the volume-to-surface peak amplitude ratio η. In the combined model, the surface roughness is only present in the surface portion, and is a parameter only in the height pdf in that model. The extinction coefficient is found only in the volume scattered impulse response and the combination ratio is used in the summation of the surface and volume models. This *separable* nature of the model parameters will permit the use of a "brute-force" method to find the parameters that best fit the altimeter data. Other minimization algorithms are discussed as possible methods to perform this fitting process, but their implementation is deferred to future research.

For this application, the "best fit" is defined as the combined waveform and parameters which yield a minimum value of the squared difference between specific discrete points on the model and data. As a test case, the fitting algorithm will be used to find a best fit of a model waveform to itself. This is done by using the model to generate a sample waveform and then use the estimation algorithm to find the waveform parameters. Finally, examples of parameter estimation for actual altimeter data will be given to demonstrate the effectiveness of this method.

4.1 Estimation Method

Before selecting a suitable optimization method, the function that is to be optimized must be defined. In this case, the desired optimization is a minimization of a function that is the cumulative square of the difference between the averaged altimeter data and the combined scattered waveform model. Mathematically, this function is

$$F(\sigma_h, k_e, \eta) = \frac{1}{N}\sum_{i=1}^{N}|D(\tau_i) - C(\tau_i; \sigma_h, k_e, \eta)|^2. \tag{4-1}$$

In (4-1), $D(\tau_i)$ represents N discrete time values of the averaged waveform data that exceed some minimum threshold value. A threshold is used to avoid having the model forced to fit the data in regions which are inherently noisy. $C(\tau_i; \sigma_h, k_e, \eta)$ is a discrete time representation of the combined waveform model given in (2-32). The $1/N$ factor provides a normalization in the sense that the values of F can be compared independently of how many data points are used to compute (4-1). This is most important when comparing F values for different waveform shapes, such as those for nadir and off-nadir waveforms which can have a different number of sample points that exceed some threshold value.

The two functions $D(\tau_i)$ and $C(\tau_i; \sigma_h, k_e, \eta)$ must also be aligned before (4-1) can be computed. This must be done because the altimeter records the waveform samples within a range window that is not necessarily time-referenced to the same time as the waveform model. The range window is usually referenced to a threshold value on the waveform because of the use of a threshold tracker in the MARA system. In general the relationship between the threshold value and absolute time is not directly known, especially for off-nadir returns. The alignment is done by simply searching through both the model and the data to find the time of their respective peaks. The waveforms are then aligned by the time of their peaks and the function $F(\sigma_h, k_e, \eta)$ is computed. The waveform data comprise discrete points of a continuous curve, so quite often the peak value of the data does not coincide with the true peak of the waveform it represents. To circumvent this difficulty, the data is splined to find an estimated peak location and that value is used to align the model to the data. The function evaluation in (4-1) is done only with the original N data points and the corresponding values of the aligned model waveform.

It is worth noting here that the waveform model $C(\tau_i; \sigma_h, k_e, \eta)$ is actually also dependent on pointing angle ξ and altitude h. Figure 3.2 showed that the width of the modeled returns can vary dramatically, particularly for larger altitudes. Since the MARA data that will be examined was obtained from relatively low altitudes ($\sim$ 500 meters), this sensitivity is not as critical. The MARA system records the aircraft INS attitude (pitch and roll) with every return waveform. These attitude angles are quite accurate [38]

and are used along with the nominal pointing angles to determine a fairly accurate estimate of the actual antenna pointing angle for each return waveform, as discussed in §3.1.2. Thus, the parameter estimation does not have to account for pointing angle sensitivity in the waveform model. The MARA system also records a threshold-detected range value with each waveform, which can be converted to altitude using the estimated pointing angle These values of pointing angle and altitude can then be supplied to the estimation program to generate modeled waveforms. If data is examined from higher altitudes for a system with less accurate pointing knowledge, these simplifications may not be valid.

Since the combined model is a function of three unknown parameters, a three dimensional optimization algorithm must be employed. As each of the three are varied the value of F will change; the minimum value of F is interpreted as the best fit situation and the corresponding parameters are recorded as the best-fit values. Several methods can be used to perform this optimization, including many minimization routines that are available in software libraries. For this work, a more basic approach was used because of the special separable nature of the model. The commercially-available techniques are discussed first, then an outline of the optimization method that was used in this work is given.

4.1.1 Evaluation of Available Minimization Methods

Several optimization methods are candidates for the minimization of (4-1). An incomplete list of such multidimensional methods includes downhill simplex, conjugate-gradient, direction set (Powell's) and variable metric methods [29]. Each method has its particular advantages, but only the first two of these will be discussed. A brief summary of the advantages and disadvantages of these methods follow, but more detailed information is provided in the literature [29].

The downhill simplex method is the most straightforward of those listed above. It is a self-contained algorithm, in that it does not rely on one-dimensional minimization techniques as do the other methods. The other strong advantage is that it does not require derivative information. At first, this latter feature may not seem important, but consider the difficulty involved with computing a derivative of (4-1) with respect to any of the three unknown parameters. σ_h is contained within the surface model, k_e in the volume model and both involve a convolution integral. Clearly a closed expression for a

derivative, let alone a gradient, of (4-1) is extremely difficult to obtain. Thus, if a minimization method that does not require derivative calculations can be developed, it should be given preference.

The most imposing disadvantage of the downhill simplex method is that it is rather inefficient in terms of the number of function evaluations required, and this is a rather serious concern for this application. The computation of the function in (4-1) is not that difficult; however, the calculation of the model waveform $C(\tau)$ can be very time consuming if many computations are needed. This is because of the double integration needed for the volume scattering impulse response (see equation (2.17)) and the dependence of the upper limit of one of these integrals on time. While simplifications exist for the nadir and far-off-nadir pointing cases, there is the very real chance that these simplifications will not apply.

In contrast, the class of conjugate-gradient methods is quite efficient when derivative information is available. While these methods require evaluations of both the function and its gradient, the total number of evaluations is often much less than those for the more primitive downhill simplex method. The reason is that gradient information provides a best "direction" for the minimization routine to use to find the parameter values that minimize the function. Thus, fewer evaluations are needed to arrive at a best fit. Gradient information is not readily available in this work, as such expressions would be quite cumbersome. As an alternative way to provide the gradient information, a numerical gradient can be computed using either a central-, backward- or forward-difference technique in each of the three parameter directions. A disadvantage is that the number of function evaluations is increased with this approach, which may make the method less efficient than others and defeats the purpose for using conjugate-gradient methods.

A number of libraries exist that provide source code for all of these optimization techniques. Those found in Numerical Recipes [29] are particularly useful versions because they are supplemented with examples and discussions to demonstrate their use. The implementation of these methods is deferred to future work. For now, computational speed is not as important as accurately determining the parameters of the model. For this reason, a more basic approach is used to find the model parameters.

4.1.2 "Brute-Force" Minimization Algorithm

The minimization algorithm that was used in this research is a brute-force method. As the name implies, it is not an elegant algorithm, but it serves its purpose as an easy implementation that provides good results. Basically, this method computes all the surface and volume waveforms that it will need before actually combining them and comparing to the data. The reason that this method has promise is due to the fact that the fitting parameters (σ_h, k_e, η) are separable. Since the surface roughness is only present in the surface model, all the expected values of σ_h can be used to calculate a series of surface waveforms for a given pointing angle and radar altitude. Likewise, all the k_e values in the expected range are used to compute the volume models. With all of these waveforms stored in memory, they can each be used in the combined model using the entire range of expected η values to obtain $C(\tau)$. Thus, all combinations of the three parameters are used to compute $F(\sigma_h, k_e, \eta)$ and the best fit is the combination of parameters that yield the smallest value.

A concern about this method is the choice of the parameter value ranges (as well as the increments for each) that will be used to compare to the data. Testing on the model determined that the range of η can safely be limited to 0.1 to 10. Beyond this range the model waveforms are practically insensitive to η. The other two parameter ranges must be chosen carefully to ensure that the number of data waveforms that cannot be fit is minimized while keeping in mind that extending the range too far is rather costly in terms of memory storage and CPU time. As for the increment for the parameters, a similar balance between memory use / CPU time and desired estimate precision must be found.

A simple test case for this fit algorithm was developed to demonstrate its use and to see how well it performs. The waveform model is used to compute a simulated data waveform that is fed into the fit program as the function $D(\tau_i)$ in (4-1). If the parameters used to generate this simulated waveform fall within the range of values used by the algorithm, they will be found. If those values coincide with the values used by the estimation algorithm, the method will find those parameters exactly. Thus, if the simulated waveform is calculated using parameters that are within the parameter search ranges but do not fall exactly on values that will be checked by the minimization routine, the closest values will be found. While this test case may seem rather pointless, it does confirm that this algorithm operates correctly.

Confirmation of this is shown in Table 4.1. A model waveform was computed using the values of $\sigma_h = 0.23$ m, $k_e = 0.47$ Np/m and $\eta = 0.78$ for MARA having a zero (nominal) pointing angle and an altitude $h = 500$ meters. Each of the parameter search ranges are given in the table, along with their increments and resulting number of steps. The increments chosen for this test will not allow the algorithm to find these parameters exactly, but the estimated parameters that were found are very close to those used to simulate the data waveform. A finer increment is necessary if better precision is desired, but this costs added CPU time. The parameter range can be reduced, but then there is a risk of encountering waveform data that may have parameters outside the range of one of the parameter's search. A balance must then be struck between desired resolution for each parameter and the amount of memory and CPU time required to search all the parameter combinations.

4.2 Estimation Examples Using Altimeter Data

For these examples, the data are taken from an archive of the MARA 1991 Greenland experiment [38]. Specifically, the data are from the flight line shown in Figure 4.1, which was recorded on September 20, 1991. In the figures that accompany this example, the data run starts at the southern end of the flight line in the soaked and ablation region and goes northward into the dry snow region. During the summer of 1991, the different regions defined by Benson were thought to be approximately located along the flight line as follows: soaked and ablation from start to 69.5°N; percolation from 69.5 to 72°N; and dry snow from 72°N northward. For the south-to-north leg of this flight, there are over 630,000 individual return waveforms for each of the four beams (the aft beam did not operate during this experiment). In each case, an average of 100 individual altimeter returns were used, which results in well over 6300 averaged waveforms that could be used in the parameter estimation routine. These estimation examples were also performed using waveform averages of 500 and 1000 returns with no appreciable change in the results. In order to reduce the amount of time required to process the data for the whole flight line, only every tenth averaged waveform was selected as the function $D(\tau_i)$ in the fit program. The range of fit parameters, along with their increments and resulting number of steps are given in Table 4.2. These ranges and increments seemed to provide a good trade-off in resulting resolution and required computation time. Also, the speed of

Table 4.1 Summary of test results for the brute-force parameter estimation routine.

parameter	simulated value	range, increment, # steps				estimated values
		min.	max.	inc.*	# steps	
σ_h (m)	0.23	0.10	0.50	0.05	9	0.25
k_e (Np/m)	0.47	0.4	0.9	0.05	10	0.50
η	0.78	0.1	10.0	$10^{0.1}$	21	0.79

*Note: η increment is performed in log-space, with increment (in this example) of 0.1.

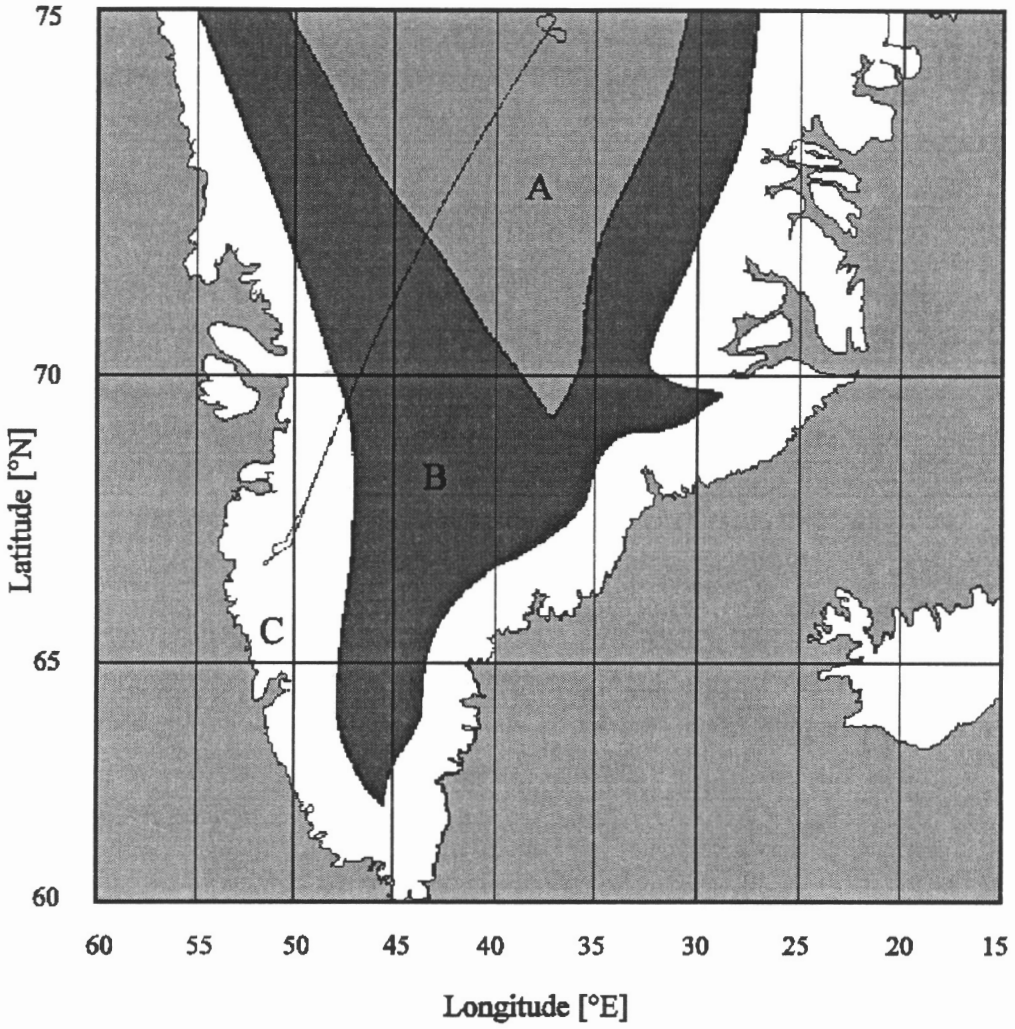

Figure 4.1 Map of Southern Greenland showing the flight line for the example data and the: (A) dry snow, (B) percolation, and (C) soaked and ablation regions.

Table 4.2. Parameter ranges, increments and resulting number of steps for analysis of the south-to-north leg of the September 20, 1991 MARA flight.

parameter	range, increment, # steps			
	min.	max.	inc.	# steps
σ_h (m)	0.02	0.60	0.02	30
k_e (Np/m)	0.10	2.00	0.05	39
η	0.1	10.0	$10^{0.1}$	21

light in snow, c_s is set to 0.24 m/ns, a value similar to that used by Davis [13], even though he was evaluating Ku-band data and these data are Ka-band. The error in using this value for the MARA data should be negligible because the dielectric constant does not change very much between the two frequencies, especially in dry snow [37] where volume scattering is most prevalent.

Figure 4.2 shows the results of the estimation program for the nadir beam data. All three parameters are plotted together as a function of latitude. Note that the right ordinate is used for the value of η, which is plotted logarithmically. The value of $\log \eta = 0$ (or $\eta = 1$) corresponds to equal surface and volume scattering contributions. The left ordinate gives the values for σ_h and k_e with units of meters and Nepers/meter, respectively. 636 data points are shown in Figure 4.2 for each parameter. The noisy nature of these results make it difficult to determine the general behavior that each parameter follows. To obtain a more representative value for the parameters, the largest possible number of values should be somehow averaged to effectively smooth out the data. A filtering process can thus be used to smooth out the data and provide a better estimate of a trend for each of the parameters.

The easiest filter to implement is the *simple averaging filter* [18], also known as a sliding average filter. It is defined by

$$y(n) = \frac{1}{M+1}\sum_{m=0}^{M} x(n-m). \tag{4-2}$$

Equation (4-2) states that the output value of some sequence of numbers, given by $y(n)$, is the average of the current and previous M values ($M+1$ total) of $x(n)$. This filter can be applied to the sequence of parameter values shown in Figure 4.2 to give a smoother representation of each. This will help identify the basic trends, if any, that the parameters exhibit as a function of latitude.

The sliding average filter is applied with a slight modification. Rather than average over the past $M+1$ values of a given sequence, the average will be centered around a given data point. In other words, the current, previous $M/2$ and following $M/2$ values are averaged to obtain a given data point. In mathematical terms, the lower limit on the summation in (4-2) becomes $-M/2$ and the upper limit becomes $M/2$. In signal processing this makes the filter *non-causal*, which simply means that a given value in an output sequence depends on information that has not yet happened in the input sequence.

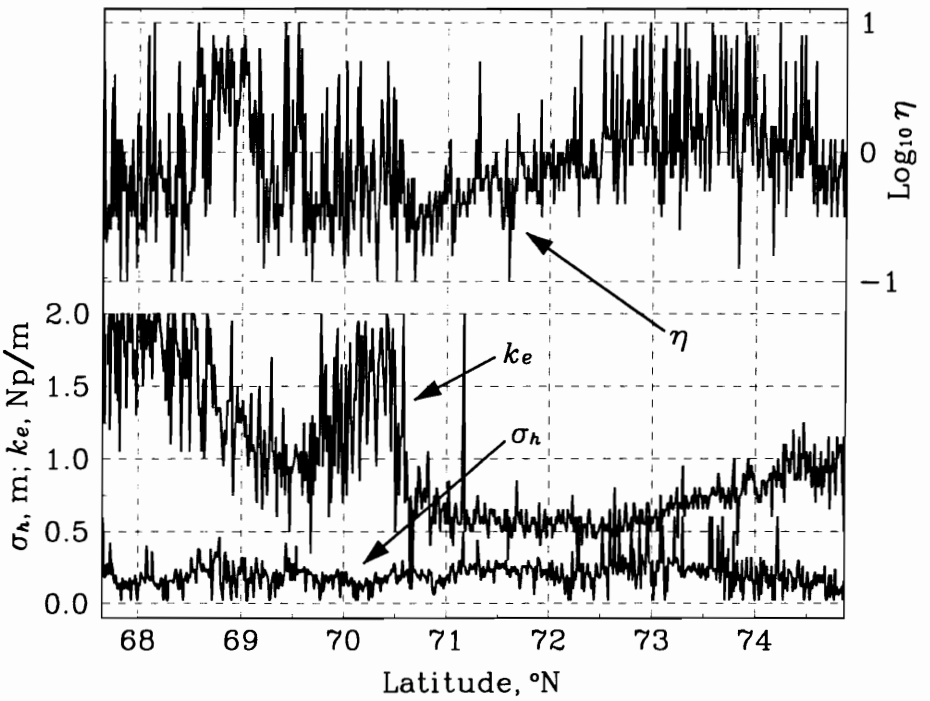

Figure 4.2. Plot of estimates of the three parameters (σ_h, k_e, η) vs. location for the nadir beam data.

Since this sliding *centered* averaging filter is applied to already recorded data, this will not cause a problem. The central average is used simply to relate the filtered data points to those that immediately surround them. Figure 4.3 shows the result of applying an $M = 18$ sliding average filter to the estimates in Figure 4.2. Notice that the noisiness of the parameters that was seen in Figure 4.2 is significantly reduced in this filtered version, which makes the overall trend in the data more apparent. In general, the larger the averaging length, M, the smoother the data becomes. However, making M too large will smooth the data too much; in the limit of $M \rightarrow N$ (the number of available parameter estimates), the filter output is one value, which is the average of all the estimated parameter values.

A question arises that must be addressed. Should the parameter estimation really be based on a series of given averaged waveforms, then apply the smoothing filter? Or should a greater number of waveforms be averaged before estimating the parameters, thus eliminating the need for the smoothing filter? No matter how many individual waveforms are averaged before the estimation is performed, the estimation results for a sequence of averaged waveforms will be noisy to some degree. The reason for averaging more is to reduce the noisiness of these waveforms, but there is the risk that the first and last waveforms in the average might be returns from somewhat different media. Thus a trade-off is created between noisiness and loss of resolution in the parameter estimates. By averaging only 100 individual returns to obtain the average waveforms, the loss of resolution is hopefully avoided. Performing the filtering at this point then effectively reduces the noisiness in the results, providing a better look at the overall behavior of the parameters. One might argue that there is no difference in how averaging is done as long as a trend can be identified. Performing the estimation as described above provides more control in how much detail is desired in the estimates. The filtering can be performed very rapidly after the estimation is done, so that different filtering levels can be compared without redoing the waveform averaging or parameter estimation.

Returning to Figure 4.3, notice that the extinction value generally decreases as latitude increases toward the upper end of the flight line, which means that the pulse penetration is increasing. At the same time the value of η is generally increasing, indicating a greater amount of volume scattering in the combined scattering. Both of these observations agree with the general description of the ice sheet as given by Benson [4] (see Chapter 1). The exceptions are in the region around 70°N where the extinction

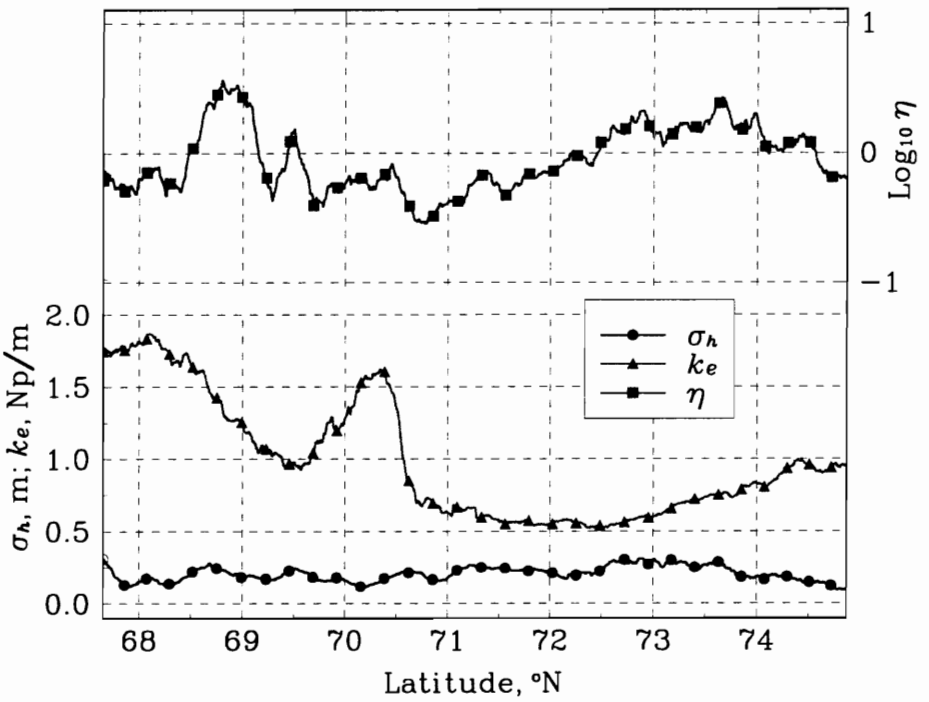

Figure 4.3. Filter output for the parameter estimates of the nadir beam shown in Figure 4.2. The filter length is $M = 18$.

value suddenly jumps up and at about 69° where the value of η suddenly increases. Also notice near the end of the data, where the extinction value begins to increase while the η value decreases. This implies that less penetration and less volume scattering is occurring, which according to Benson's description should not happen. The surface roughness appears to be relatively constant, another rather unexpected result. Surface observations by experimenters [4,15,38] indicate that the snow surface is relatively smooth in the dry snow regions when compared to the lower (soaked, ablation and percolation) regions, so the surface roughness values should be decreasing as latitude increases. A possible cause for these anomalous observations is the suspected saturation of the nadir channel's receiver, due to the high received power that was common to the nadir data during this mission.

Figure 4.4 shows the corresponding filtered values of recorded AGC and resulting values of F_{min} for the nadir beam data. F_{min} is the minimum value of (4-1) that was found for each waveform fit that resulted in the values of σ_h, k_e and η given in Figure 4.3. The AGC values show that the system was well above the upper limit of 160 for essentially the entire flight. This in itself may be the cause of these conflicting results, but this is purely speculation since the excessive power level effects on the receivers are not yet understood (see Chapter 3). The value of F_{min} is thus a good measure of how well the given models waveform fit the averaged altimeter waveforms. Figure 4.4 indicates that these fits were fairly good in the beginning of the flight line, then started to degrade after 70°N.

Figures 4.5-7 show some specific examples of how well the estimation program found a combination of parameters to fit the averaged waveforms. It is worth noting that these are individual fits to averaged waveforms; an adjacent waveform fit may be slightly different. An effort was made to find examples that were fairly representative of the specific regions along the flight path. The first example is typical of those waveforms in the soaked region of the flight line. Figure 4.5 shows an averaged waveform from 67.7°N, 49.7°E along with the best model fit. The fit parameters for this example were $\sigma_h = 0.24$ m, $k_e = 1.20$ Np/m and $\eta = 0.251$. This translates into a strongly surface-scattered waveform (about four times stronger than the volume scattered part). An example of a typical averaged waveform from the dry snow region is shown in Figure 4.6. Specifically it is from 72.9°N, 41.9°E, where the fit parameters were found to be $\sigma_h = 0.20$ m, $k_e = 0.60$ Np/m and $\eta = 2.512$. This waveform is dominated by volume

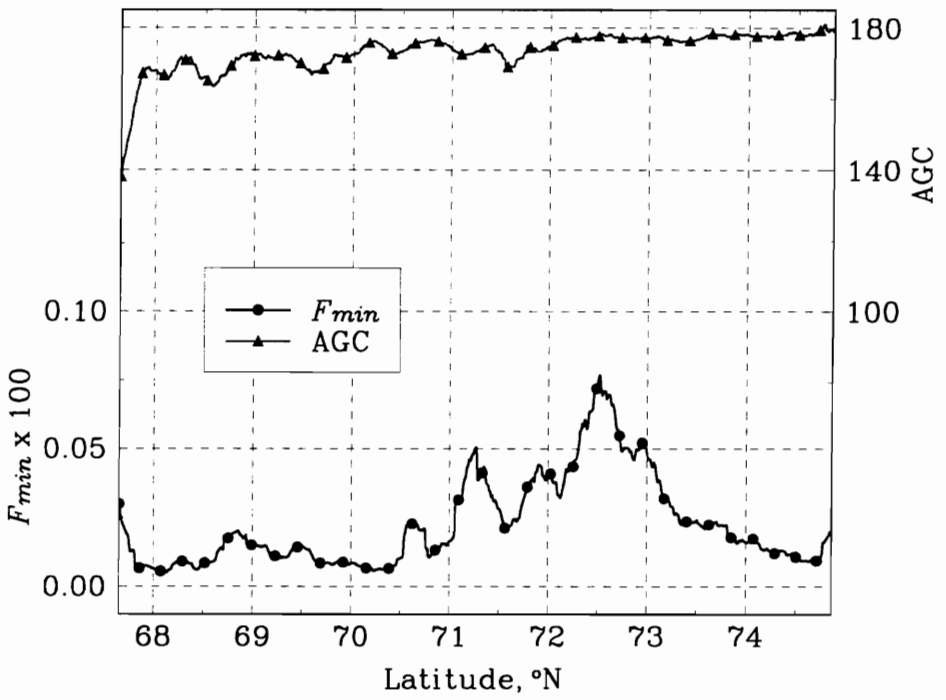

Figure 4.4. Plot of the minimum value of F and AGC vs. location for the nadir beam data. The larger the AGC number, the higher the backscattered power. The larger the value of F_{min}, the poorer the model fit to the waveform data.

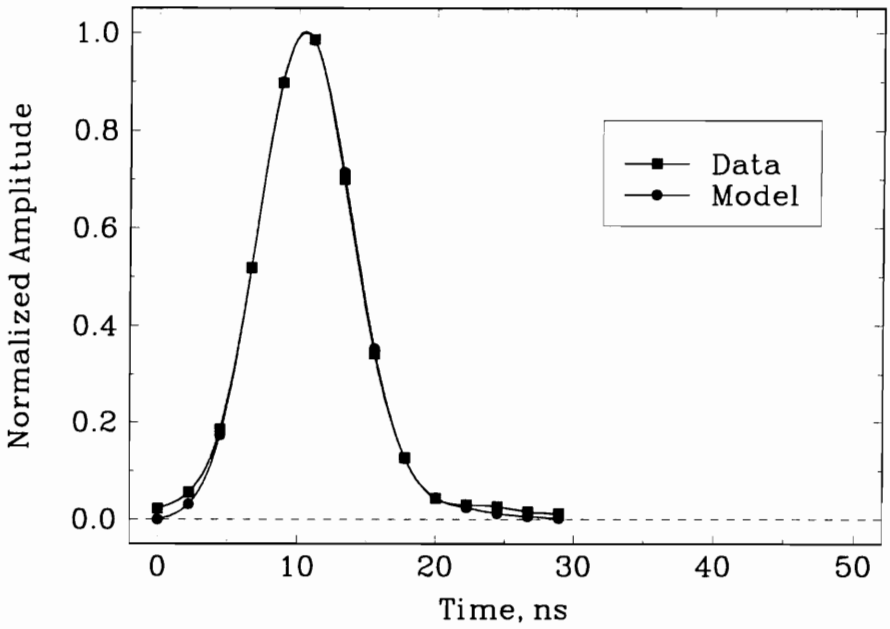

Figure 4.5. Example of the resulting nadir waveform fit performed by the estimation program. This waveform is common to those seen in the soaked and ablation regions of Greenland. The parameters are $\sigma_h = 0.24$ m, $k_e = 1.20$ Np/m and $\eta = 0.251$. The radar altitude is 539 m and $\xi = 2.14°$.

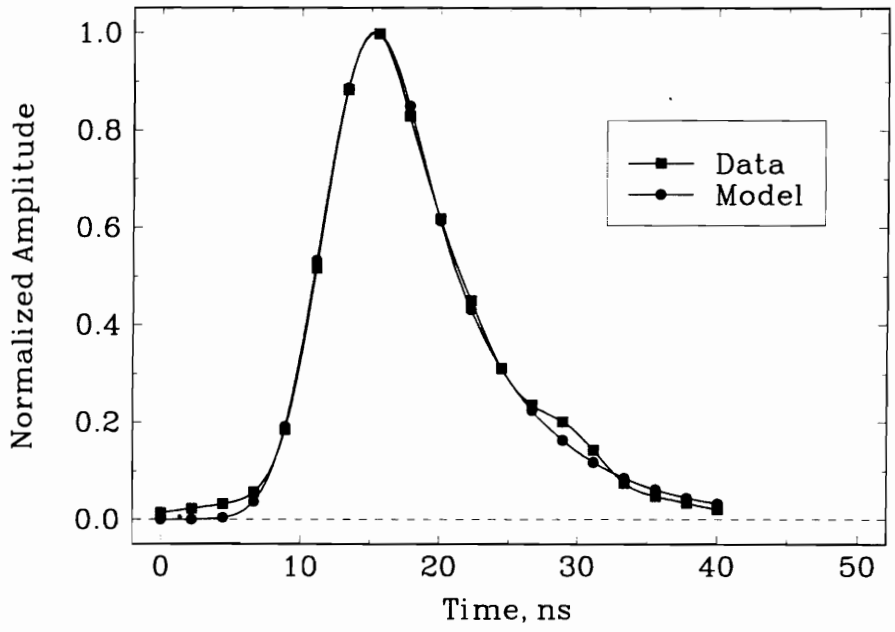

Figure 4.6. Example of the resulting nadir waveform fit performed by the estimation program. This waveform is common to those seen in the dry snow region of Greenland. The parameters are $\sigma_h = 0.20$ m, $k_e = 0.6$ Np/m and $\eta = 2.512$. The radar altitude is 406 m and $\xi = 2.65°$.

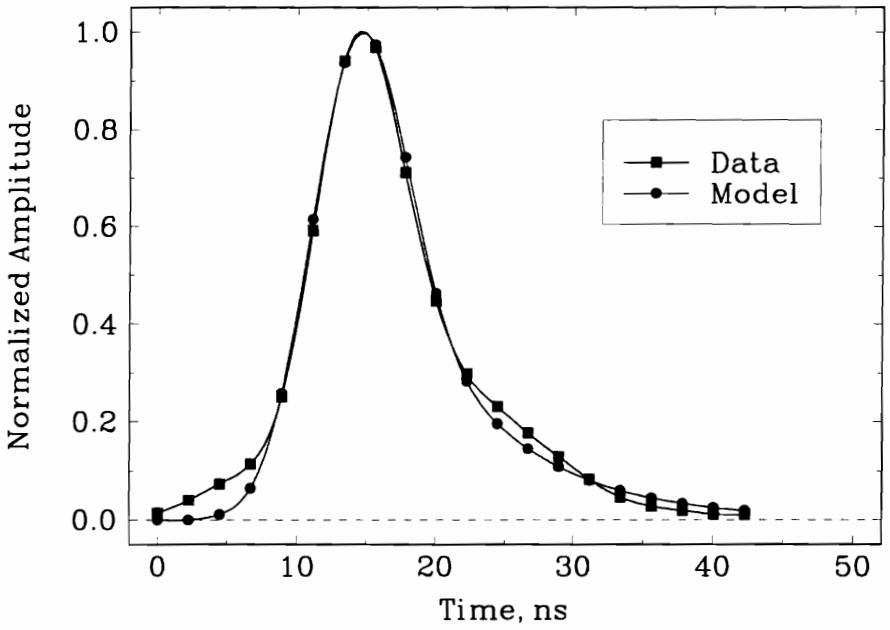

Figure 4.7. Example of the resulting nadir waveform fit performed by the estimation program. This waveform is common to those seen in the percolation region of Greenland. The parameters are $\sigma_h = 0.28$ m, $k_e = 0.55$ Np/m and $\eta = 0.631$. The radar altitude is 438 m and $\xi = 1.30°$.

scattering; the volume portion is 2.5 times greater than the surface scattering. Both of these examples (as well as all that follow) have the same time scale. Notice how the dry snow return has a slower decay in the tail region than the soaked region waveform, indicative of the pulse penetration. Figure 4.7 shows a waveform average from the percolation region (at 71.3°N, 44.8°E), an area where the scattering is due to both the surface and volume. For this waveform, the fit parameters are $\sigma_h = 0.28$ m, $k_e = 0.55$ Np/m and $\eta = 0.631$, which reflects the mixed nature of the medium. This waveform decays a bit more rapidly than the dry snow example, but still exhibits some penetration behavior. It is apparent from these examples that the waveform fitting is performed very well. The problem is that the higher than desired AGC values for this beam indicate that the averaged waveforms themselves may not be reliable.

Data from the other beams need to be examined to see if the anomalous behavior seen in the parameter estimates for the nadir beam is common to the whole system or only to that channel. Figure 4.8 shows the three fit parameters for the left beam data and Figure 4.9 shows the corresponding AGC and F_{min} values. Again these data are filtered the same way as was done for the nadir data in Figures 4.3 and 4.4. In this case, the AGC values (on average) never go much above 140, so saturation should not be a factor. Indeed, the fit parameters in Figure 4.8 appear to be better behaved when compared to those for nadir in Figure 4.3. The extinction values are decreasing while the η values are increasing and there are no large deviations from these trends as was seen in the nadir case. These trends indicate an expected increase in contribution by volume scattering as well as deeper penetration depths as latitude increases. The interesting exception in the left beam data is that the surface roughness seems to be increasing slightly with latitude. As discussed above, the surface roughness is expected to decrease as the flight progresses. While this increase is rather small, it still raises some concern. Also notice that the values for F_{min} shown in Figure 4.9 are in general just a little larger than was seen in the nadir data. This indicates that the waveform fits are not quite as good, even though they are not that much worse.

Examples of the left beam waveform fits for the various regions are given in Figures 4.10-12. The first, in Figure 4.10, is an example waveform fit from the same soaked region as examined in Figure 4.5, located at 67.7°N, 49.7°E. The fit parameters are similar to those from the nadir case: $\sigma_h = 0.26$ m, $k_e = 0.65$ Np/m and $\eta = 0.316$, except the extinction value is somewhat lower. This may be due to the fact that the volume

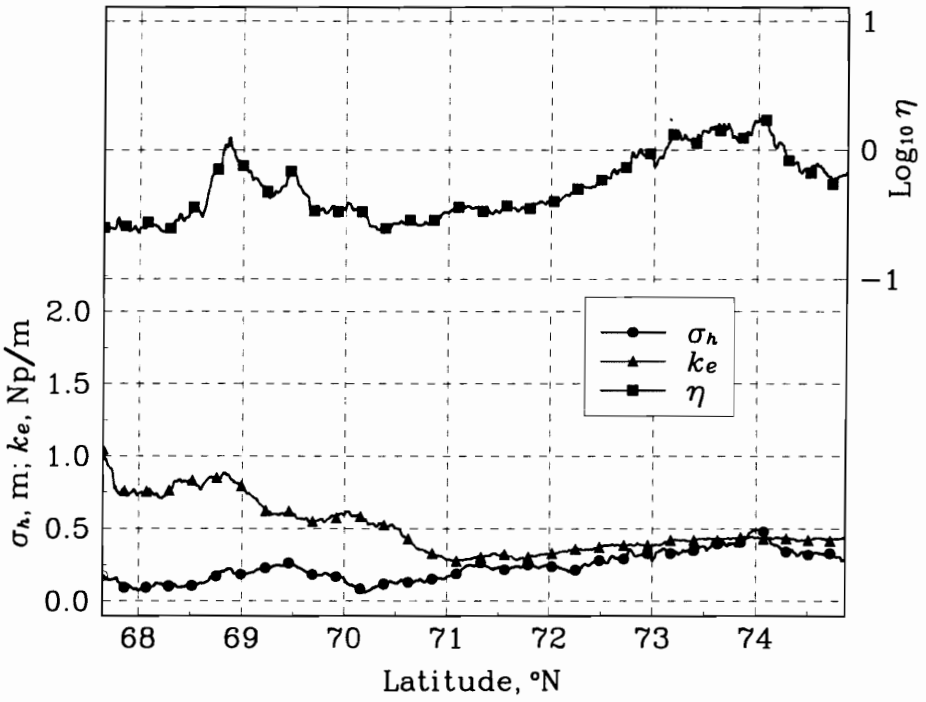

Figure 4.8. Plot of the three parameters (σ_h, k_e, η) vs. location for the left beam data. The filter length is $M = 18$.

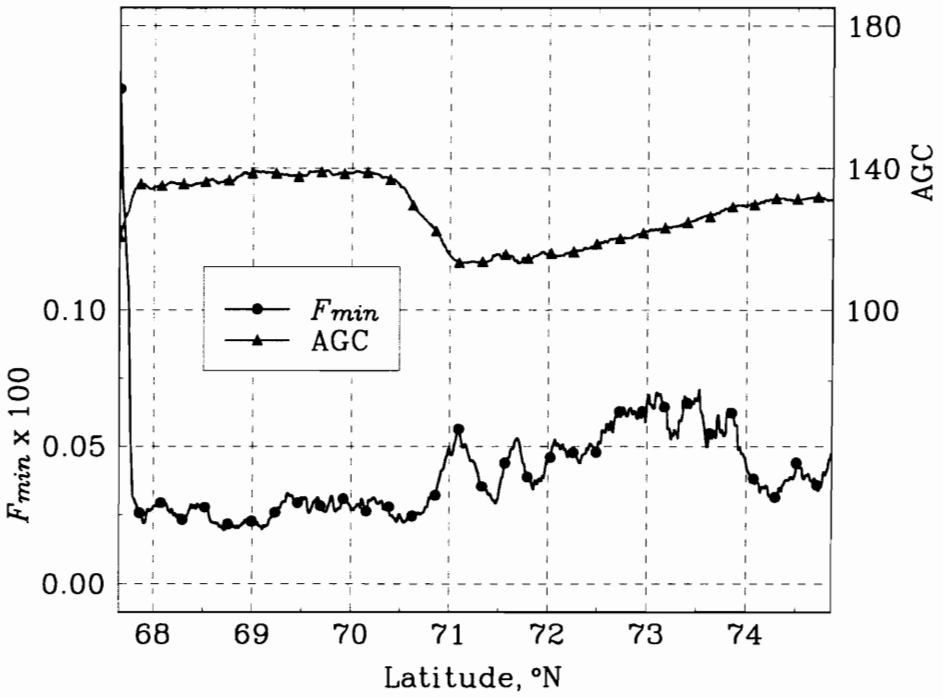

Figure 4.9. Plot of the minimum value of F and AGC vs. location for the left beam data.

portion is not as strong as the surface portion (about one-third as strong), so the extinction value will not be as influential to the overall waveform. Still, the comparison is good. Figure 4.11 shows the left beam example of a dry snow region waveform with its model fit. The location was the same as the nadir case, 72.9°N, 41.9°E, and the fit parameters are $\sigma_h = 0.16$ m, $k_e = 0.40$ Np/m and $\eta = 1.585$. Again, the comparison to the nadir case (Figure 4.6) is good and the longer tail of the waveform is present. The left beam example of a waveform from the percolation region is shown in Figure 4.12, from the same location (71.3°N, 44.8°E) as for the nadir example in Figure 4.7. Yet again the parameter values indicate the mixed nature of the medium: $\sigma_h = 0.28$ m, $k_e = 0.40$ Np/m and $\eta = 0.631$. These values are very close to those in the nadir case.

Figure 4.13 shows the fit parameters for the right beam. The trends are very similar to those for the left beam data in Figure 4.8, except that the initial extinction estimates are higher and the overall trend in η is shifted slightly lower. Still, the agreement between left and right beam data is very good. Figure 4.14 shows the AGC and F_{min} values for the right beam. The AGC values are a little higher than for the left beam (cf. Figure 4.9), but are still safely below 160. The F_{min} values are essentially the same, indicating a similar level of error in the model fits for the left and right beam data.

Figures 4.15-17 show the waveform fit examples for the right beam. The soaked region waveform is shown in Figures 4.15, with it's fit parameters given by $\sigma_h = 0.16$ m, $k_e = 0.95$ Np/m and $\eta = 0.200$. This strongly surface scattered waveform has a lower roughness value than the previous examples, but this could be due to the possibility that the right beam was actually illuminating a smoother area than the other beams were at this time. The soaked region is by no means a uniform surface. It has smooth as well as rough areas distributed across it, so such results are to be expected in this region. Figure 4.16 shows the right beam example of a dry snow waveform. The fit parameters in this case are $\sigma_h = 0.12$ m, $k_e = 0.45$ Np/m and $\eta = 1.585$, which are in excellent agreement with the left beam, and very similar to those for the nadir beam. These values may be more acceptable since the nadir beam values are derived from data that may have been in saturation. The agreement between the off-nadir beams reinforces this. Finally, Figure 4.17 shows the right beam example for the percolation region. The fit parameters are $\sigma_h = 0.18$ m, $k_e = 0.30$ Np/m and $\eta = 0.316$, which indicates a relatively strong surface scattered waveform. This is not unexpected since the percolation region is so variable in terms of the scattering sources. In this case it appears that the right beam illuminated a

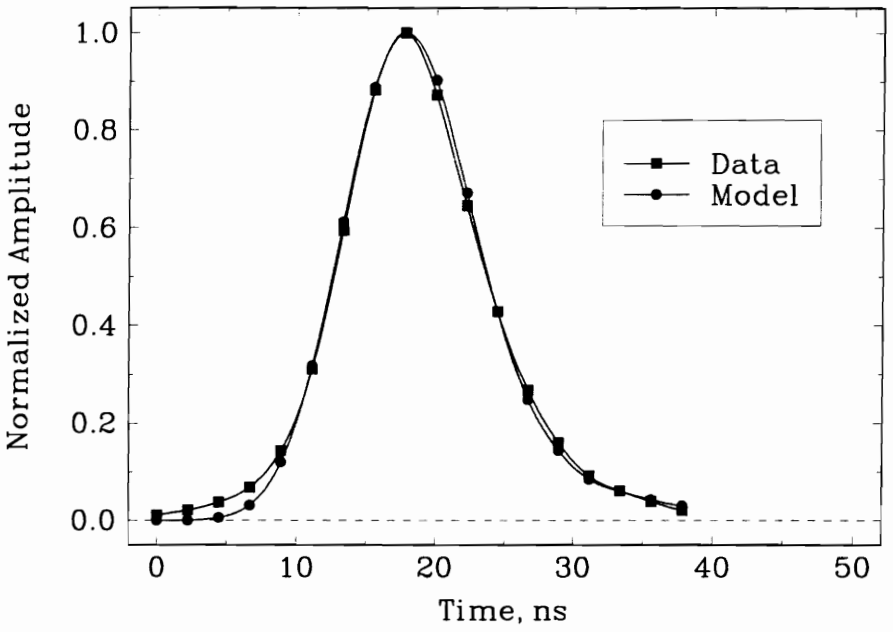

Figure 4.10. Example waveform fit for the left beam in the soaked region. The parameters are $\sigma_h = 0.26$ m, $k_e = 0.65$ Np/m and $\eta = 0.316$. The radar altitude is 537 m and $\xi = 11.81°$.

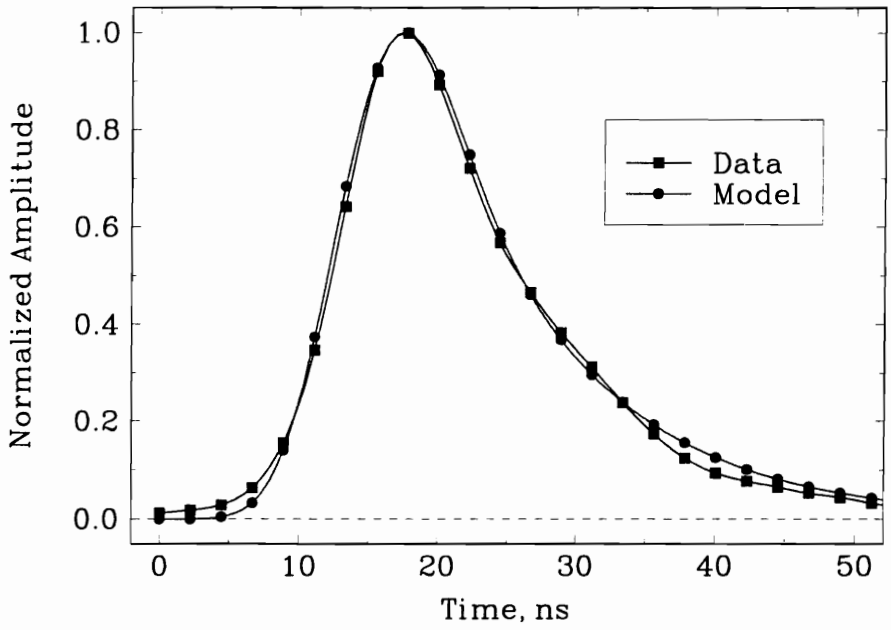

Figure 4.11. Example waveform fit for the left beam in the dry snow region. The parameters are $\sigma_h = 0.16$ m, $k_e = 0.40$ Np/m and $\eta = 1.585$. The radar altitude is 414 m and $\xi = 12.60°$.

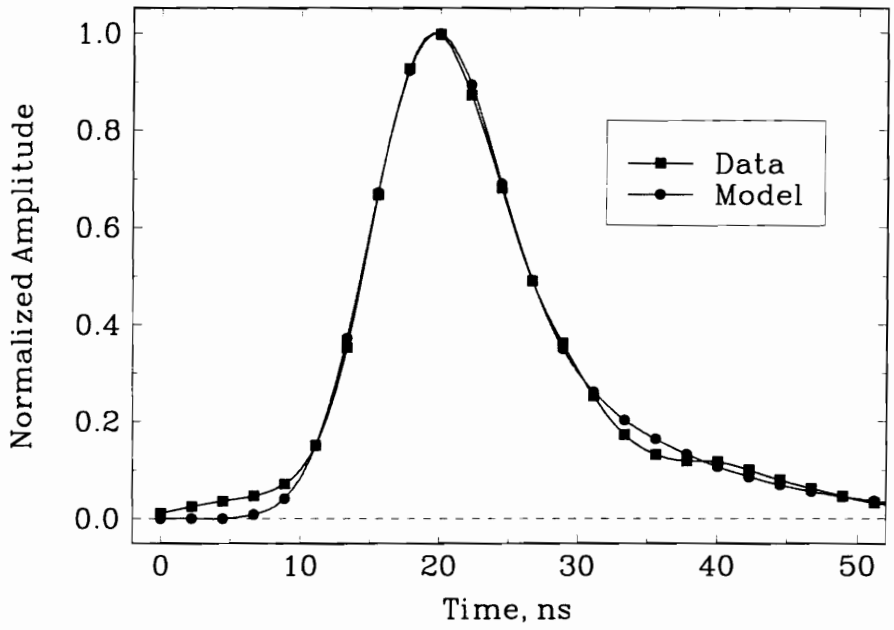

Figure 4.12. Example waveform fit for the left beam in the percolation region. The parameters are $\sigma_h = 0.28$ m, $k_e = 0.40$ Np/m and $\eta = 0.631$. The radar altitude is 438 m and $\xi = 12.80°$.

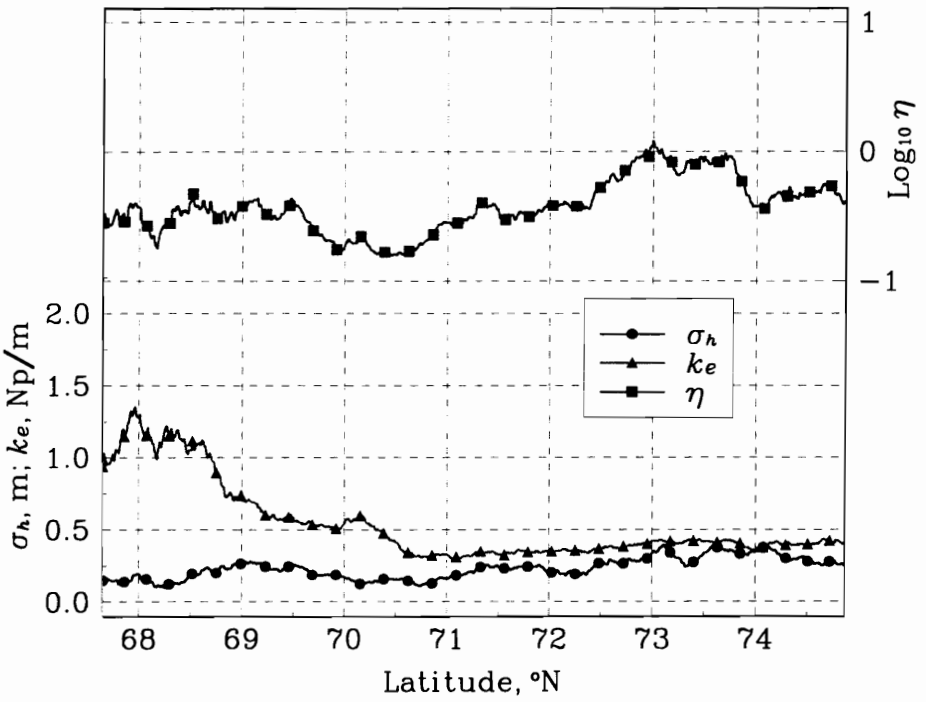

Figure 4.13 Plot of the three parameters (σ_h, k_e, η) vs. location for the right beam data. The filter length is $M = 18$.

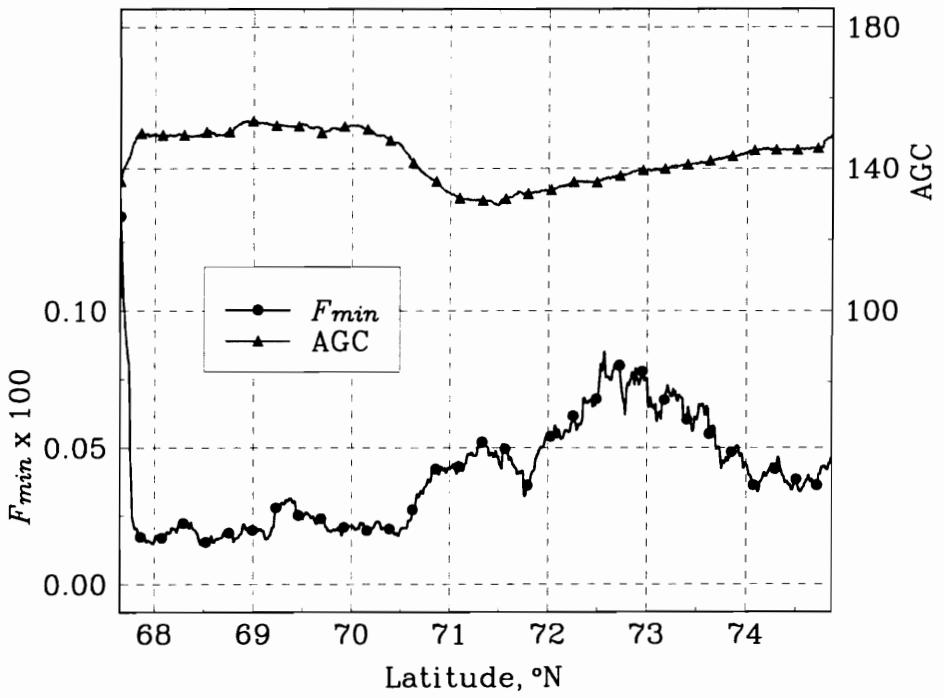

Figure 4.14 Plot of the minimum value of F and AGC vs. location for the right beam data.

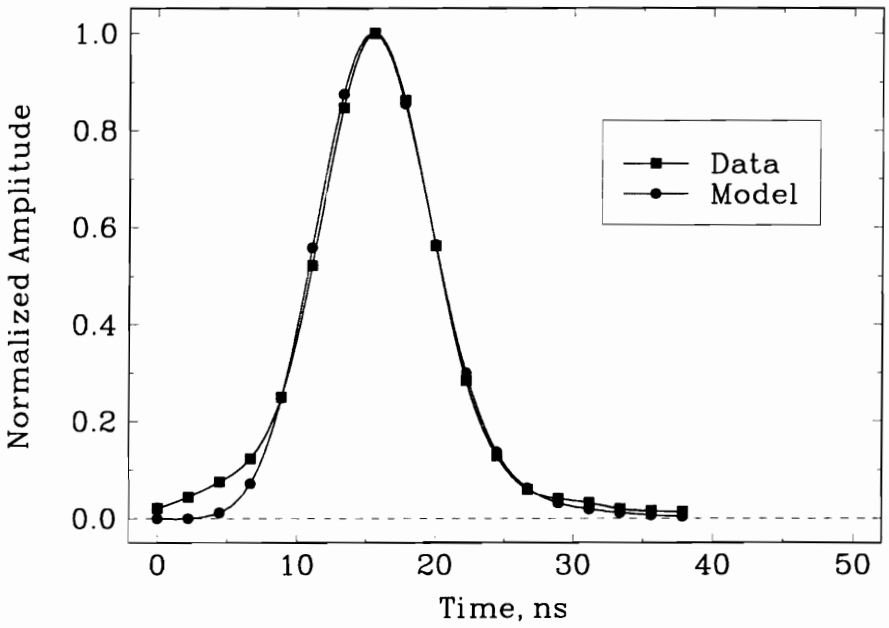

Figure 4.15. Example waveform fit for the right beam in the soaked region. The parameters are $\sigma_h = 0.16$ m, $k_e = 0.95$ Np/m and $\eta = 0.200$. The radar altitude is 494 m and $\xi = 12.20°$.

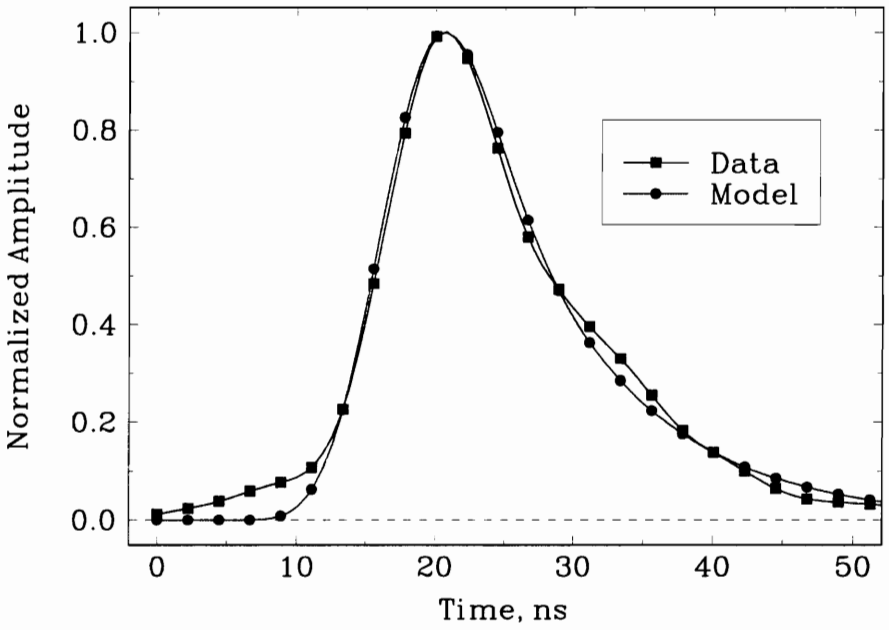

Figure 4.16. Example waveform fit for the right beam in the dry snow region. The parameters are $\sigma_h = 0.12$ m, $k_e = 0.45$ Np/m and $\eta = 1.585$. The radar altitude is 412 m and $\xi = 13.06°$.

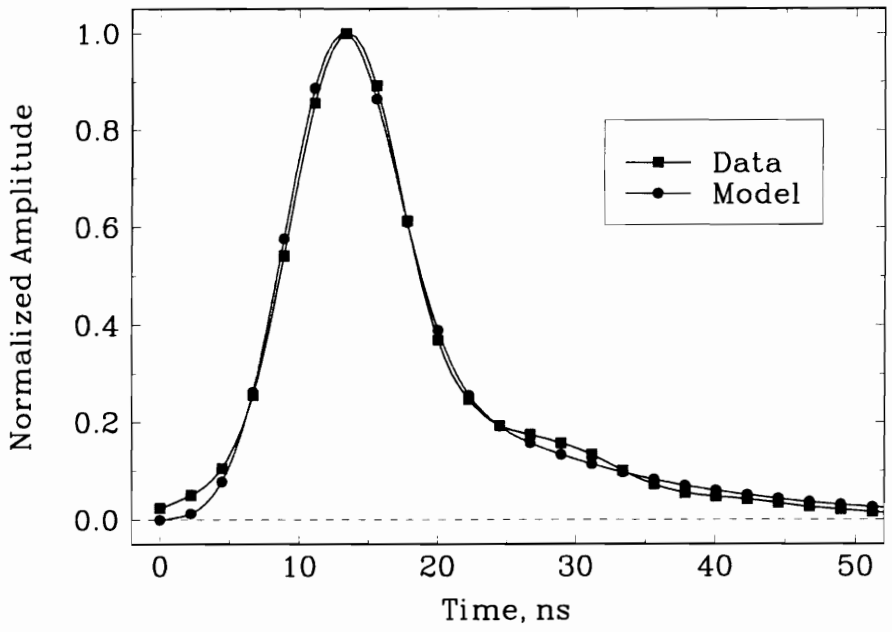

Figure 4.17. Example waveform fit for the right beam in the percolation region. The parameters are $\sigma_h = 0.18$ m, $k_e = 0.30$ Np/m and $\eta = 0.316$. The radar altitude is 433 m and $\xi = 12.95°$.

particularly strong surface scattering area within this region.

Table 4.3 summarizes the specific waveform fitting examples for each location and beam. The table is organized so that parameter comparison can be easily made between the MARA channels. Notice that for each beam, the surface roughness is smallest in the dry snow region as is expected. That value is expected to be greatest in the soaked region, but instead is in the percolation region. This is somewhat unexpected but not unreasonable. For each beam, the extinction coefficient values decrease as the flight progressed from the soaked to percolation to dry snow regions, which is an expected result. The η values also show an increase from region to region, once again as expected. These specific examples seem to show that the data follows the expected results, but the overall trends are more descriptive of the parameter behavior over the whole flight line.

Overall, the off-nadir data seems to provide a more consistent view of the behavior of the medium parameters. The only point in question is the generally increasing surface roughness values, which are expected to decreases as the altimeter flies from the rougher soaked and ablation zones into the smoother dry snow region. Since the surface roughness value is very sensitive to the leading edge slope of the averaged waveform, any errors in the averaging process that affect the leading edge slope will directly affect this value. Chapter 3 discussed the peak-alignment method that was used to retrack the altimeter data before the averaging was performed. This method works quite well when the individual waveforms do not experience *intra-pulse* fading (this is when fading occurs within the time extent of the received waveform). Most (but not all) of the individual returns for MARA do not experience a significant degree of this type of fading, simply because the extremely beamwidth-limited nature of the system generates such short-duration return pulses. Examination of the individual MARA returns shows that there are in fact a small number of waveforms that have this type of fading, so the peak alignment method for retracking may not be the best for this system. Other retracking methods should then be examined to see if they improve the resulting parameter estimation.

Another observation is that the very leading edge portions of the averaged waveforms do not fit the modeled waveforms very well. This was most noticeable in the ice sheet returns, but was also observed in the earlier water data as well (see Figure 3.5). This "front porch" feature is thought to be a problem associated with the relatively crude peak alignment retracking method that was used for all this data. Hopefully this can be

Table 4.3. Summary of the parameter estimates for the September 20, 1991 south-to-north leg of the MARA flight.

Benson Zone		soaked	percolation	dry snow
Location	Lat. (°N)	67.7	71.3	72.9
	Lon. (°E)	49.7	44.8	41.9
Parameter	Beam			
σ_h (m)	Nadir	0.24	0.28	0.20
	Left	0.26	0.28	0.16
	Right	0.16	0.18	0.12
k_e (Np/m)	Nadir	1.20	0.55	0.60
	Left	0.65	0.40	0.40
	Right	0.95	0.30	0.45
η	Nadir	0.251	0.631	2.512
	Left	0.316	0.631	1.585
	Right	0.200	0.316	1.585

rectified with a more refined retracking method.

These examples demonstrated the performance of the parameter estimation program and the combined model that it is based upon. The general regional dependence of the trends for surface roughness, effective extinction coefficient and volume-to-surface contribution ratio were for the most part correctly identified. The problems that were encountered resulted from using waveform data having known deficiencies. If it was not suspected saturation or nonlinear detector effects, it was retracking errors that tainted the waveform data. After all, the parameter estimates can only be as good as the data from which they are derived.

Chapter 5
Conclusions

In this research, an improved volume scattering model was developed to be used with a general surface scattering model in a combined surface and volume scattered waveform model. This combined scattering model can be used to model altimeter waveforms from arbitrary pointing angle, radar altitude and antenna pattern, something that cannot be done with previous scattered waveform models. Examples were given that indicate the advantages of using a low altitude, beamwidth-limited altimeter to examine the effects of volume penetration on altimeter data.

The altimeter data that is used to demonstrate the use of the combined model is taken from the Multimode Airborne Radar Altimeter. The steps necessary to preprocess the data are outlined. These include non-linear detector correction, true pointing angle determination, waveform retracking and splining. To ensure that the model behaves well, it is compared to data obtained during the 1991 Greenland mission from open water. Upon checking the statistics of this return waveform data, unexpected problems were encountered. Attempts were then made to correct for these problems, but ultimately were not successful. The Greenland ice sheet data is still used for analysis of parameter variation over its extent, but the fact that the data may not be perfect requires the understanding that the resulting analysis may be in error.

Specific examples of fitting this model to real altimeter data have been given, which demonstrate the dependence of penetration and scatter mechanism on location over the Greenland ice sheet, where known regional differences exist in the random medium that is the ice sheet. While suspected problems with these data leaves a desire for better data to examine for penetration effects, the estimation algorithm was shown to work very well in fitting model waveforms to averaged data.

This research also opens up other subjects for possible future research. The use of a more efficient estimation algorithm would greatly improve the implementation of this method to find the descriptive parameters of the scattering media. While the brute-force method used in this research does its job quite well, it has to search through all combinations of expected fit parameters to find the best combination for a given data

waveform. One of the minimization techniques mentioned in §4.1.1 that has promise is the conjugate-gradient method. Since this method requires the calculation of gradient information, deriving expressions for the derivative of the FSIR and VSIR equations in Chapter 2 provides an area for future research.

A more involved area of research would include performing another experiment that would collect beamwidth-limited data. Certain problems with the existing MARA system have been identified and can be corrected before performing another mission. One of these problems discussed in this work is the excessive signal strength that caused the AGC levels to be too high, causing suspected saturation of the MARA receiver. Future missions can be conducted from a higher altitude or by using a lower transmit power level to remedy this problem. Also, the nonlinear detectors used in the MARA system, should be more thoroughly tested or even replaced with better-behaved units. This nonlinearity is accounted for in the data averaging program, but this correction is by no means ideal. The MARA system in concept is an excellent tool for use in studying the penetration phenomenon, but in practice it leaves much to be desired.

Investigation of other waveform retracking methods would be useful as well. The methods listed in §3.1.3 were designed for pulsewidth-limited, high altitude systems that have return waveforms which are very long, at least when compared to the MARA waveforms. Because of the unique waveform behavior of the MARA, these methods do not work as well as desired. The peak alignment method that is used in this work is acknowledged to be rather crude. A promising technique relies on splining the individual returns waveforms, then retracking them based on a centroid location. Implementation of this scheme should not be too difficult, but it will increase the time required to compute the average waveforms.

Another possible topic for research is the possible application of this model to layered media, such as sea ice. As it is given now, the model assumes that the discrete random medium is a homogenous volume. Modification of the VSIR equations should be possible to account for a layer feature, but the resulting expressions are expected to be much more complicated. Maybe other simplifications can be made to reduce the complexity of such expressions, but much work is necessary to find this out. Also, investigation of whether the randomly rough interface affects the volume scattering model should be performed. Currently the combined model assumes that the surface model accounts for the rough interface, but this is an assumption that needs to be checked.

Finally, application of this model and the parameter estimation algorithm as it exists to other aircraft altimeter data and satellite altimeter data may provide a complimentary view of the penetration process. The University of Massachusetts' AAFE altimeter was present on board the same aircraft as the MARA system during the 1991 Greenland experiment and has revisited Greenland since then. Much pulsewidth-limited, nadir-looking data exists for that instrument, which would provide an interesting side-by-side comparison for differing frequencies and configurations. Currently, the European Space Agency's ERS-1 satellite is operating and recording waveform data for much of the polar regions. Soon the ERS-2 is to be launched, which will provide even more waveform data for examination. These instruments have fairly narrow beamwidths, but their enormously different altitude (compared to the MARA system) will provide very different waveforms that may be affected by penetration differently than low altitude data.

Chapter 6
References

[1] Abramowitz, M., and I. A. Stegun, eds., *Handbook of Mathematical Functions*, Dover Publications, Inc., New York, 1972.

[2] Barrick, D. E., and C. T. Swift, "The Seasat microwave instruments in historical perspective," *IEEE J. Oceanographic Eng.*, vol. 5, pp. 74-79, 1980.

[3] Bender, C. M., and S. A. Orzag, *Advanced Mathematical Methods for Scientists and Engineers*, McGraw-Hill, Inc., New York, 1978.

[4] Benson, C. S., *Stratigraphic studies in the snow and firn of the Greenland ice sheet,* U. S. Army Snow Ice and Permafrost Research Establishment (SIPRE), Research Report 70, 1962.

[5] Bohren, C. F., and D. R. Huffman, *Absorption and Scattering of Light by Small Particles,* John Wiley & Sons, New York, 1983.

[6] Bracewell, R. N., *The Fourier Transform and Its Applications*, McGraw-Hill, Inc., New York, 1986.

[7] Brigham, E. O., *The Fast Fourier Transform*, Prentice-Hall, Englewood Cliffs, NJ, 1974.

[8] Brown, G. S., "The average impulse response of a rough surface and its applications," *IEEE Trans. Antennas and Propagation*, vol. 25, pp. 67-74, 1977.

[9] Brown, G. S., "A useful approximation for the flat surface impulse response," *IEEE Trans. Antennas and Propagation*, vol. 37, pp. 764-767, 1989.

[10] Brown, G. S., "Quasi-Specular Scattering from the Air-Sea Interface," *Surface Waves and Fluxes, Volume 2, Chapter 10*, Kluwer Academic Publishers, The Netherlands, 1990.

[11] Cheng, D. K., *Field and Wave Electromagnetics, Second Edition*, Addison-Wesley, Reading, MA, 1989.

[12] Davenport, W. B., and W. L. Root, *An Introduction to the Theory of Random Signals and Noise*, IEEE Press, New York, 1989.

[13] Davis, C. H., and R. K. Moore, "A combined surface and volume scattering model for ice sheet radar altimetry," *J. Glaciology*, vol. 34, pp. 675-818, 1993.

[14] Davis, C. H., and H. J. Zwally, "Geographic and seasonal variations in the surface properties of the ice sheets by satellite-radar altimetry," *J. Glaciology*, vol. 39, no. 133, pp. 687-697, 1993.

[15] Ferraro, E. J., "Analysis of Airborne Radar Altimetry Measurements of the Greenland Ice Sheet," *Ph.D. Dissertation*, University of Massachusetts at Amherst, 1994.

[16] Hayne, G. S., "Radar Altitude Mean Return Waveforms from Near-Normal-Incidence Ocean Surface Scattering," *IEEE Trans. Antennas and Propagation*, vol. 28, pp. 687-692, 1980.

[17] Ishimaru, A., *Wave Propagation and Scattering in Random Media, Vols. 1 & 2*, Academic Press, New York, 1978.

[18] Jackson, L. B., *Digital Filters and Signal Processing*, Kluwer Academic Publishers, Boston, MA, 1986.

[19] Johns Hopkins University Technical Digest, *Johns Hopkins APL Technical Digest*, vol. 8, no. 2, 1987.

[20] Kuga, Y., F. T. Ulaby, T. F. Haddock and R. D. DeRoo, "Millimeter-wave radar scattering from snow 1. Radiative transfer model," *Radio Science,* vol. 26, pp. 329-341, 1991.

[21] Lang, R., and J. Sidhu, "Electromagnetic scattering from a layer of vegetation," *IEEE Trans. Geoscience and Remote Sensing*, vol. 21, pp. 62-71, 1983.

[22] LeVine, D. M., R. H. Lang and Y. Lin, "Transient Response of a Layer of Discrete Random Media Over a Dielectric Half Space," *IEEE Trans. Geoscience and Remote Sensing*, vol. 30, pp. 1034-1045, 1992.

[23] McGoogan, J. T., L. S. Miller, G. S. Brown and G. S. Hayne, "The S-193 radar altimeter experiment," *Proc. IEEE*, vol. 62. pp. 793-803, 1974.

[24] Milton, J. S., and J. C. Arnold, *Probability and Statistics in the Engineering and Computing Sciences*, McGraw-Hill, New York, 1986.

[25] Moore, R. K., and C. S. Williams, Jr., "Radar Terrain at Near-Vertical Incidence," *Proc. IRE*, vol. 45, pp. 228-238, 1957.

[26] Newkirk, M. H., and G. S. Brown, "Issues Related to Waveform Computations for Radar Altimeter Applications," *IEEE Trans. Antennas and Propagation,* vol. 40, pp. 1478-1488, 1992.

[27] Parsons, C. L., and L. S. Miller, "Design of a Large-Aperture Lens Antenna Usable over a $\pm$ 15° Scanning Sector," *IEEE Trans. Antennas and Propagation,* vol. 36, pp. 1162-1165, 1986.

[28] Parsons, C. L., ed., *MARA System Documentation, Volume I - MARA System Requirements Document*, NASA Reference Publication 1226, 1989.

[29] Press, W. H., B. P. Flannery, S. A. Teukolsky and W. T. Vetterling, *Numerical Recipes*, Cambridge University Press, New York, 1989.

[30] Rahmat-Samii, Y., "Useful Coordinate Transformation for Antenna Applications," *IEEE Trans. Antennas and Propagation*, vol. 27, pp. 571-574, 1979.

[31] Ridley, J. K., and K. C. Partington, "A model of satellite radar altimeter returns from ice sheets," *Int. J. Remote Sensing,* vol. 9, pp. 601-624, 1988.

[32] Rodriguez, E. "Altimetry for Non-Gaussian Oceans: Height Biases and Estimation of Parameters," *J. Geophys. Res.*, vol. 93, no. C11, pp. 14,107-14,120, 1988.

[33] Special Issue on Geos-3, *J. Geophys. Res.*, vol. 84, no. B8, 1979.

[34] Swift, C. T., P. S. Hayes, J. S, Herd, W. L. Jones and V. E. Delnore, "Airborne Microwave Measurements of the Southern Greenland Ice Sheet," *J. Geophys. Res.*, vol. 90, pp. 1983-1994, 1985.

[35] Thomas, R. H., "Polar Research from Satellites," Joint Oceanographic Institutions, Inc., Washington, DC, 1991.

[36] Townsend, W. F., "An initial assessment of the performance achieved by the Seasat-1 radar altimeter," *IEEE J. Oceanographic Eng.*, vol. 5, pp. 80-92, 1980.

[37] Ulaby, F. T., R. K. Moore and A. K. Fung, *Microwave Remote Sensing - Active and Passive, Vols. I-III*, Addison-Wesley, Reading, MA, 1982.

[38] Vandemark, D. C., various private communications, 1993-94.

[39] Wolfram, S, *Mathematica for Windows, Version 2.2.2*, Wolfram Research Inc., Champaign, IL, 1994.

Appendix A
Beamwidth-Limited vs. Pulsewidth-Limited Altimetry

For a given set of altimeter parameters, it would be convenient to have a method for determining whether the altimeter is operating in a beamwidth-limited or pulsewidth-limited mode. The qualitative difference between these two modes is that the illuminated area on the surface is determined by the antenna beamwidth or transmitted pulsewidth, respectively. This delineation is sketchy at best, so an expression is needed to provide a more definitive method to indicate which mode is being used.

In order to determine this criterion, the geometry of the altimetry system must be examined. Figure A.1 shows a nadir oriented antenna operating above a mean surface from an altitude h. The antenna beamwidth is given as BW and the transmitted pulsewidth is PW. In this figure the diameter of the area of the circle on the surface that is within the beamwidth is

$$d_b = 2h \tan\frac{BW}{2}. \tag{A-1}$$

Furthermore, the area of the circle formed by the intersection of the leading edge of the pulse when the trailing edge of the pulse just intersects the surface at the nadir point (as shown in Figure A.1) has a diameter given by

$$d_p = 2\sqrt{(h + c\,PW)^2 - h^2}. \tag{A-2}$$

As the pulse progresses in time, the illuminated area becomes an annulus that has an area that is equivalent to that shown in the figure, but weighted by the antenna pattern. When the maximum area created by the pulsewidth illumination, as shown in Figure A.1, is greater than that within the beamwidth, the altimeter is considered *beamwidth-limited*. In terms of diameters, this is when $d_p > d_b$, which is shown in Figure A.1(a). When $d_p < d_b$, the altimeter is *pulsewidth-limited* (Figure A.1(b)). Comparing (A-1) to (A-2) and solving for BW provides a condition that determines the altimeter operating mode

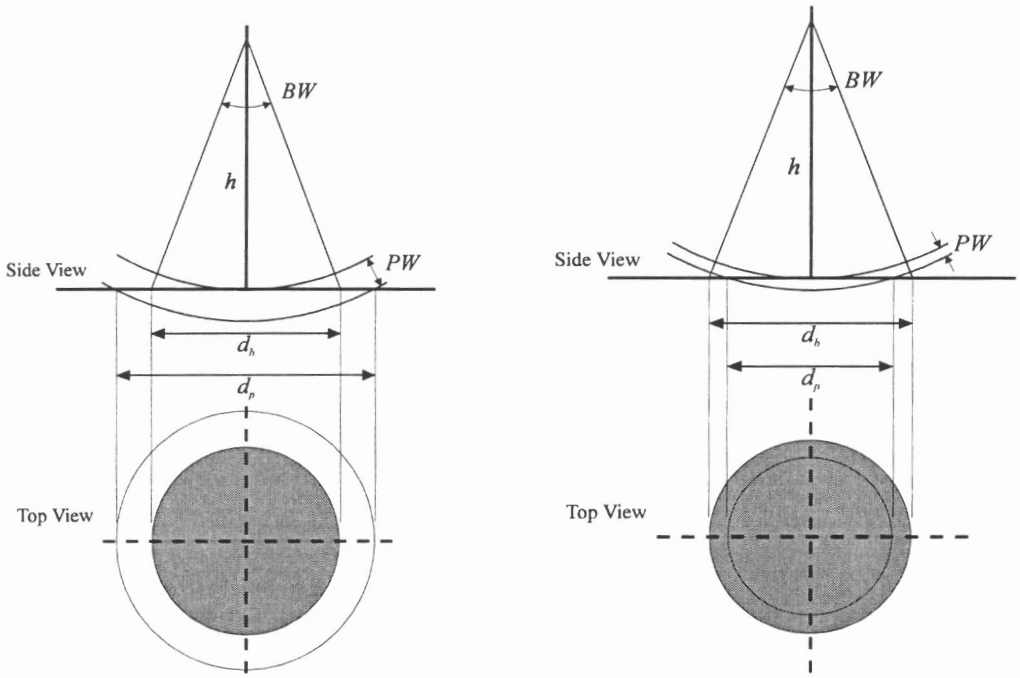

(a) (b)

Figure A.1. Geometry of a nadir oriented (a) beamwidth-limited altimeter ($d_p > d_b$) and (b) pulsewidth-limited altimeter ($d_p < d_b$).

for nadir pointing, i.e.,

$$\begin{aligned} BW &> 2\tan^{-1}\sqrt{\left(1+\frac{c}{h}PW\right)^2-1} \quad \rightarrow \quad \text{“pulsewidth-limited”} \\ BW &< 2\tan^{-1}\sqrt{\left(1+\frac{c}{h}PW\right)^2-1} \quad \rightarrow \quad \text{“beamwidth-limited”}. \end{aligned} \tag{A-3}$$

When the altimeter antenna is pointed away from nadir, the expressions given in (A-3) are not applicable; they must be modified to account for the pointing angle, ξ. Figure A.2 shows the geometry associated with an off-nadir oriented altimeter. The beamwidth-limited illuminated area is an ellipse, in this case defined by the intersection of the antenna beam (a cone) and the surface (a plane) at angle ξ. The major axis of this ellipse, as shown in Figure A.2 by d_b, is

$$d_b = h\left[\tan\left(\xi+\frac{BW}{2}\right)-\tan\left(\xi-\frac{BW}{2}\right)\right]. \tag{A-4}$$

The pulsewidth-limited illuminated area is now a sector of an annulus and its width is given by

$$d_p = h\left[\sqrt{\left(\sec\xi+\frac{c\,PW}{2h}\right)^2-1}-\sqrt{\left(\sec\xi-\frac{c\,PW}{2h}\right)^2-1}\right]. \tag{A-5}$$

Note that this area is limited in the radial direction only by the pulsewidth projection onto the surface, and is limited by the antenna beamwidth in the azimuthal direction. In other words, the pulsewidth-limited area is a segment of an annulus, while the beamwidth-limited area is an ellipse. As for the nadir oriented case, the equations given in (A-4) and (A-5) can be compared and solved for the BW to provide a condition for determining the operating mode. Trigonometric identities are used in (A-4) and the result is then solved for BW, which has two roots and only one is positive. Comparing d_b to d_p as before, the condition analogous to (A-3) is

$$\begin{aligned} BW &> 2\tan^{-1}\left\{\frac{\sqrt{1+(2+x^2)\tan^2\xi+\tan^4\xi}-\sec^2\xi}{x\tan^2\xi}\right\} \quad \rightarrow \quad \text{“pulsewidth-limited”} \\ BW &< 2\tan^{-1}\left\{\frac{\sqrt{1+(2+x^2)\tan^2\xi+\tan^4\xi}-\sec^2\xi}{x\tan^2\xi}\right\} \quad \rightarrow \quad \text{“beamwidth-limited”}, \end{aligned} \tag{A-6}$$

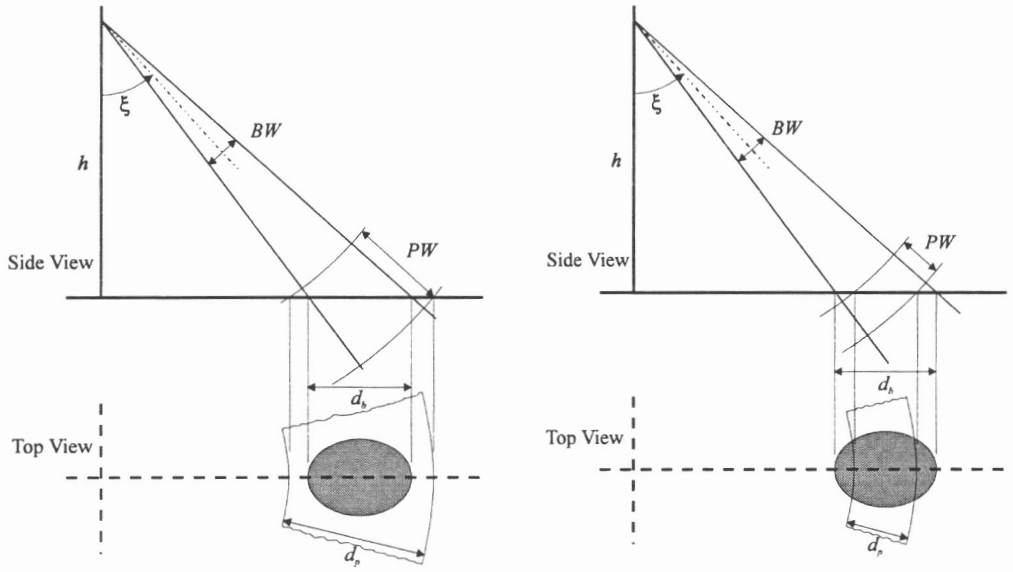

(a) (b)

Figure A.2. Geometry of an off-nadir oriented (a) beamwidth-limited altimeter ($d_p > d_b$) and (b) pulsewidth-limited altimeter ($d_p < d_b$).

where $x = d_p/h$ is used in (A-6) to simplify the expressions.

Note that if $\xi = 0°$, the beamwidth-limited diameter in (A-4) reduces to (A-1); however, the pulsewidth-limited diameter in (A-5) does not reduce to (A-2). This is because the pulsewidth-limited area is defined differently at nadir (a circle) and off-nadir (a sector of an annulus). The beamwidth-limited area definition is unchanged (an ellipse in both cases, specifically a circle at nadir). *For this reason, it is important to not apply the off-nadir condition in (A-6) to the nadir configuration.* The lower limit on ξ for which (A-5) is valid is determined by examining its form. The argument of the radical in the second term of (A-5) must be positive to avoid a non-real result. Thus, the first term of this argument must be greater than unity; solving this condition for ξ yields

$$\xi \geq \sec^{-1}\left[\ 1 + \frac{cPW}{2h}\right]. \tag{A-7}$$

Equation (A-7) *provides a lower limit for when* (A-6) *can be used.* Below this limit, the pulsewidth- and beamwidth-limited definitions become rather nebulous. Neither of the terms beamwidth-limited or pulsewidth-limited accurately describes the situation created when ξ is bounded by 0° and (A-7). When "identification" of the configuration is desired for some angle that is less than the limit given in (A-7), the nadir condition in (A-3) can be used. As long as the right hand side of (A-3) is not close to the beamwidth value, it is safe to say that the altimeter is either pulsewidth- or beamwidth-limited. If the right hand side of (A-3) is on the order of a beamwidth, the altimeter cannot in general be classified as either type.

These expressions provide a way to determine whether an altimeter is beamwidth- or pulsewidth-limited, for both nadir and off-nadir orientations. It is important to note that it is possible to have an altimeter that is beamwidth-limited when pointed at nadir and is pulsewidth-limited when pointed off-nadir, but the opposite can never be true. Also, any altimeter will become pulsewidth-limited when pointed far enough off-nadir, as in the case of surveillance radars. Regardless of pointing angle, the conditions given by (A-3) and (A-6) provide a convenient method to determine an altimeter's operating mode, subject to the condition noted in (A-7).

Appendix B
Range Coordinate Integration of the Volume Scattered Impulse Response

In Chapter 2, §2.2.1, the volume scattered impulse response (VSIR) was developed from the basic expression given by equation (2-9). With the expression for σ_V^o given by (2-10) included, the VSIR is

$$P_{IR}(t) = \frac{\lambda^2 N_V \sigma_a}{(4\pi)^3} \int_0^{2\pi} \int_0^{\pi/2} \int_h^{\infty} \frac{G^2 T_b^2}{r^4} \delta\left[t - 2\left(\frac{r_i}{c_o} + \frac{(r - r_i)}{c_s}\right)\right] \cdot e^{-2k_e(r-r_i)} u(r - r_i)\, r^2 \sin\theta \, dr \, d\theta \, d\phi. \tag{B-1}$$

The θ- and ϕ-dependence of G and T_b are assumed and $r_i = h \sec\theta$. The impulse funtion $\delta[\bullet]$ in (B-1) takes a form that can account for its propagation through both free space and the penetrable medium, as shown in Figure B.1. An impulse travels a distance r_i at speed c_o through free space to the medium interface. It then crosses into the medium and travels a distance χ at speed c_s to the differential volume dV. At this point it is scattered back toward the radar (as well as in all directions) and the path is reversed, accounting for the factor of 2 within the delta function argument.

The unit step function in (B-1) determines the upper limit on the θ integral, as discussed in §2.2.1. The argument $r - r_i = r - h \sec\theta_u$ is equated to zero and solved for θ_u which gives

$$\theta_u = \cos^{-1}\frac{h}{r} \tag{B-2}$$

instead of π as given in (B-1). This angle corresponds to where (in angle θ) the impulse intersects the medium interface, as seen in Figure B.1 Now the argument of the impulse function can be rearranged in order to isolate the r-dependence to obtain

$$\delta\left[t - \frac{2r_i}{c_s}(c_r - 1) - \frac{2r}{c_s}\right], \tag{B-3}$$

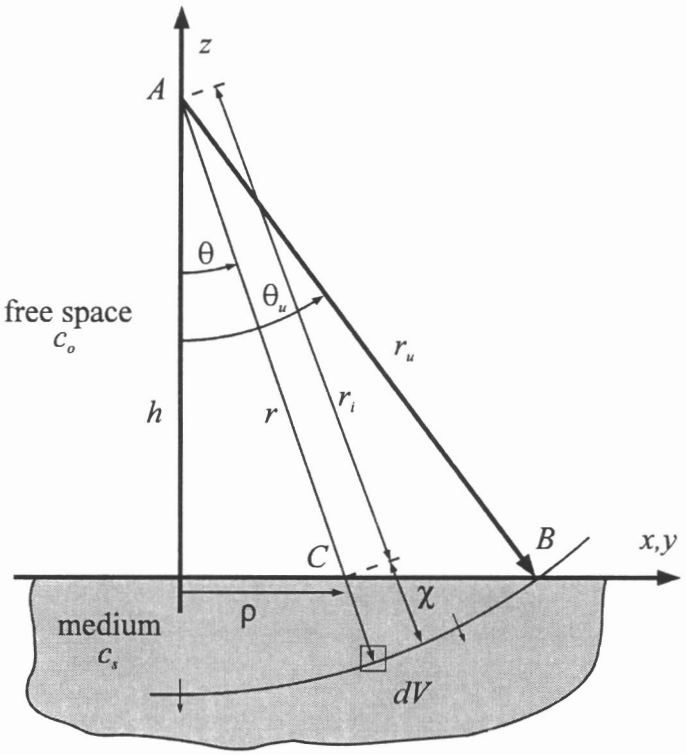

Figure B.1. Geometry used to demonstrate the r-integration of the volume scattered impulse response.

where $c_r = c_s/c_o$ is the relative speed of light in the lower medium. The r-integration can now be easily performed by making use of the *sifting property* of the impulse function. This simply replaces all references to r in (B-1) by the solution for r when the argument of the impulse function in (B-3) is equated to zero. This result is

$$\begin{aligned} r &= \frac{c_s}{2}\left[t - \frac{2r_i}{c_s}(c_r - 1)\right] \\ &= \frac{c_s t}{2} + h\sec\theta(1 - c_r). \end{aligned} \tag{B-4}$$

Also, the differential dr must be converted to dt through a Jacobian transformation:

$$dr = \frac{c_s}{2}dt. \tag{B-5}$$

This provides a $c_s/2$ amplitude factor in the resulting integration.

Substituting equations (B-2), (B-4) and (B-5) into (B-1) and simplifying, the r-integration of the impulse response becomes

$$P_{IR}(t) = \frac{2\lambda^2 N_V \sigma_a c_s}{(4\pi)^3}\int_0^{2\pi}\int_0^{\theta_u} G^2 T_b^2 \frac{\exp\{-k_e\left[c_s t + 2h\, c_r\sec\theta\right]\}}{\left[c_s t + 2h\sec\theta(1 - c_r)\right]^2}\sin\theta\, d\theta\, d\phi. \tag{B-6}$$

An important point is that the upper limit of the θ-integral does not depend on the medium. That is, the expression for r in (B-4) is not used to find the value of θ_u in (B-2) in terms of time t. Rather, the value of θ_u is determined by how far the impulse has traveled in free space to intersect the medium at the point B in Figure B.1. Thus, equation (B-2) is given in terms of t by using $r = c_o t/2$ to obtain

$$\theta_u = \cos^{-1}\frac{2h}{c_o t}. \tag{B-7}$$

This is the value for the upper limit in terms of absolute time t. In terms of the two-way ranging time $\tau = t - 2h/c_o$, equation (B-7) can be rewritten to obtain

$$\theta_u = \cos^{-1}\frac{1}{(c_o\tau/2h) + 1}. \tag{B-8}$$

Notice that this time conversion does not affect the Jacobian operation in (B-5) since $d\tau = dt$.

Vita

Michael H. Newkirk was born on July 6, 1965, in Elmer, New Jersey, where he grew up working on the family dairy farm. He graduated from Woodstown High School, Woodstown, New Jersey, in 1983.

Michael received the Bachelor of Science degree in Electrical Engineering in 1988 and the Master of Science degree in Electrical Engineering in 1990, both from Virginia Tech. In 1990, he was awarded a Bradley Fellowship from the Bradley Department Electrical Engineering at Virginia Tech, which supported his continuing research into altimeter waveform modeling.

During the summers of 1988 and 1989, Michael worked at the U.S. Naval Research Laboratory in the Space Sensing Branch of the Space Systems Division. While there he performed testing and development duties on an experimental 95 GHz, short-pulse radar altimeter system. During the summers of 1992 and 1993 he was a Visiting Scientist at NASA Goddard Space Flight Center - Wallops Flight Facility. In that position, he was responsible for data analysis in support of an ongoing ocean and ice scattering studies program.

Michael is currently employed as a Research Associate for the Bradley Department of Electrical Engineering at Virginia Tech, where he continues his research in the area of waveform scattering by penetrable media.